Programmable ultrashort highly localized wave packets

D i s s e r t a t i o n

zur Erlangung des akademischen Grades

d o c t o r r e r u m n a t u r a l i u m

(Dr. rer. nat.)

im Fach Physik

eingereicht an der

Mathematisch-Naturwissenschaftlichen Fakultät I

der Humboldt-Universität zu Berlin

von

M.Eng., Martin Bock

Präsidentin/Präsident der Humboldt-Universität zu Berlin

Prof. Dr. Dr. Jan-Hendrik Olbertz

Dekanin/Dekan der Mathematisch-Naturwissenschaftlichen Fakultät I

Prof. Dr. Stefan Hecht

Gutachterinnen und Gutachter:

1. Prof. Dr. Thomas Elsässer
2. Prof. Dr. Oliver Benson
3. Prof. Dr. Peeter Saari

Tag der mündlichen Prüfung: 25.06.2013 (15:15 Uhr, c.t.)

CONTENTS

Abstract

This thesis deals with the concept of radially non-oscillating, temporally stable ultrashort-pulsed Bessel-like beams or “needle pulses”, which are an example of a highly localized wave packet (HLW). HLWs are the closest approximation of linear-optical light bullets and provide specific benefits compared to conventional Gaussian-like light bullets. The spatio-temporally nonspreading propagation behavior of few-cycle needle beams of less than 10 fs duration will be theoretically discussed in detail. An overview of the generation and detection of localized waves carrying an orbital angular momentum is also given.

High fidelity spatial light modulators are used for the generation of HLWs. The flexible tailoring of few-cycle wave packets at near-infrared wavelengths is reported. It is shown that such pulses propagate over a huge depth of focus, neither significantly changing their spot size or nor the pulse duration. Variable geometrical distributions like circular disks, rings, or bars of light are shaped and exploited as building blocks for structures of higher complexity. The last section of the thesis emphasizes the numerous potential applications of related techniques for two-dimensional spatial pulse shaping and diagnostics based on localized waves. As a particularly important example, time-wavefront sensing is used to combine nonlinear multichannel autocorrelation with Shack-Hartmann wavefront sensing by means of localized sub-beams and adaptive functionality. The capabilities of such devices are illustrated by the results of angular and temporal mapping of few-cycle wave packets. Moreover, spatial encoding and subsequent tracking of individual sub-beams, even at incident angles of up to 50°, enables to significantly improve the spot recognition. Thus, the concept appears to be well-suited for optimizing the performance and to reduce ambiguities of 2D

pulse diagnostic systems. Finally, first steps towards the generation of optical light bullets carrying integer or non-integer orbital angular momenta are presented.

Kurzfassung

Die vorliegende Arbeit beschäftigt sich mit dem Konzept der radial nicht-oszillierenden, zeitlich stabilen ultrakurzen Bessel ähnlichen Strahlen oder „Nadelstrahlen“ („needle beams“), die zu einer Klasse von optischen hochlokalisierten Wellenpaketen generalisiert werden. Hochlokalisierte Wellenpakete (HLWs) können in diesem Zusammenhang in guter Näherung als linear-optische „light bullets“ verstanden werden, die spezifische Vorteile gegenüber Gauß ähnlichen „light bullets“ mit sich bringen. Hierbei wird die Theorie über das räumlich-zeitlichen Ausbreitungsverhaltens von nicht auseinanderdriftenden Nadelstrahlen mit Pulsdauern von kleiner als 10 fs näher diskutiert. Dies wird durch eine systematische Darstellung der Methoden zur Generierung und Detektierung von lokalisierten Wellen komplettiert, die ein optischen Drehmoment tragen.

Für die Erzeugung von HLWs kommen räumliche Lichtmodulatoren zum Einsatz, die ein flexibles Zuschneiden von Wellenpaketen mit der Dauer weniger Zyklen des Feldes im Spektralbereich des nahen Infrarot erlauben. Es wird gezeigt, dass solche optischen Pulse sich über beträchtliche Entfernungen ausbreiten, ohne dass sich dabei signifikant der Strahldurchmesser vergrößert oder der Puls zeitlich verbreitert. In variabler Weise werden geometrische Lichtverteilungen erzeugt, die runde Scheiben, Ringe, stadion- oder gitter-ähnliche Formen bilden. Der letzte Abschnitt der Dissertation hebt das bedeutende Anwendungspotential dieser auf lokalisierten Wellen basierenden Techniken der räumlichen Pulsformung und Diagnostik hervor. Als besonders wichtiger Ansatz ist der Zeit-Wellenfront-Sensor zu erwähnen, welcher die nichtlineare, mehrkanalige Autokorrelation, die Wellenfrontdetektion mittels nichtdiffraktiver Teilstrahlen nach dem Shack-Hartmann-Prinzip

und eine adaptive Funktionalität miteinander vorteilhaft verbindet. Das enorme Potential solcher Ansätze wird durch die hohe Genauigkeit orts-, winkel- und zeitabhängiger Rekonstruktionen der Wellenpakete nachgewiesen. Darüber hinaus ermöglicht das räumliche Kodieren und anschließende Verfolgen der Teilstrahlen eine wesentliche Verbesserung der Identifikation relevanter Parameter von Verteilungsfunktionen. Demnach erscheint das Konzept als hervorragend geeignet, um die Leistungsfähigkeit von 2D Pulsdiagnostiksystemen zu optimieren und Mehrdeutigkeiten zu reduzieren. Schließlich werden erste Schritte zur Generation von optischen „light bullets“ mit ganzzahligen und fraktalen orbitalen Drehmomenten präsentiert.

List of symbols and abbreviations

List of the Latin Symbols

Symbol	Notation	Unit
$\tilde{a}$	frequency order of Zernike polynomials	a.u.
b	weighting factor	a.u.
$\vec{B}$	magnetic field strength vector	
c	ellipsoid dimension in z-direction	a.u.
c_0	light speed in the vacuum	
CF	calibration factor	
D	diameter of the axicon	μm
d_{CCD}	beam diameter at the CCD plane	mm
d_{SLM}	beam diameter at the SLM plane	mm
$\vec{E}$	electric field strength vector	V/m, N/C
E_0	electric field amplitude	V/m, N/C
E_ℓ	electric field envelope of orbital momentum beams	V/m, N/C
h	height of the conical axicon	nm
f	focal length	nm
I	intensity	W/m^2; kg/s^{-3}
Im	imaginary part	-
J	total optical angular momentum	Js

J_n	Bessel function of n-th order	-
J_0	zero order Bessel function	-
k	wave vector	m^{-1}
k_0	wave vector in vacuum	m^{-1}
k_r	wave vector in transverse direction	m^{-1}
k_z	wave vector in axial direction	m^{-1}
K	kurtosis	-
ℓ	topological charge, orbital angular momentum	-
L	optical path length	mm
L_{diff}	integer Talbot distance	mm
L_{int}	self-imaging distance	mm
m	diffraction order	-
M^2	beam quality factor	-
M_{new}^2	modified beam quality factor	-
M_{NB}^2	beam quality factor of a needle beam	-
M_{orb}	momentum density	Js/m^3
n	refractive index in the medium	-
n_{SPP}	refractive index of the spiral phase plate material	-
$\tilde{n}$	radial order of Zernike polynomials	-
P^2	pulse propagation factor	-
p_g	spatial period of a grating	μm
L^2	spatiotemporal localization parameter	-
q	integration variable	-
Re	real part	-
R	radius of the axicon	-
r	radial coordinate	mm
sh	spot shift	μm
S	spectral function	-
t	time	s
U	radial component of Zernike polynomials	-
V	magnification factor	
W	wavefront	-
$\vec{W}$	wavefront vector	m^{-1}
w	beam radius	mm (μm)

w_0	beam waist radius	mm (µm)
x	transverse coordinate	mm (µm)
y	transverse coordinate	mm (µm)
z_0	Rayleigh length	mm
z	position in propagation direction	mm
z	depth of field of a Bessel beam	mm
Z	Zernike polynomial	-

List of the Greek Symbols

Symbol	Notation	Unit
α	base angle of the axicon	rad (mrad); °
α_{max}	maximum base angle of the axicon	rad (mrad); °
γ	angle of incidence	rad (mrad); °
δ	delta function	
ε_0	dielectric constant	
ζ	wavefront tilt	rad (mrad)
η	azimuthal angle	rad (mrad); °
θ	conical angle	rad (mrad); °
λ	wavelength	nm
λ_0	vacuum wavelength	nm
π	pi	
ξ	phasefront	rad (mrad); °
ρ	radius of curvature	m
ς	screw angle	rad (mrad); °
σ	standard deviation	µm
σ_{NB}	standard deviation of the needle beam width	µm
σ_0	standard deviation of the beam width	µm
σ_∞	standard deviation of the beam width in the far-field	1/µm
σ_v	standard deviation of the spectral width	µm
σ_t	standard deviation of the temporal width	µm
v	spatial frequency	1/nm

σ	spectral standard deviation	nm
ξ	angle of incidence within the liquid crystal layer	rad (mrad); °
τ_0	input pulse duration	fs
τ_p	pulse duration	fs
τ_{FWHM}	pulse duration at the full-width-at-half-maximum	fs
υ	normalized radial distance	
φ	phase	rad (mrad); °
φ_0	constant phase term	rad (mrad); °
$d^2\varphi/d\omega^2$	group delay dispersion	fs^2
Φ	complex phase term	rad (mrad)
Φ_ℓ	wavefront curvature in axial and radial direction	rad (mrad)
ω	angular frequency	Hz
ω_0	center angular frequency	Hz
Ω_a	angular velocity	m/s
η_S	normalized diffraction efficiency	-
∇	Nabla-operator	-

List of the Letter Symbols

Acronym	**Notation**
BBO	Beta-Barium-Borate
CAR	Chirped ARrangement
CCD	Charge-Coupled Device
CPP	Checkered Phase Pattern
DC	Down-Conversion
DOE	Diffractive Optical Element
EMCCD	Electron Multiplying Charge-Coupled Device
FRAC	Fringe Resolved Autocorrelation
FROG	Frequency Resolved Optical Gating
FWHM	Full-Width at Half-Maximum
GTI	Gires-Tournois-Interferometer
GDD	Group-Delay-Distortion
HLW	Highly Localized Wave packet

HLB	Highly Localized Beams
HOT	Homodyne Optical Technique
HPP	Homogeneous Phase Pattern
LC	Liquid Crystal
LCoS	Liquid Crystal on Silicon
LX	Long Crystal
MEMS	Micro-Electro-Mechanical System
MBI	Max Born Institute
NBA	Needle Beam Array
OAM	Orbital Angular Momentum
PAN	Parallel Aligned Nematic
PG	Polarization Gated
SD	Self-Diffraction
SEA	Spatially Encoded Arrangement
SF	Symmetry Factor
SHG	Second Harmonic Generation
SHS	Shack-Hartmann Sensor
SLM	Spatial Light Modulator
SNB	Single Needle Beam
SVEA	Slowly Varying Envelope Approximation
SPIDER	Spectral Phase Interferometry for Direct Electric field Reconstruction
TADPOLE	Temporal Analysis by Dispersing a Pair of Light E-fields
TG	Transient-Grating
THG	Third Harmonic Generation
VAN	Vertically Aligned Nematic
X	Cross-correlation
ZAP	Zero Additional Phase

CHAPTER 1

1 Introduction

Lasers with ultrashort pulses are universal tools in physics research. By means of the concentration of the whole pulse energy within a small time interval, high peak intensities can be achieved. This enables the study of strong nonlinear light-matter-interactions and new physical phenomena. On the other hand, ultrashort pulses offer new insight into ultrafast dynamical processes. The range of applications is extremely broad and includes optical clocks, probing of chemical reactions, quantum control (quantum computing) and nanostructuring. With the introduction of solid state gain media and the understanding of the pulse generation conditions (intra-cavity pulse shaping), mode-locked lasers became commercially available with pulse durations down to only a few cycles of the electric field [Kär04]. To obtain higher energies the pulses are amplified, spectrally broadened and recompressed close to the Fourier limit. In general, the evolution of the space and time variables of ultrashort pulses are treated independently, which means a separate observation of the spatial beam profile and the temporal pulse shape. However, the assumption of separable parameters is inadequate for a complete characterization because spatial and temporal aberrations caused by misalignments of the optical components have to be taken into account. If space-time coupling effects occur, the beam intensity, the pulse duration as well as the spectral amplitude and phase become complex functions of the space-time-coordinates. Moreover, the complexity increases for even shorter pulses with extremely broad optical spectra and if further effects like wavefront distortions (e.g. orbital angular momentum) and polarization effects are included. Spatiotemporal characterization techniques of pulses allow

for the possibility of observing such couplings effects. For instance a pulse can be found to be chirped at one spatial position, but Fourier-limited at another.

Most pulse characterization methods, such as wavefront-autocorrelation, FROG or SPIDER do not measure the full spatiotemporal behavior of optical pulses. For the exploration of ultrafast phenomena, proper diagnostics and control of spatial and temporal pulse parameters is important. Besides the well-established acousto-optical or liquid crystal pulse shapers for the temporal domain, micro-electro-mechanical deformable mirrors and liquid crystal based micro-displays are the most common devices allowing for the highest flexibility in 2D spatial light modulation. With such devices it is straitforeward to manipulate all parameters of ultrashort pulses. Flexible shaping of ultrashort pulsed wave fields is of increasing interest with potential applications in measuring techniques, optical communication, information processing or encoding, linear or nonlinear spectroscopy, materials processing, particle acceleration and controlling filamentation.

For these applications simultaneous temporal as well a spatial confinement of light requires new methods to synchronize all spectral contributions coherently. Such a confinement is fundamental in physics [Saa05, Saa06, Saa12] and is extremely challenging for few-cycle or single-cycle optical pulses. In recent experiments, the spatial compression of femtosecond laser pulses down to the diffraction limit was demonstrated with the help of an all-reflective microscope objective [Pig11]. Here, the energy was concentrated in a volume of only about 1.8 μm^3.

Now the question of how to maintain a set of spatial and temporal parameters over an extended propagation distance arises or what kind of boundary conditions are necessary to keep the pulse compact as it propagates. The answer can be found in Maxwell equations which give localized non-dispersive solutions of propagating electromagnetic waves (so-called undistorted progressive waves) [Str41]. This kind of free propagating electromagentic wave experiences no diffraction or spreading in space and time over arbitrary distances (supercollimation). Generally, the unique interaction between spectral interference and spectral-dependent time delays allows shaping of wave packets which are robust against distortions and deformations. The behavior is quasi particle-like. However, because of the finite energies and apertures such beams are physically not realizable but can be approximated with certain optical elements (e.g. by annular slits or axicons). The basis of a theory to predict new localized waves uses spatiospectral interference of wave packets However, the most interesting types are X-shaped waves or Bessel-X-pulses.

Ideal Bessel beams represent propagation-invariant solutions of the Helmholtz equation for conical waves [Dur87] possessing infinite extension, spatial electric field distributions given by Bessel functions, and self-reconstruction capabilities. Physical approximations including diffractive, refractive or reflective axicons lead to finite Bessel zones [Her00]. An established method to measure the spatiotemporal properties of pulsed Bessel beams is the Spatially Encoded Arrangement for Temporal Analysis by Dispersing a Pair of Light E-fields (SEA TADPOLE) [Bow09, Val09]. Higher order Bessel beams with central minima are obtained by illuminating axicons with Laguerre-Gaussian beams [Arl00]. By combining Airy pulses with Bessel beams, nondispersing and nondiffracting wave packets can be realized which are offered in the literature as versatile linear light bullets [Cho10]. The approach in this publication of introducing a large cubic spectral phase, makes the pulse insensitive to a certain huge amount of GDD (main material dispersion) and thus the behavior is non-dispersive, but the true pulse is several 100 fs long. The major disadvantage of Airy pulses can be seen in the oscillations of the Airy function consisting of a train of pulses with slowly decreasing peak amplitudes. More advantageous for applications are nonspreading localized wave packets without spatial and temporal oscillations.

Localized optical light waves have been studied with increasing interest during the past two decades. Only a few publications, however, have dealt with high localization wave packets. The spatiotemporal structure should be fringeless in space and time to achieve the optimal localization.

In this thesis the generation, manipulation and characterization of such localized wave packets with pulse durations down to 2.4-cycles of the electric field are addressed in detail. On the basis of programmable, ultraflat axicons, X-shaped pulses (“needle beams”) are generated via a liquid-crystal-on-silicon spatial light modulator (LCoS-SLM) starting with few-cycle pulses from a Ti-sapphire oscillator. The specific advantages of fringeless Bessel-beams are, extreme aspect ratios, high tilt robustness and an excellent pulse transfer.

In general, needle beams can be obtained by a self-apodized truncation via a tailored aperture or at very small axicon angles. The latter method was preferred because of being more flexible with respect to geometry, angle and losses when using phase-only LCoS-SLMs. The transition between Bessel-like beams (with) and needle beams (without fringes) is determined by the axicon angle. Furthermore, the typical space-time-structure of Bessel pulses (X-shape) disappears if the fringes around the central maximum are suppressed. The localization is then increased. A further advantage of needle beams is that the programmed phase profiles (corresponding gray level patterns) are not restricted to conical shapes, as will be shown.

Therefore, the intensity profiles are extended to other distributions like rings or lines. In this context, a generalization to a class of highly localized wave packets is made and allows for the treatment of such beams as linear versatile light bullets. Furthermore, the uniqueness of this concept enables the generation of the ultimate nonspreading light bullet – the single-cycle needle beam.

This thesis is organized as follows. First, an introduction to theoretical approaches describing localized waves with and without an orbital angular momentum is given. In chapter 2 special aspects of (and differences between) Bessel and needle beams will be discussed and a new approach is introduced for evaluating the propagation qualitatively. A brief review of the experimental techniques can be found in chapter 3. This includes a detailed spatiospectral description of mode-locked few-cycle pulsed lasers and spatial light modulators, which are are one of the main topics of this dissertation. Furthermore, a brief introduction to the experimental setup is given, including the working principle of an extended type of Shack-Hartmann sensor. Chapter 4 is completely devoted to experiments on shaping and combining highly localized waves via high fidelity spatial light modulators. A special attention is dedicated to ultra-broadband pulsed needle and hollow beams and their spatiotemporal propagation characteristics and free programmability. Periodic and non-periodic arrangements of needle beams obtained by controlling axicon-shaped phase profiles in a simple and flexible way are discussed. It is shown that complex patterns ("flying images") can be shaped whose recognizability is maintained over extremely large distances without significant degeneration with respect to diffraction and cross-talk effects. In addition, conventional arrays of nondiffracting needle beams are introduced to measure the wavefront and the spatially resolved pulse duration of pulsed laser sources. In this context, a relative time resolution in the attosecond range is achieved by analyzing time delays between autocorrelation traces of the sub-beams. In the second last subchapter localized waves with an orbital angular momentum are of special interest. These pulsed vortex beams of micrometer dimensions show nondiffracting propagation properties over several millimeters. Finally, in chapter 5, conclusions are given, including future directions and experiments in this field.

CHAPTER 2

2 Theoretical background

2.1 Propagation-invariant solutions of the Helmholtz wave equation

2.1.1 History and Definition

Localized waves (LW) or nondiffracting waves are known since a long time. First theoretically predicted in 1915 by Bateman, they were shown to be specific wavelet type solutions to the Maxwell equations which behave similarly to solitons [Bat15]. One kind of waves which are devoid of diffraction are the well-known plane waves as a direct and simplest solution of the wave equation. In these cases, amplitude and phase appear propagation invariant. However, Stratton found another monochromatic solution whose transverse shape was described by a Bessel function [Str41]. Moreover, it was found that certain compositions of plane waves can generate new nondiffracting field distributions. Besieris proposed a new integral method to describe these LWs by decomposing the scalar wave field equation into forward and backward traveling plane waves (bi-directional ansatz) [Bes89]. It should be mentioned that the wave equation is only a part of a larger class of equations which admit the concept of nondistorted progressive waves. Depending on the boundary conditions, analogue solutions exist also for the force-free Schrödinger equation (thus indicating the theoretical existence of nondiffracting quantum states) [Ber79].
Localized waves can exist either in the monochromatic as well as polychromatic regime. Especially localized nondiffracting pulses are shape-preserving structures of light in the spatial and temporal domain. Ideal localized wave packets propagate over arbitrary distances

without broadening in space and time. However, because of the finite energies and finite apertures such beams are physically not realizable. Any kind of beam with a finite energy distribution (containing a spectrum of wave vectors) leads to dispersion and spread of energy and thus to a localization over a finite distance. Nevertheless, finite energy LWs have distinct advantages compared to quasi-monochromatic or broadband Gaussian pulses. For a certain depth of field such beams are as well less affected by spatiotemporal deformations. That was shown by Sezginer who formulated a general description for focus wave modes including finite-energy pulses [Sez85]. Durnin's exact nondiffracting solution of the scalar wave equation confirmed the existence of beams (Bessel beams) whose central lobe shows an exceptional resistance to diffractive perturbations [Dur87]. Later, in the 1990s, Lu et al. constructed theoretically and experimentally new solutions to the wave equation in free space by superimposing Bessel beams with different acoustical frequencies but same phase velocities (same axicon angle) [Lu92]. The appearance of an X-structure in the field distribution centered and the nondiffracting character in axial and transversal direction is very typical for such kind of beams. Therefore, this polychromatic generalization of Bessel beams was later used for describing also optical ultrashort Bessel wave fields. On this basis, spatially and temporally non-oscillating localized waves were constructed, defined as light bullets [Zam02, Zam08]. It should be noted that in a strict sense only non-disturbed solutions of the nonlinear wave equation can be considered as solitons (or bullets) [Con04].

The phenomenon of light bullets is well-known in the literature. Silberberg (1990) described the collapse of optical pulses in a homogenous medium under the combined action of diffraction, anomalous dispersion, and nonlinear refraction [Sil90]. He predicted that under certain conditions nondispersing, nondiffracting optical pulses are possible, which he referred to as "light bullets". The specific interaction of light with the medium determines whether the bullet is of linear or nonlinear type. Such nonspreading light fields exploit either linear or nonlinear effects. The nonlinear light bullets are among the well-known solitons self-trapped in space and time. Solitons appear in fluids, plasmas, solids, matter waves, but also in classical EM-fields as bright, dark, scalar, vector and numerous other optical solitons [Kiv03]. The interaction of diffraction, dispersion and nonlinear self-phase modulation counteracts the spreading and leads to spatio-temporally stable wave packets. Generally, the propagation behavior is very sensitive against perturbations. Thus, the complex interaction of the aforementioned propagation parameters have to be well-controlled to prevent a too fast decomposition of the soliton. Linear light bullets are in this regard more appropriate to shape nonspreading wave fields because they are by nature more distinct and stable (linear

interaction: diffraction, refraction, dispersion, etc.) in comparison to their nonlinear counterparts. In the literature, a plenty of various linear or nonlinear light bullets are described, including Bessel beams, e.g. Airy [Gut00], Mathieu [Siv07], Helmholtz [Rin12], Pearsey [Zha12], Weber [Ale12], and other beams. Furthermore, three dimensional wave packets have been reported in the literature without exploiting nonlinear effects of media [Her08, Sõn97, Lu92, Tra03, Por04, Lon04]. A rough overview (not complete) of selected approaches of light bullets is given in *Fig. 2.1.1*. Additionally, the family of localized waves comprises not only X-type superluminal waves but also sub-luminal and luminal localized waves [Saa04].

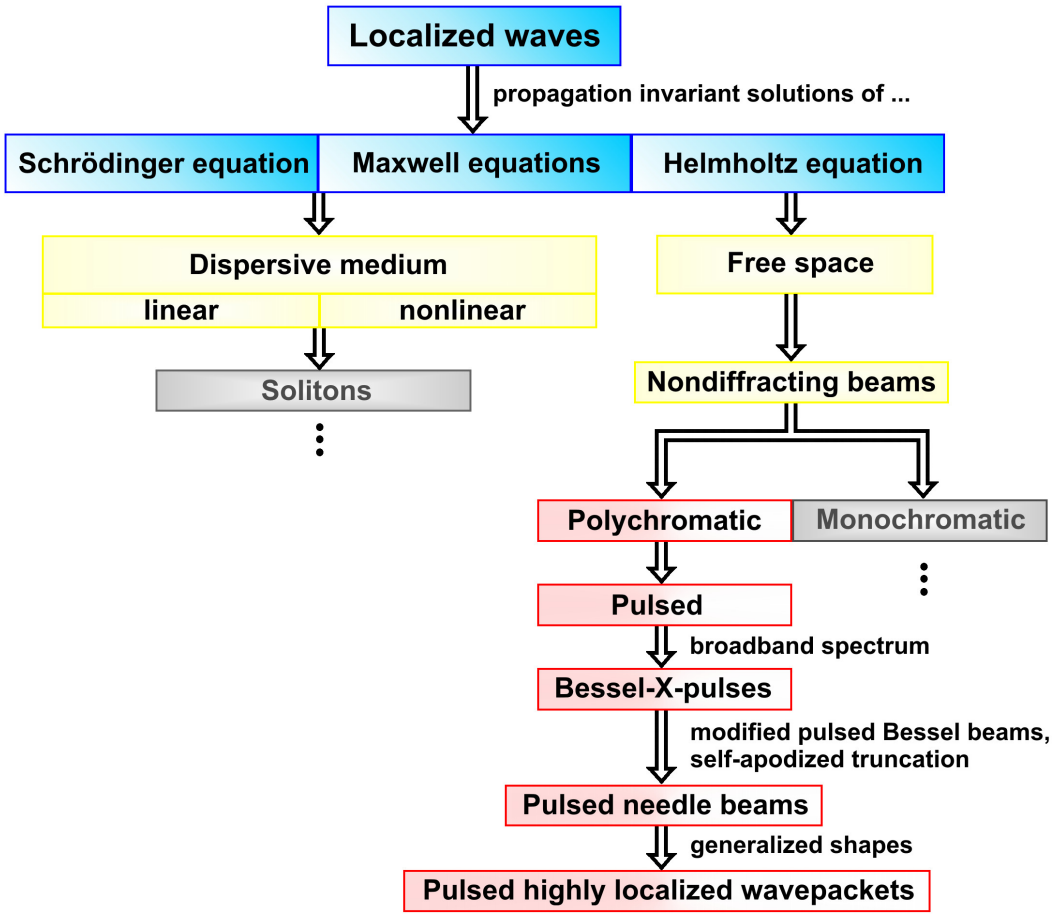

Fig. 2.1.1 Family tree of localized waves: The red fields indicate the classification of linear light bullets. In the right arm of the flow chart one can find the specific case of self-apodized Bessel-X-pulses or pulsed needle beams.

In this context the generation and spatiotemporal propagation dynamics were investigated in very details but a spatial shaping and composition as well as the propagation behavior of such linearly generated localized waves, however, remained largely unexplored. For that reason, linear light bullets of various spatial shapes propagating in free space (red fields in the right part of *Fig. 2.1.1*) will be examined in the following.

2.1.2 Structure of localized waves

Starting point of the considerations to describe the propagation behavior of localized nondiffracting pulses is the homogeneous wave equation in cylindrical coordinates. The equation in this form only consider axially symmetric solutions, albeit alternative coordinate transformations allow to construct any other nondiffracting wave. The only criterion is that it must satisfy the wave equation. Nevertheless, after separating the variables the wave equation in radial direction *R(r)* is obtained, well-known as Bessel's equation:

$$r^2 R''(r) + rR'(r) + (r^2 - n^2)R(r) = 0\,. \tag{1}$$

The two linearly independent solutions to this differential equation are the Bessel function $J_n(k_r,r)$ and Neumann functions $Y_n(k_r,r)$. The variable r describes the radial-dependent function curve whereas n determines the order of the Bessel (Neumann) function. The Bessel function is described as follows:

$$J_n(k_r,r) = \frac{1}{\pi}\int_0^{\pi} \cos\left[2\pi \cdot r \cdot \frac{\sin(\theta)}{\lambda} \cdot \sin(q) - n\theta\right] \cdot dq\,, \tag{2}$$

where θ, λ, and q represent the conical angle, the optical wavelength, and integration variable, respectively.

Following the approach in [Her08], a general expression for an axially symmetric solution is derived, satisfying also the wave equation. The solution is written in terms of a Bessel-Fourier transform with respect to the radial coordinate r:

$$\Psi(r,z,t) = \int_0^{\omega/c}\int_{-\infty}^{+\infty} k_r J_0(k_r,r)\exp(ik_z z)\exp(-i\omega t)S(k_r,\omega)\,d\omega\,dk_r\,. \tag{3}$$

Here, k_z can be substituted by

$$k_z{}^2 = k^2 - k_r{}^2 = \frac{\omega^2}{c^2} - k_r{}^2\,, \tag{4}$$

where the wave vector k is split into a radial k_r and axial k_z vectorial component. The very important spectral function $S(k_r, \omega)$ is responsible to construct any kind of solution. From the physical point of view, the spectral function is nothing other than an expression for a wave vector distribution of an optical field around the propagation axis for a single optical frequency or frequency spectrum. The purpose of the following considerations is to emphasize the differences of the spectral functions of Gaussian and Bessel beams, respectively. It is obvious that for a Gaussian beam the wave vectors (plane waves) propagate in all directions. The angular distribution of the vectors is then determined by a Gaussian envelope function as it is visualized in *Fig. 2.1.2(a)*. The spectral function is formulated as follows, fulfilling the aforementioned requirements:

$$S(k_r,\omega) = 2w_0{}^2 \exp\left(-w_0{}^2 k_r{}^2\right)\cdot \delta(\omega-\omega_0)\,. \tag{5}$$

The delta function $\delta(\omega-\omega_0)$ implies a monochromatic beam whereas w_0 denotes the width of the spectral function. Note that for pulsed Gaussian beams the spectral function should be extended with a frequency spectrum. After substituting the spectral function of monochromatic fields into equation (3) and applying the paraxial approximation one ends up with a Gaussian distribution [Har08]:

$$\Psi(r,z,t) = w_0{}^2 \frac{\exp\left(-\dfrac{r^2}{\left(w_0{}^2+\dfrac{i2z}{k_0}\right)}\right)}{\left(w_0{}^2+\dfrac{i2z}{k_0}\right)} \exp\left(ik_0 z - i\omega_0 t\right). \tag{6}$$

After some mathematical operations (multiplying with conjugate complex terms) this equation appears as the amplitude distribution of a Gaussian beam in the well-known form [Ald02]:

$$\Psi(r,z,t) = \frac{w_0 \exp\left(-\dfrac{r^2}{w(z)^2}+i\dfrac{k_0 r^2}{2R(z)}\right)}{w(z)} \exp\left[ik_0\left(z-ct\right)\right], \tag{7}$$

with

$$|w(z)|^2 = w_0^2\left[1+\left(\frac{2z}{k_0 w_0^2}\right)^2\right], \tag{8}$$

$$\rho(z) = z\left[1+\left(\frac{k_0 w_0^2}{2z}\right)^2\right], \text{ and} \tag{9}$$

$$k_0 = \frac{2\pi}{\lambda_0} \tag{10}$$

The expression describes the propagation behavior of a Gaussian beam with a z-dependent evolution of the beam width $w_0(z)$ and radius of curvature $\rho(z)$ of the wavefront for a central wavelength λ_0. Both parameters depend on propagation distance. The beam width is the smallest at $z = 0$, usually denoted as the beam waist. Furthermore, at this position the radius of curvature is infinite which corresponds to a flat wavefront. A further consequence of Gaussian propagation behavior is the fact that the initial beam radius w_0 is doubled after traveling the distance $z = 3^{½}k_0w_0^2/2$ (other features of Gaussian beams can be found in the literature [Gue90, Hod92, Ped93, Sal91, She89, Sie96, Sve89]). It is called diffraction length and can be very short in a frame of a very small spot size (tightly focused Gaussian beams).

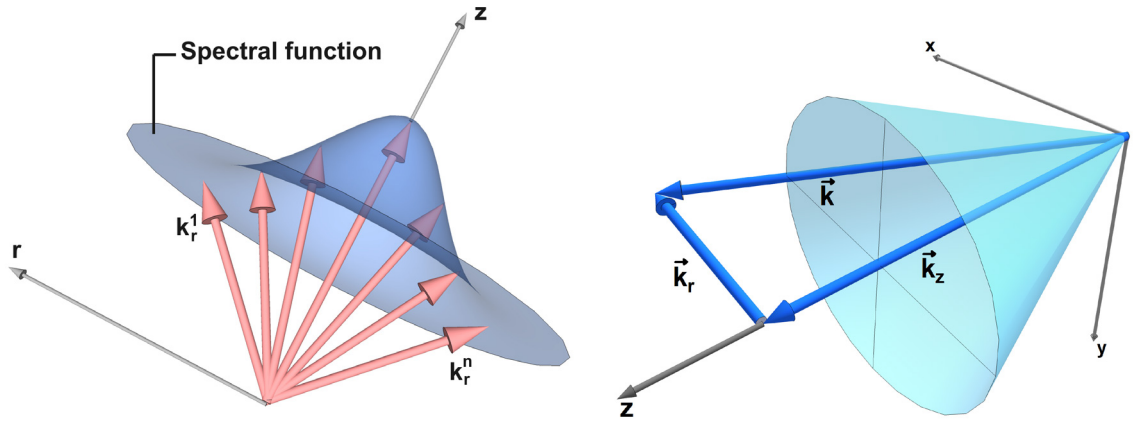

(a) **(b)**

Fig. 2.1.2 Visual interpretation of the vector distributions of different spectral functions. Here, the symmetry axis is identified as the propagation axis. It should be mentioned that especially in the case of Bessel beams this definition is not completely applicable because of the divergent behavior, however, for Gaussian beams (averaged wave vector lies on the symmetry axis) this assumption is very helpful. **(a)** Here, the spectral function is assumed to be a rotational symmetric Gaussian function where all plane waves are superimposed. **(b)** For conical beams the spectral function consists of vector components which are laying on the surface of a cone. The cone angle measured to the optical axis is constant. Each k-vector can be projected on a radial and axial component.

To achieve a much longer nondiffracting zone the spectrum of k-vectors should be significantly reduced, ideally to only a single vector corresponding to a single angle. In practice, however, pseudo nondiffracting beams are obtained by a very narrow angular distribution of the k-vectors. Due to this reduction obtained, for instance, by a spatial separation of plane waves behind a lens (e.g. annular slit) or by redirecting the plane waves (e.g. by a conical axicon) it becomes evident that this transformation leads to an increased degree of localization [Rei02, Rei04]. To conclude, all kinds of nondiffracting waves have a conical shape characteristics of the wavefronts.

Bessel beams are a superposition of plane waves whose wave vectors lay on a surface of a cone as sketched in *Fig. 2.1.2(b)*. Each wave vector confines the same and constant angle to the propagation axis independent on the radial coordinate. Consequently, the wave vector can be decomposed into radial and axial component $\boldsymbol{k} = (k_r, k_z)$. This unique property implies a linear constraint between optical angular frequency ω and the radial vector $k_r=(\omega/c)\cdot\sin(\theta)$ and shows the specific space-time coupling which is very important to obtain localized waves [Har08]. For a Bessel beam the spectral function (arbitrary thin hollow cone) becomes:

$$S(k_r,\omega)=\frac{\delta\left(k_r-\left(\frac{\omega}{c}\sin\theta\right)\right)}{k_r}\delta(\omega-\omega_0)\,. \tag{11}$$

By inserting equation (11) in (3) one can recognize that symmetric Bessel beams are indeed a superposition of plane waves propagating on a predefined path (vector cone)

$$\Psi(r,z,t)=J_0\left(k_r r\right)\exp\left(ik_z z-i\omega t\right), \tag{12a}$$

and after substituting k_r and k_z, one yields after some algebra:

$$\Psi(r,z,t)=J_0\left(\frac{\omega_0}{c}\sin(\theta)r\right)\exp\left[i\frac{\omega_0}{c}\cos(\theta)\left(z-\frac{c}{\cos(\theta)}t\right)\right]. \tag{12b}$$

As it follows from the above equation the Bessel beam keeps its transversal shape while propagating. Independently on the distance the vector cone is ideally undistorted and identical for each position. That means a permanent reconstruction of the Bessel beam profile by interference. In principle, the “diffraction-free” distance can be made arbitrary long for Bessel

beams. By taking finite apertures into account the reconstruction is perturbed at the diffraction distance of the aperture. Affected by diffraction, the k-vector cone or the spectral function, respectively, becomes a function of the distance. Narrowed by the aperture (sharp cut), the beam intensity begins to oscillate when light interferes coming from the outermost lobe and decays rapidly at the diffraction distance. For this very reason real localized waves are bounded to a finite nondiffracting distance. Finite aperture nondiffracting beams are limited in the depth of field z_{max} by the axicon size (aperture radius R) and the beam axicon angle θ:

$$z_{\max} = \frac{R}{\tan\theta}. \tag{13}$$

A larger axicon angle increases the lateral resolution but also reduces the depth of field at the same time. This behavior is comparable with conventional optics. As long as the distance to the axicon aperture is much smaller than the depth of field z_{max} it is appropriate to apply equation (12b) to the description of the spatial intensity distribution. Otherwise, when the radial variable r becomes equal to the aperture radius R the contribution of the diffracted light has to be taken into account and a scalar diffraction theory (e.g. Fresnel-Kirchhoff diffraction integral) is suitable for the description of the optical field. However, the influence of diffraction can be significantly reduced by using optical elements without sharp edges. A phase apodization is obtained by a continuous and slow decrease of the axicon height. This concept is preventially applicable for focusing optics with flat or ultraflat angles. As it will be shown later on, a discrete phase apodization of sufficient height resolution is achieved by programming well-designed gradient-index distributions into a liquid crystal spatial light modulator.

Another consequence of interfering conical waves is the capability of self-healing. This effect is simply another description for a shadowing effect shortly behind an obstacle. The undistorted intensity profile (Bessel function) is reproduced at distances where the undisturbed conical wave parts contribute to the interference.

2.2 Ultrashort-pulsed large-bandwidth needle beams

For ultrashort pulses, the monochromatic spectral function of a Bessel beam has to be extended to the polychromatic case by applying a frequency spectrum instead of a Dirac delta function. The resulting X-shaped pulses feature the property of a localization both in space and time. Similar to monochromatic ideal Bessel beams, ideal Bessel-X pulses propagate nondispersive and nondiffracting for all times. Assuming a Gaussian frequency spectrum one finds a modified analytical expression for the zeroth order Bessel-X pulse [Saa97a, Saa97b]:

$$J_{PBB}(r,t) = \mathrm{Re}\left\{\sqrt{Z}\cdot\exp\left[-\frac{\tau_a{}^2 + t^2}{2\tau_0{}^2}\right]\cdot\exp\left[i\frac{2\pi\cdot t\cdot c}{\lambda_0}\right]\cdot J_0(r,k_r)\right\} \tag{14}$$

with

$$J_0(r,k_r) = \frac{1}{\pi}\int_0^{\pi}\cos\left[\Phi(r,t)\cdot\sin(q)\right]\cdot dq\,, \tag{14a}$$

$$\Phi(r,t) = Z\cdot k_r\cdot r = Z\cdot r\cdot 2\pi\cdot\left(\frac{\sin(\theta)}{\lambda_0}\right), \tag{14b}$$

$$Z(t) = 1 + i\frac{t\cdot\lambda_0}{2\pi\cdot c\cdot\tau_0{}^2}\,, \tag{14c}$$

$$\tau_a = \frac{r}{c}\sin(\theta)\,, \tag{14d}$$

$$\tau_0 = \frac{\tau_{FWHM}}{2\sqrt{\ln 2}}\,, \tag{14f}$$

where t is the time, r the radius, k the wave number, θ the cone angle, λ the wavelength and q a variable of integration. The other terms are identified as a wavelength-dependent Bessel distribution in radial direction $J_0(r, k_r)$, a complex phase term $\Phi(r,t)$, a radial-dependent time separation τ_a between two interfering pulses and as an input pulse duration τ_0. Equation (14) represents the typical X-structure in a space-time-diagram. With a time-integrating detector such an X-pulse can be measured via second order autocorrelation technique in a nonlinear crystal. The typical X-shape in the autocorrelation trace originates from the fact that towards higher radii two time-separated pulses appear whereas the time delay between both pulses

depends on the radius. Approximately, it is justified for needle beams to replace the Bessel integral by the following formula [Abr72]:

$$J_{0,NB} = \exp\left[-\left(\frac{\pi r \sin(\theta)}{\lambda}\right)^{16}\right] \cdot \left(1 - \frac{\Phi(r,t)^2}{4} + \frac{\Phi(r,t)^4}{64} - \frac{\Phi(r,t)^6}{2304}\right). \qquad (15)$$

Axicons as well as circular or spiral gratings are specialized optics (meso-optics or non-imaging optics) with unusual functionality. With such optics generally a point-like source is converted into a straight line or a more complex line distribution. Axicons with conical shapes are the well suited optics to convert a plane wave into a conical wavefront as it is required for the generation of monochromatic, polychromatic or pulsed Bessel [Dur87], Bessel-Gaussian [Gor87] or quasi-Bessel [Her91] beams. In recent experiments it was shown that the particular shaping properties of Bessel beams are predestined to focus femtosecond laser pulses [Boc05]. The modifications of the spatiospectral and spatiotemporal characteristics are negligible within the central lobe as expected from pulsed localized waves. Because of the spatiospectral interference, however, the outer rings are spatially chirped. Consequently, the pulse duration increases with the radius due to a narrowed optical spectrum. One can distinguish between the two most important subvarieties: (i) Bessel beams with a wavelength-dependent and (ii) Bessel beams with a wavelength-independent radial wave number:

$$\text{(i)} \quad \nu_0(\lambda) = \frac{\sin(\theta)}{\lambda}, \qquad (16)$$

$$\text{(ii)} \quad \nu_0(\lambda) = const. \qquad (17)$$

In the first case, a spatial chirp in radial direction emerges. In the other case, each spectral component superimposes exactly with the same angle showing a constant pulse duration over the radius. In theory, any kind of dependence of the radial wave number is possible to apply theoretically. However, a practical realization will require more complex axicons than such with only a conical shape. A special design of the axicon can be ingeniously circumvented when only the central lobe with spatially independent spectral and temporal properties is considered. This is shown in the next section focused on discussing the properties of ultrashort truncated Bessel beams (needle beams).

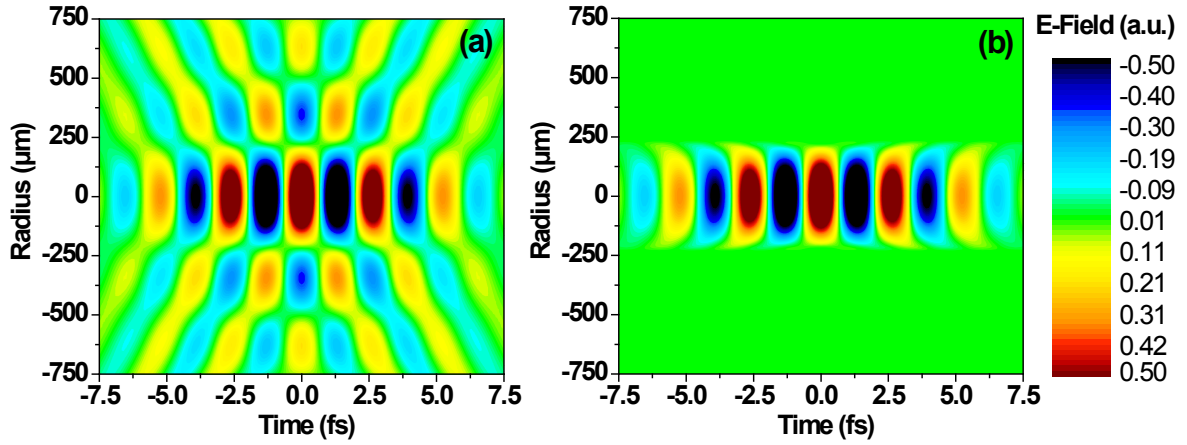

Fig. 2.2.1 Calculated space-time properties of a pulsed Bessel and needle beam in terms of the electric field. To evaluate also the oscillation in the outer fringes, the range of the scale of the electric field was chosen to be oversaturated in the center: **(a)** Radially dependent electric field of a pulsed Bessel beam of a pulse duration of 6 fs, **(b)** radially dependent electric field of a spatially self-apodized pulsed Bessel beam (needle beam) of the same pulse duration. Calculation parameters: center wavelength at λ_0 = 800 nm; conical angle θ = 1.8 mrad; axicon radius R = 450 µm.

The required apodization is usually realized by an arbitrary aperture. But without an appropriate size of the aperture, the beam quality is perturbed by diffraction effects at the edges. The size should be matched exactly to the first zero of the electric field of the radial Bessel profile. Then, only the central maximum passes the aperture and modified Bessel-X pulse denoted as "pulsed needle beam" or "needle pulses" are generated. The disadvantage of wasting photons by an aperture is avoided by using axicons of extremely small conical angles. This works best when the lateral interference zone matches exactly to the first minimum.

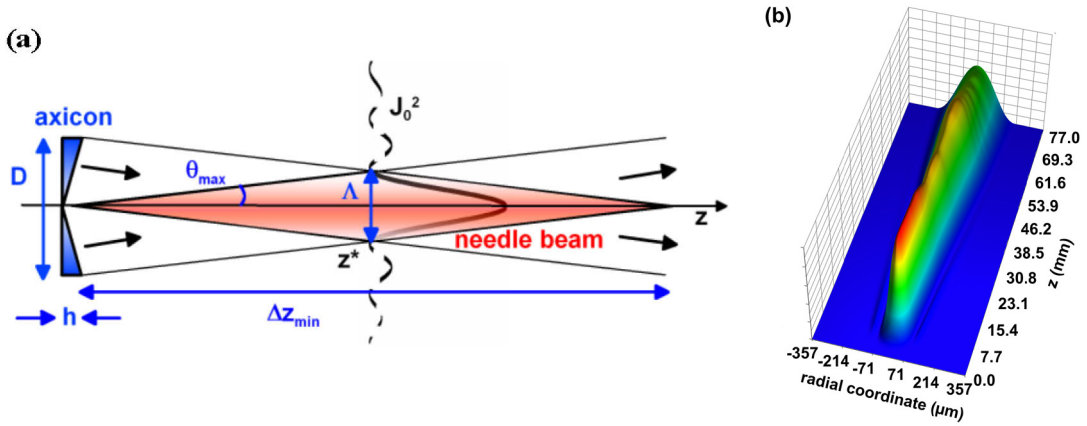

Fig. 2.2.2 Theoretical needle beam propagation: **(a)** Schematical view on the interference conditions of self-apodized Bessel beams. For the case that the transverse extension of the needle beam is equal to the first zero of electric field distribution following a Bessel function, a perfect needle beam is generated. **(b)** Simulated propagation for realistic parameters (Gaussian spectrum) over an axial depth from z = 0 mm to z = 77 mm in steps of 1 mm.

The equation (14) allows to calculate the electric field of an ideal pulsed Bessel beam (Bessel-X pulse) generated via an axicon of infinite diameter which is plotted in time-space-coordinates in *Fig. 2.2.1(a)* where the X-structure as mentioned above is clearly recognized. It

further allows the calculation of the electric field of the self-apodized Bessel beam (needle beam) as shown in *Fig 2.2.1(b)*. If the axicon angle remains unchanged the axicon radius R has to be appropriately adapted to obtain a needle beam which is given by:

$$R = \frac{\lambda}{n\theta}. \tag{18}$$

and is directly derived from *Fig. 2.2.2(a)* by geometrical approaches, assuming that the axicon angle is very small. A simulation of the propagation behavior of a needle beam (using the equation above) is plotted in *Fig. 2.2.2(b)* by assuming an axial-dependent conical angle and negligible diffraction effects. The intensity fluctuations originate from specific superposition conditions (input wavefront, axicon shape, pulse duration and spectrum).

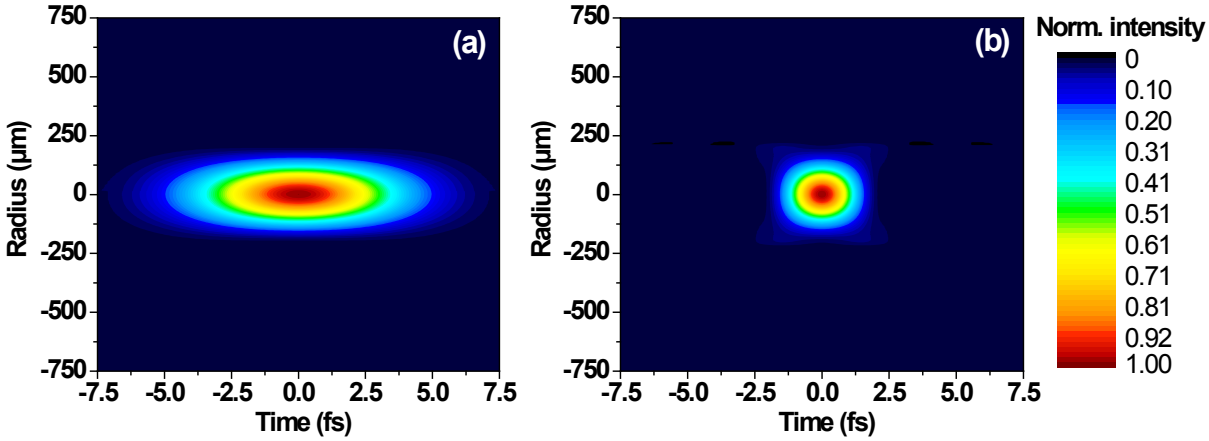

Fig. 2.2.3 Spatiotemporal structure of pulsed needle beams for two different pulse durations: **(a)** τ = 6 fs and **(b)** τ = 2.66 fs (corresponding to a single cycle pulse at 800 nm). Here, a weak X-structure can be recognized around the central bullet. Simulation parameters: center wavelength at λ_0 = 800 nm; conical angle θ = 1.8 mrad; axicon radius R = 450 µm.

Such ultrashort wave packets remain the advantages of nondiffracting propagation but are not corrupted by an oscillating radial intensity distribution, which means they reach an increased spatial localization in comparison to Bessel beams of multiple concentric fringes. The pulse structure is maintained over the entire nondiffracting zone. The shorter the pulse the higher the localization in space and time. For much shorter pulses (≤ 2.66 fs), residuals of the typical X-structure of pulsed Bessel beams appear also in the space-time characteristics of pulsed needle beams. But even without truncation such beams show a higher degree of localization (sharp central peak on an increasing unstructured pedestal). A change in the spatiotemporal behavior can be verified in *Fig. 2.2.3* where few-cycle (6 fs) and single-cycle (2.66 fs) needle pulses are compared. In the example the axicon angle and size were chosen to be θ = 1.8 mrad

and R = 286 µm, respectively. Note the slightly flattened spatiotemporal shape at low intensities which is due to the special interference structure obtained by superimposing conical waves.

Needle beams are of pure paraxial type (small angles to the optical axis) as Gaussian beams, however, they do not show a Gaussian-type beam propagation. For this reason, the new types of nondiffracting beams require adequate methods for the characterization and description in space and time. A first approach to evaluate the propagation characteristics of needle beams was based on a confined definition of the temporal and spatial beam quality factors P^2 and M^2. Applying the known beam quality factor for Gaussian beams in the spatial domain reveals that this definition is incomplete or incorrect for Bessel-like or needle beams. Because Bessel beams show a transversal oscillation, a reformulation of the quality factor is hardly trivial. However, for oscillation-free needle beams it is possible to find a solution. A promising approach based on the definition of the Gaussian beam quality factor is described by the relationship:

$$\theta = M^2 \frac{\lambda}{\pi w_0}. \tag{19}$$

The relationship results from the property that the beam parameter product θw_0 of a Gaussian beam is a constant for the corresponding wavelength. Such a parameter product exists also for needle beams where the half beam divergence angle is intrinsically determined by twice the axicon base angle (conical angle):

$$\theta = \frac{\lambda}{R}. \tag{20}$$

The standard deviation σ_{NB} of the intensity profile of an ideal needle beams becomes in good approximation:

$$\sigma_{NB} \approx \frac{R}{6} \tag{21}$$

For needle beams, the following beam parameter product applies:

$$\theta \cdot \sigma_{NB} = M_{new}{}^2 \frac{\lambda}{\pi}. \qquad (22)$$

This equation is similar to the relationship of the quality factor for Gaussian beams, but in this case the divergence angle is given by the conical angle introduced by the axicon. By inserting equation (20) and (21) in equation (22) one obtains a lower limit of the needle beam quality factor assuming perfect conical waves of a single k-vector (delta function in the far-field):

$$M_{new}{}^2 = \frac{\pi}{6} \approx 0.52, \qquad (23)$$

yielding a calibration factor of $CF = 6/\pi$. The calibration factor is necessary to renormalize the quality factor. Another ansatz to calculate the quality factor is:

$$M^2 = 4\pi\sigma_0\sigma_\infty. \qquad (24)$$

The modified quality factor is then attributed to:

$$M_{NB}{}^2 = CF \cdot 4\pi\sigma_0\sigma_\infty = \frac{6}{\pi} \cdot 4\pi\sigma_0\sigma_\infty = 24 \cdot \sigma_0\sigma_\infty, \qquad (25a)$$

where σ_0 represents the standard deviation in the near-field whereas σ_∞ defines the center position of the involved spatial frequencies (ring distribution) measured in the far-field.
As usual, a quality factor of $M_{NB}{}^2 = 1$ indicates a perfect needle beam and the absolute minimum value. Further it is necessary to introduce an axially dependent quality factor $M_{NB}{}^2(z)$ for the simple reason that needle beams do not possess a beam waist at an explicitly defined axial spatial position as it is the case for Gaussian beams:

$$M_{NB}{}^2(z) = 24 \cdot \sigma_0(z)\sigma_\infty. \qquad (25b)$$

In analogy to the spatial beam quality (as mentioned above), the temporal shape of ultrashort pulses can formally be described by a pulse propagation factor P^2 [Rou02] assuming that spatial variations in the spectral and temporal properties of the pulse are negligible and independent from M^2 :

$$P^2 = 4\pi\sigma_\nu\sigma_t\,, \tag{26}$$

wherein σ_ν and σ_t represent the variances in spectral and temporal domain, respectively. Moreover, a dimensionless spatiotemporal localization parameter L^2 of an ultrashort-pulsed wave packet is defined by the root of the product of M^2 and P^2:

$$L^2 = \sqrt{M^2 \cdot P^2}\,. \tag{27}$$

If complex space-time couplings are involved it is more appropriate to find a suitable description of the propagation properties based on a spatially and temporally dependent energy flux. Thus, a simple description of such pulses by one quality factor becomes senseless.

Another aspect of finite Bessel-like beams is attributed to the axial dependent shift of the phase through the focus, which is well known as the Gouy phase shift [Gou90]. This property is a direct consequence of the superposition of plane waves consisting of a single wave vector or spectrum of wave vectors (spread of transverse momenta due to apertured beams of finite energy) each contributing by an additional phase shift. Consequently, the Gouy phase shift is a result of the transverse spatial confinement of light as valid for both Gaussian and Bessel beams. First observed by Gouy in 1890 the total phase shift for Gaussian beams focused by a convex lens is exactly π when the beam propagates from -∞ to +∞ but only $\pi/2$ for cylindrical lenses. The axial dependence for a TEM_{00} mode is calculated by the relation $\varphi_{\mathrm{Gouy}} = arctan(z/z_0)$ [Fen01]. In contrast, Bessel beams show a linear dependence specified by [Tac10]:

$$\varphi_{Gouy} = (k - k_z)z = \frac{k_r^{\,2}}{k + \sqrt{k^2 - k_r^{\,2}}}\,z\,. \tag{28}$$

The importance of the Gouy phase shift becomes clear when considering that the carrier-envelope phase of few-cycle pulses experiences the same shift during the propagation through the focus. Such a behavior is of particular relevance in linear and nonlinear light matter interactions [Fen98, Lin04]. For microscopic needle beams generated by ultraflat microaxicons and approximately flat input wavefronts, the contribution of the Gouy phase at the end of the Bessel zone should be exactly reach the value π.

2.3 Physical importance of highly localized wave packets (HLW)

To conclude, the generation and control of localized wave packets has been of long-standing interest in ultrafast optics. Obviously, the degree of localization strongly depends on the pulse duration and the spatial dimensions of the beam as well as the coupling between both. Shaping the spatial properties without influencing the temporal properties is a challenging task whereas the difficulties increase at extreme parameters (like micrometer dimensions and few-cycle pulses). In the previous paragraph it was described under which conditions highly localized and nondispersing, nondiffracting wave packets are achieved simultaneously and how they behave in space and time during the propagation.

Needle beams enable a nearly undisturbed propagation of ultrashort pulses over a large axial depth. In addition, diffraction effects can be further reduced by supergaussian-like shapes, shifting the disturbing influence of finite apertures to other axial planes. Moreover, “smoothed axicon edges“ further increase the compatibility to ultra-broadband polychromatic pulsed Bessel beams and the axial-dependent narrowing of the transversal Bessel zone. In fact, this unique characteristics become more important if one realizes that conventional pulsed Bessel beams show a spatially dependent pulse duration due to a spatial chirp introduced by the specific spectral interference [Gru08]. In the case of very short pulses the localization of the X-wave increases and an extremely sharp spatial peak without oscillations is generated, not only highly localized in axial direction but also in the transversal direction. Together with a mono-cycle in the time-domain (2.7 fs) such wave packets present the ultimate localization in space and time (4D) propagating in a nondiffracting manner over large distances (“the ultimate light bullet”). Due to the propagation behavior, needle beams can be regarded to be the physical approximations of "rays" and allow a very flexible structuring of light for example with respect to realize a robust method for a lensless image relay (“flying images”). At extremely small conical angles, the resulting beams show super-collimation properties. In certain applications it is of huge interest to have those kind of beams, for instance, detecting wavefronts of ultrashort pulses according to the Shack-Hartmann principle and improving existing ultrashort pulse characterization methods. Wavefront and pulse diagnostics (spatially resolved 2^{nd} order autocorrelations) can be realized in a common compact setup. Consequently, according to the unique features, fringe-free nondiffracting beams are of particular interest for reasons of fundamental optics as well as practical applications in the fields of micro materials processing, microscopy, highly sensitive wavefront measurements and laser beam homogenizing.

In the past, aside from the need of nonspreading wave packets, physicists also paid much attention to the free-space nondiffracting propagation of optical patterns or images in relation to different experimental approaches. Nevertheless, they all based on the same fundamental principle – the interference of plane waves.

Ideal nondiffracting fields are a coherent superposition of plane waves (also nondiffracting) with propagation-invariant relative phases. The fundamental boundary conditions to obtain spatially stable propagating beams is that the k-vectors of the plane waves should preferably lie on a conical surface as already explained in the previous paragraph. However, amplitude and phase can be arbitrarily modulated to generate new patterns. On the basis of binary circular gratings, which were programmed into an SLM, Bessel beams of higher order and combinations were realized [Dav96]. Furthermore, it has been reported that also double Bessel beams can be shaped from diffractive optics [Ket98]. A complete control of the phase and amplitude of the angular spectrum enables a wide spectrum of realizable nondiffracting patterns, however this was only shown for incoherent and coherent monochromatic beams [Bou02]. Also random nondiffracting patterns generated by means of a spatial light modulator have been reported [Cot07]. It is even more challenging to realize pulsed nondiffracting patterns because of the difficulties in spatial filtering and Fourier transformation of broadband coherent light sources.

Thereby, the main emphasis of this thesis is laid on adaptive generation (via SLM) of such beams and their properties in relation to their spatiotemporal dynamics. In addition, an adaptive-optical beam shaping approach for ultrashort pulses delivers a sufficient number of degrees of freedoms to generate other nondiffracting light fields than needle beams. The definition of a basic set of highly localized waves is a very new approach and promises an extended access to manipulate and control the properties of ultrashort pulses in a wide range of experiments. The next chapters are focused on the experimental realization and analysis of such rotational symmetric and asymmetric HLWs in space and time, confirming the theoretical approach.

2.4 Optical angular momentum

2.4.1 History and definition

The angular momentum of light was first theoretically investigated by Poynting [Poy09]. Like Maxwell he addressed that one can assign a mechanical property to light. Both associated this phenomena with circularly polarized light or with the spin of a photon, respectively. A first measurement was performed in 1936 by exploiting the induced torque of a double refractive plate suspended on a fiber [Bet36]. Optical vortices in light fields caused by phase singularities were studied by Nye and Berry [Nye74]. During the research with coherent or partially coherent optical fields it was recognized that sometimes dark spots appear within the beam or forked structures of interference patterns. Laser speckles, for example, have their origins in randomly superimposed optical vortices [Bar83]. Mechanical effects induced by an orbital angular momentum (OAM) were first recognized by Allen and co-workers in 1992 [All92].

Historically, the nature of an intrinsic angular momentum was attributed to the spin momentum of light appearing independently from the chosen axis. For the orbital momentum it was incorrectly concluded that the property is completely extrinsic. That misleading interpretation was forced by the understanding of a particle spinning around its own axis (intrinsic) or orbiting around one point (extrinsic orbital momentum). Furthermore, the typical spatial (spiral) phase distribution around the singularity suggests that the orbital momentum might have a central axis and thus an extrinsic property only. The mechanical equivalence was proved for the spin momentum of circularly polarized light and the orbital momentum of $\ell = 1$ beams [Sim97]. For light fields the spin angular momentum is always intrinsic. An unambiguous assignment for the orbital angular momentum, however, remains still controversial. Berry et al. showed that the orbital momentum of particular Laguerre-Gaussian beams is always intrinsic as long as the direction of the observing axis is chosen carefully with respect to a zero transverse momentum.

Therefore, the OAM is an intrinsic or quasiintrinsic property of light (photons) – a photon phase property [Zam06]. However, when the transverse momentum is nonzero (e.g. the OAM beam is passed through an off axis aperture) the OAM has extrinsic properties. It must be explicitly stated that the manifestation of an intrinsic or extrinsic behavior depends on the specific interaction with particles [Nei02]. Nevertheless, with the possibility to create light field carrying an OAM surprising physical consequences and applications arise, e.g. enabling

the possibility to prepare a higher dimensional state space for a massive parallel quantum processing (encoding a large alphapet) [Mol07, Ber10].

A spin angular momentum is well-known as the rotation of the magnetic and electric field around the propagation vector (circularly polarized light) and can attain values of $\sigma\hbar$ per photon with $\sigma = \pm 1$. For $\sigma = 0$ the beam appears linearly polarized consisting of right- and left-handed circularly polarized light. In contrast, the orbital momentum is related to a rotating phase front distribution and is usually not coupled to the polarization of the optical field. The orbital momentum per photon is defined as $\ell\hbar$ where ℓ represents the topological charge as an integer or noninteger variable. This description was derived within the paraxial approximation of optical vortices and was approved within a fully non-approximated calculation of the angular momentum density M_{orb} which is [Bar02]:

$$M_{orb} = \varepsilon_0 \vec{r} \times \left(\vec{E} \times \vec{B}\right). \tag{29}$$

Here E, B and r represent the electric field, magnetic field and the radial distance, respectively.

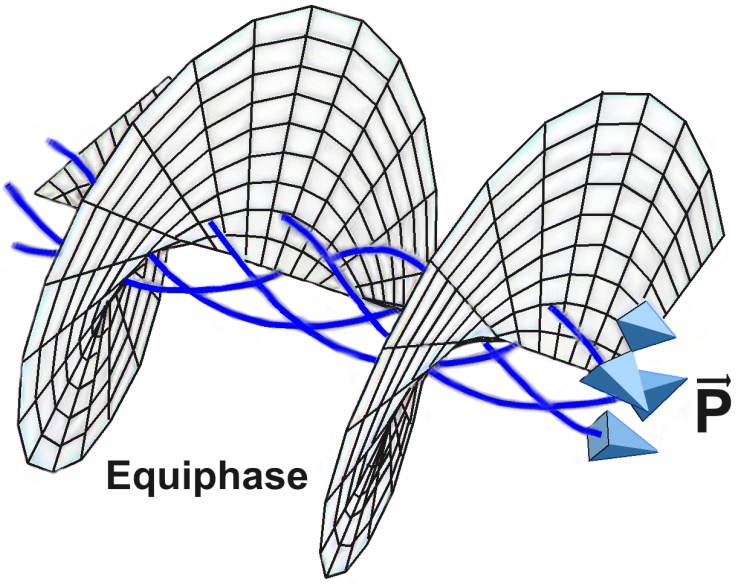

Fig. 2.3.1 Spatial evolution of the wavefront phase and the corresponding Pointing vector of an orbital momentum beam of charge $\ell = 1$ [All03].

The product of the topological charge ℓ and the wavelength λ can be understood as a quantitative measure of the change in the phase of light at a full rotation of the azimuthal angle pointing in the direction perpendicular to the axis of the singularity. The equiphase surface has a form of a helix with a pitch (on-axis periodicity length) of $\ell\lambda$. In this case the

Poyinting vector possesses a component in azimuthal direction winding in a loop around the wavefront helix. Consequently, the evolution of the corresponding total pointing vector is intertwined around the beam axis which is schematically drawn in *Fig. 2.3.1*. In cylindrical coordinates for a fixed radial position, the phase dependence is $\ell\xi$. That means for a full rotation the phase of the electric field changes by a factor of 2π even though the phase at $r = 0$ is completely uncertain. The intensity must vanish at this point. As mentioned before, the azimuthal components circulate. More specifically, a closed line integral delivers in any case

$$\oint \nabla\xi(r)dr = \oint k(r)dr = -2\pi\ell \,, \tag{30}$$

independently on the radial position. The variable $\nabla\xi(r)$ is defined as the phase gradient and k as the wave number.

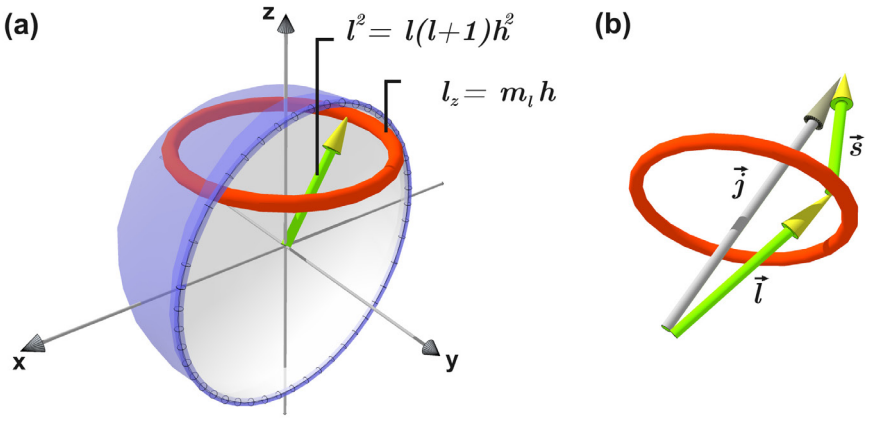

Fig. 2.3.2 Spin and orbital angular momenta: **(a)** Exemplary representation of the orbital angular momentum. The vector length is $\hbar[l(l+1)]^{1/2}$ with a z-component $m_l\hbar$. **(b)** The total angular momentum can be calculated by summing up spin ***s*** and orbital ***l*** vectors.

Based on the Huygens-Fresnel principle, all points on the circle radiate spherical waves which interfere with each other. The phase difference of two symmetric and opposite points is always π with respect to a virtual center. Destructive interference occurs and a dark spot appears in the center. By mixing different topological charges it becomes evident that fractional topological charges can also be realized. However, the resulting beam profile is affected by an azimuthally varying intensity distribution [Lea04, Gut08].

Nevertheless, the property of photons has a quantum mechanical origin. *Fig. 2.3.2* shows the orbital and total angular momentum for a photon [All92, Enk94, Pad00b, Mol07]. The spin angular momentum of a photon comes in two varieties: left handed or right handed. Then linearly polarized light must be a mixture of left and right circularly polarized light. But if the

photon density is reduced to the single photon level the measured momentum should either be left or right handed. In the case of linearly polarized light, the probability is then 50:50. Experiments showed that this is in fact true but it is not the probability of an ensemble of photons, it is rather a quantum meachanical probability of a single photon. This non-classical property, this uncertainty of a photon is only accessible according to the present knowledge by describing it by a superposition of left and right handed spin momenta. Apart from the difficulty that neither spin nor orbital angular momentum are describing the nature of a photon sufficiently, it turns out that an angular momentum flux (photon fluid) is more convenient to describe optical vortices than the angular momentum density [Bar02]. The theory confirms the ratio of angular momentum to energy (ℓ/ω) which was earlier given by the paraxial approximation but it shows that the ratio is independent on the degree of focusing.

2.4.2 Generation of optical vortices

In fact, vortices emerge in fluids (superfluids) or in global weather patterns (cyclones) but it was surprising that in frame of modern optics also light fields can rotate with an orbital angular momentum. In the past two decades a lot of research was spent on the generation and usage of optical vortices.

Such twisted fields enable to consider new applications in optical data storage techiques, optical free-space communications, astrophysics, micromechanics or quantum optics. Optical tweezers, for instance, are the most known and well-developed technique to trap and rotate particles. Related to this, also the influence of amplitude, phase and polarization on tightly focused vortex beams was investigated in frame of the conversion of SAM to OAM within the focal plane. An overview can be found in [Che12]. Apart from controlling optical vortices with linear methods the interaction with a nonlinear material opens a new parameter space for shaping. Much attention is therefore paid to the second harmonic generation [Dho96, Cou97], four-wave mixing [Len11] and the generation of vortex solitons [Chr96, Kiv98] in order to improve existing physical measuring techniques (microscopy, spectroscopy, etc.). Here, the order of the OAM of frequency converted vortex beams is dictated by the conservation of the angular impulse.

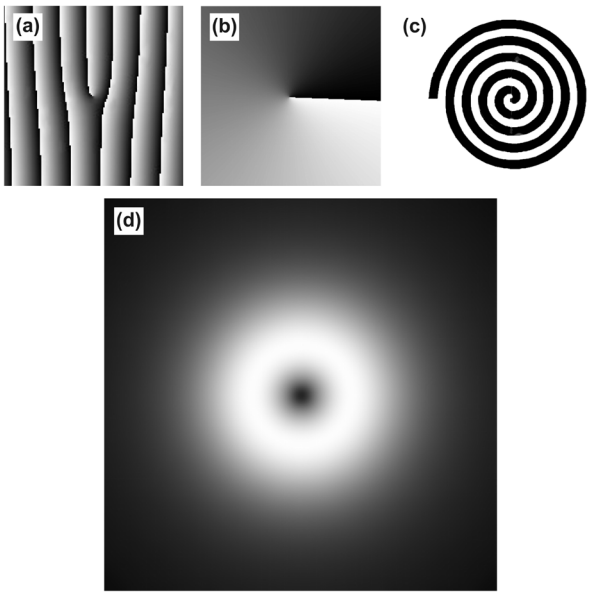

Fig. 2.3.3 Generation of an orbital angular momentum beam of ℓ=*-1* under Gaussian beam illumination: **(a)** Holographic single forked structure, **(b)** spiral phase distribution (gray levels from 0 to 255 correspond to phases between 0 to 2π), **(c)** spiral binary phase grating, **(d)** Gaussian doughnut mode obtained in the far-field of the particular optical element. Note that for holographic gratings the orbital momentum beam appears in the higher diffraction orders > 1.

Generation methods:

There are three branches to generate optical vortices, first, spiral phase distributions, second, Hermite-Gaussian converters, and third, diffractive optics as summarized in *Fig. 2.3.3*. The exact intensity distribution and phase properties within the focal plane are generally coupled to the focusing conditions. That means, for instance, by using a spherical lens one obtains a Laguerre-Gaussian beam in the focal plane. Alternatively, a Bessel-Gaussian beam is generated when using an axicon.

The easiest and most intuitive scheme for the conversion of a flat to a helical wavefront consists of a refractive spiral phase plate (SPP) [Kho92]. The topological charge is directly given by the pitch height h proportional to integers of the wavelength λ. The total height is defined by $h = \ell\lambda/(n_{SPP}-n)$ where n_{SPP} is the refractive index of the plate and n of the surrounding medium. The plate height itself is a function of the azimuthal angle ξ plus an additional constant basic height h_0:

$$h(\xi) = \frac{\ell\lambda}{(n_{SPP} - n)} \cdot \frac{\xi}{2\pi} + nh_0 \,. \tag{31}$$

The phase delay is then calculated as follows:

$$\varphi(\xi) = \ell\xi + \varphi_0 \text{ with } \ell = \frac{h(n_{SPP} - n)}{\lambda}. \tag{32}$$

As one can derive from the above equation for the phase delay, chromatic aberrations are intrinsically involved. This property is a significant disadvantage if the plate is illuminated by a polychromatic beam and ultrashort pulse, respectively. Then the condition for an integer vortex beam is only fulfilled for the original design wavelength. For non-integer values of ℓ the azimuthal intensity distribution appears to be disturbed or interrupted [Ber04, Gut08]. Moreover, difficulties in the manufacturing process arise due to the radially dependent steepness of the ramp in the central region.

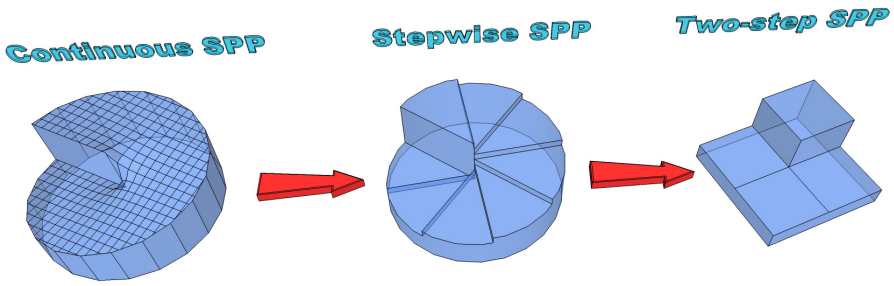

Fig. 2.3.4 Continuous, stepwise and two-step spiral phase plate for optical vortex generation (schematically).

The second method is given by transforming Hermite-Gaussian beams by a combination of two cylindrical lenses. The lenses are separated by $\sqrt{2}f$. The input mode is aligned in 45° to the principal axis of the parallel-oriented cylindrical lenses. As completely described in [Bei93] a Hermite-Gaussian beam, for example, of H_{10} and 45° orientation can be separated into a H_{10} and H_{01} mode. The specified lens distance ensures a Gouy phase shift (additional axial phase shift in Gaussian modes according to an on-axis plane wave) of 90° between the two modes. Therefore, a Laguerre-Gaussian beam of L_{10} is formed by superposition at the lens output.

Diffractive optics, the third branch, comprises diffractive optical elements, holographic optical elements, gratings and computer generated holograms for the vortex generation. Such optics are defined by their periodic structures. If a vortex beam interferes with a plane wave, its superposition generates an interference pattern showing single- or multi-forked discontinuities in the center. This holographic principle allows a reconstruction of vortices from appropriately designed holograms [Baz90, Hec92]. The required forked structures can either be imprinted in ordinary glass substrates or programmed into a spatial light modulator as a digitally generated hologram with a high flexibility. In both cases, a binary or multilevel pattern can contain more than a single dislocation whereas the number and arrangement can

be chosen arbitrarily. At the output, the required OAM with ℓ intertwined wavefronts is deflected into the first diffraction (off-axis) order. This reconfigurability enables an easy systematic study of vortices in optical light fields.

In contrast to that, vortex generation with diffractive optical elements occurs along the optical axis with low diffraction losses, so that the efficiency is generally higher. A staircase-like spiral phase plate is such an optical element as indicated in *Fig. 2.3.4*. Generally, a spiral phase plate can be reduced from a continuous behavior of the height to a certain number of heights or phase steps, respectively. An extreme example would be to have only two phase steps, 0 and 2π [Kim97]. The individual plateaus are oriented parallel to each other.

Spiral gratings:

The same effect of an SPP is obtained by spiral gratings. Beam dispersion and focusing are exclusively realized in terms of diffraction. The wave vector directions are sharply restricted to a cone thus resulting in localized waves with a vortex structure. The required azimuthal phase modulation is ensured by appropriate time delays of the diffracted light. While diffractive spiral axicons are associated with grooves of constant width and duty cycle winding around the symmetry axis, diffractive spiral lenses (Fresnel zone plates) consist of non-equidistant groove widths and duty cycles. They typically decrease with the radius. In general, such spiral optics are realized in a blazed or quantized fashion. The former is further classified into index gratings and grooves with surface profile. The latter exists as multilevel phase gratings and binary phase or amplitude gratings. Here, the different diffraction efficiencies are essentially influenced by the applied structure. To fully understand, for example, the light guiding and spot shaping of a blazed phase grating one has to take diffraction and refraction (deflection) into account.

The most important feature of diffractive optics is the great flexibility in controlling the spatiospectral and spatiotemporal behavior of focused ultrashort pulses especially for the realization of ultrashort vortex pulses with a high spatial and temporal contrast [Lõh12]. It is shown in experiments that such diffractive axicons are able to keep also few-cycle pulses short (3 cycles of the electric field) within the nondiffracting zone, see below in chapter 4.7. The spectral phase tuning and spatiospectral overlap is simply achieved by the angular dispersion of the grating. However, diffractive optics are not efficient as much as beam converters dealing with the concept of mode transformation.

Binary spiral gratings:

In the following, the main focus lays on binary spiral phase gratings because such gratings are later used to realize pulsed Bessel beams of the first kind. The following grating equation is valid for all gratings with a constant period:

$$\sin(\theta)+\sin(\gamma)=\frac{m\lambda}{p_g}=\frac{m2\pi c}{\omega p_g}. \qquad (33)$$

In this formula, θ represents the diffraction angles of the intensity maxima measured to the normal axis of the grating when light with of the wavelength λ incidence on the grating at an angle γ. The diffraction angles are further determined by the grating period p_g and diffraction order m. Since the light is deflected along several discrete paths on either side of the grating normal, convergent as well as divergent contributions to the interference pattern are generated. The order of diffraction is determined by the positive or negative sign of m. The circularity ensures that all diffraction orders are deflected along a conical wavefront whereas only convergent parts contribute to the generation of the localized wave in the far-field (Fraunhofer diffraction with Fresnel-numbers << 1). For typical grating periods of 10 µm, the far-field is reached in good approximation when the axial distance exceeds 2.5 mm. It should be noted that multiple foci (Bessel zones) are obtained because of several diffraction orders. It is evident that the focal spot shifts closer to the grating for increasing diffraction orders. The position and strength of each spot is determined by the grating period and diffraction efficiency (groove shape and depth), respectively. For polychromatic illumination the overall behavior is a bit more complicated explained later on.

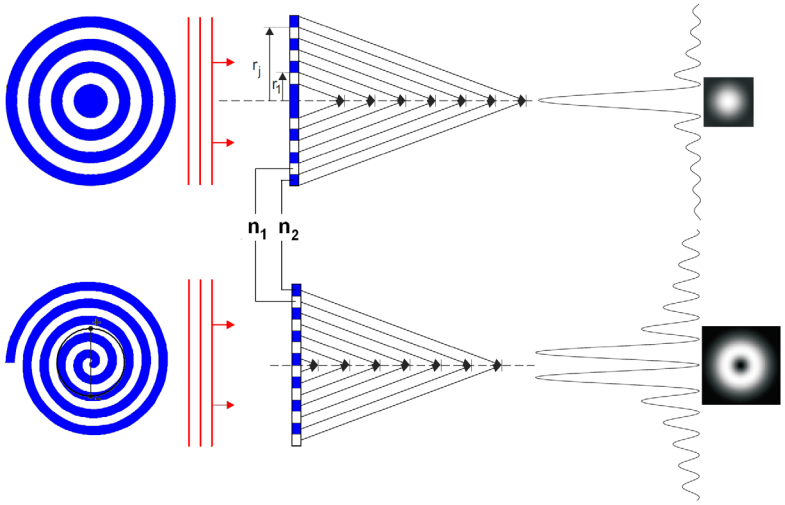

Fig. 2.3.5 Grating shapes of a concentric (top) and a spiral (bottom) diffractive axicon generating Bessel beams of zeroth- and first-order. The contrast of the phase grating is determined by the resulting phase difference of two different refractive indices [Ric09].

In the simplest case, a grating with concentric rings (without a spirality) generates a Bessel beam of zeroth-order whose length and axial structure depend on the grating period. In *Fig. 2.3.5* it is schematically visualized that constructive interference takes place on the optical axis. Each symmetric diffracted part requires the same optical path length. In contrast, a single spiral introduces a phase shift of π between opposite diffracted parts so that destructive interference occurs. Arbitrary angular spectra and time delays may be synthesized by modifying the spatial structure of the phase plate. In this way the numerous design parameters enable a tailored shaping of localized waves in space and time.

Since few-cycle ultrashort pulses exhibit a broadband optical spectrum one has to go deeper into investigating the optical properties of a grating. From the grating equation it directly follows that each frequency component has its own conical angle where the angle increases with decreasing wavelength. This fact becomes very important particularly with regard to a spatial overlap of each spectral component in polychromatic Bessel beams. The spatial frequency of the Bessel function is inversely proportional to the optical wavelength:

$$\nu(\lambda) = \sin(\theta)\frac{1}{\lambda} \ . \tag{34}$$

By substituting *sin(θ)* that is now a function of the grating period p_g the new relation exhibits no dependence on the wavelength:

$$\nu(\lambda) = \frac{\lambda}{p_g}\frac{1}{\lambda} = \frac{1}{p_g}. \tag{35}$$

Here, an angle of incidence normal to the grating surface was assumed. A spatial overlap on the one hand tells nothing about the spectral phase relations on the other. For this purpose the pathways and resulting time delays have to be analyzed for a broadband (polychromatic) illumination. The geometrical path difference L for a normal incidence is simply defined by the geometrical relation:

$$L(\theta) = \frac{z}{\cos(\theta)}, \tag{36}$$

where z represents the distance on the optical axis from the grating. The group delay $d\varphi/d\omega$ is then:

$$\frac{d\varphi}{d\omega} = \frac{L(\theta)}{c} = \frac{z}{c\cos(\theta)}. \tag{37}$$

The derivative leads to the definition of the group delay dispersion:

$$\frac{d^2\varphi}{d\omega^2} = \frac{1}{c}\frac{dL(\theta)}{d\omega} = \frac{z}{c}\frac{d\left(\cos(\theta)^{-1}\right)}{d\omega}. \tag{38}$$

By constraining the subsequent considerations to a perpendicular incidence (based on equation (33)) and the first diffraction order, the cosine of the diffraction angle is written in the form:

$$\cos(\theta) = \sqrt{1-\frac{4\pi^2c^2}{\omega^2 {p_g}^2}}. \tag{39}$$

Then, the group delay becomes [Mar84]:

$$\frac{d^2\varphi}{d\omega^2} = -\frac{4\pi^2 zc}{{p_g}^2\omega^3}\left(1-\frac{4\pi^2c^2}{{p_g}^2\omega^2}\right)^{-\frac{3}{2}}. \tag{40}$$

The negative sign implies that a positive material dispersion of second order is needed to obtain a flat phase neglecting dispersion contributions of higher orders. However, an approximated flat phase is only obtained at a certain distance z depending on the chosen grating period and the inserted material. This concept is predestined to extend the dispersion control, for instance, by separating the diffractive axicon into distinct zones of different grating periods. This enables to form a short focused X-pulse in a large depth of field by adapting the grating period to the focusing conditions. The method represents a particular kind of pulse shaper based on direct space-to-time conversion such as referred in [Min08].

2.4.3 Detection of optical vortices

Because of the enormous diversity of the generation methods, the detection of angular momenta is challenging as well. An azimuthal Doppler shift [Cou98], triangular apertures [Ara11], holography (interference with a plane wave) [Bar83], forked diffraction gratings [Gib04] or refractive optical elements [Lav12] are methods that measure the total angular momentum quantitatively. But with all these techniques a spatial resolution is achieved only to a limited degree. The detection of the intertwined phase fronts is much more applicable, especially with respect to ultrashort pulses, with the usage of a sensors based on the Shack-Hartmann principle [Pad00a, Che08]. Here, the specific advantages of needle beams can be brought to bear.

The Hartmann method of detecting wavefronts of light fields lies on the assumption that a beam is approximated by beam rays. The division of light fields into cells (e.g by arrays of pinholes) enables to measure the local tilts of the wavefront at discrete positions [Har00]. The pinholes ensure a separation and discretization of the bundle of light rays. The spatial arrangement of the pinholes is not restricted to a periodic arrays. Arbitrary patterns are possible, however, due to the manufacturing efforts in the past hexagonal or rectangular arrays were preferred. Each generated sub-beam behind the pinholes denotes the direction of propagation (Poynting vector) at the respective spatial position. This type of wavefront measurement was extended by using microlenses instead of pinholes with the great advantage that nearly the entire light energy is transferred through the sensor or microlens, respectively [Sha71]. Here, the sub-beam is deflected in a certain direction (x or y-direction) depending on how the lens with a focal length f was illuminated, either perpendicular or angular to the optical axis:

$$\begin{pmatrix} \delta x \\ \delta y \end{pmatrix} = \begin{pmatrix} f \tan(\gamma_x) \\ f \tan(\gamma_y) \end{pmatrix}. \tag{41}$$

If the lenses are sufficiently small each respective part on the wavefront is assumed as flat but tilted. The smallest detectable tilt ζ of the wavefront part by assuming small angles is given by the relation:

$$\zeta_x = \frac{\delta x_{\min}}{f} \quad \text{or} \quad \zeta_y = \frac{\delta y_{\min}}{f}. \tag{42}$$

It turns out that the minimum value for a detectable spot shift is determined by the physical properties of the detector array (pixel size, with or without light collecting lenses etc.). For elongations below this value, an increase of the deflection angle is obtained by choosing longer focal lengths. Keep in mind that in most cases, the maximum beam deflection is restricted to the unit cell of the observed spot to ensure a consistent and uniform spot association. The active principle is illustrated in *Fig. 2.3.6*. As already addressed above, a spot shift *(δx, δy)* on the detector can be observed for curved wavefronts. This enables the computation of the input wavefront if the positions relative to typical spot pattern of a reference plane wave (related to equidistant spot positions) are known. The amplitude of deflection (resulting shifts) in x- and y-direction are a measure of the 1st order derivatives (local slopes) of the wavefront:

$$\vec{W}(x,y) = \begin{pmatrix} \dfrac{\partial W(x,y)}{\partial x} \\ \dfrac{\partial W(x,y)}{\partial y} \end{pmatrix} = \frac{k_0}{f} \begin{pmatrix} \delta x \\ \delta y \end{pmatrix}. \tag{43}$$

Requirements for a correct measurement are (i) a continuous and differentiable wavefront and (ii) a less distinct defocus. Conventional microlenses generate spots which are influenced by spatial and chromatic aberrations. Furthermore, the depth of field is restricted by the type of focusing (Gaussian beam propagation). All these parameters have an influence on the measurement accuracy and dynamic range of the setup. These drawbacks are successfully reduced if ultraflat axicons are implemented. The generated sub-beams (see chapter 4.6) are robust against tilt, nondiffracting over a large axial depth and suitable for ultrashort pulses [Gru07, Gru08].

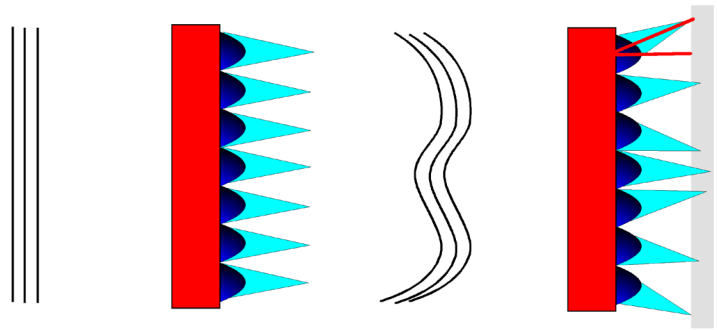

Fig. 2.3.6 Shack-Hartmann principle of detecting wavefronts with arrays of microlenses: For a plane wave illumination (left picture) all spots positions are equidistant to each other whereas a curved wavefront deflects the sub-beam in the corresponding direction.

The wavefront is obtained by integrating over the displacement map. Here the integration in x-direction yields:

$$W(x) = \frac{k_0}{f} \sum_{n=1}^{N} \left(\frac{\delta x_{n-1} + \delta x_n}{2} \right) \Delta x_{n-1}, \tag{44}$$

whether microlenses or axicons are used. Because of discrete values of the shift, each for every lens, the integration is performed numerically on the basis of the trapezoidal rule. The gap between two spot positions is considered by the variable Δx. The same is valid in y-direction.

Usually, an orthogonal set of mathematical functions, called Zernike polynomials Z_n, are used to describe the wavefront and its aberrations. In this frame, the polynomials are curve-fits to the measured data. However, a single Zernike cannot contain more than one type of variation (e.g. tilt, defocus or coma). Typically, the expression for the wavefront fit is then a linear combination of Zernike polynomials containing all these partial contributions with weighting factors b_n:

$$W(\upsilon) = b_0 Z_0(\upsilon) + b_1 Z_1(\upsilon) + b_2 Z_2(\upsilon) + \ldots = \sum_{u=0}^{n} b_n Z_n(\upsilon). \tag{45}$$

Zernike polynomials represent different shapes notated with indices of radial order $\tilde{n}$ and frequency order $\tilde{a}$. The radial order (degree of the polynomial) measures the radial function across the meridian whereas the frequency (angular-dependent parameter) specifies the number of peaks and valleys. That means, for example, the frequency order can show a sinusoidal function or be constant. The latter one implies radial properties of the wavefront. The Zernike polynomials are defined as follows [Wya92, Bor99]:

$$Z_{\tilde{n}}^{\tilde{a}}(\upsilon,\eta) = U_{\tilde{n}}^{\tilde{a}} \cos(\tilde{a}\,\eta) \qquad \text{for } \tilde{a} > 0, \tag{46}$$

$$Z_{\tilde{n}}^{\tilde{a}}(\upsilon,\eta) = U_{\tilde{n}}^{\tilde{a}} \sin(-\tilde{a}\,\eta) \qquad \text{for } \tilde{a} < 0, \text{ and} \tag{47}$$

$$Z_{\tilde{n}}^{\tilde{a}}(\upsilon,\eta) = U_{\tilde{n}}^{\tilde{a}} \qquad \text{for } \tilde{a} = 0, \tag{48}$$

where the radial polynomials U are defined by

$$U_{\tilde{n}}^{\tilde{a}}(\upsilon)=\sum_{u=0}^{\frac{(\tilde{n}-\tilde{a})}{2}}\frac{(-1)^{u}(\tilde{n}-u)!}{u!\left[\frac{(\tilde{n}+\tilde{a})}{2}-u\right]!\left[\left(\frac{\tilde{n}-\tilde{a}}{2}-u\right)!\right]}\upsilon^{(\tilde{n}-2u)}. \tag{49}$$

Here the variables η and υ are related to the azimuthal angle and the normalized radial distance.

Conventional Zernike polynomials are not the best fitting curves when dealing with vortex beams. Therefore, a modified mathematical description is proposed in [Uri10] called OAM-Zernike basis. Nevertheless, for some purposes the displacement data (vector field) as a measure of the local phase gradient are entirely sufficient, e.g. only the topological charge has to be known. From the helical behavior of the Poynting vector (azimuthal + radial part) the screw angle of a vortex beam [Pad00] is derived and has the following relation to the topological charge ℓ, the wave number k and the radial coordinate r:

$$\varsigma_{theory}(r)=\frac{\ell}{kr}\ . \tag{50}$$

The corresponding vector field to this equation is illustrated in *Fig. 2.3.7* where the vector length increases with 1/r to infinity at the center of the singularity.

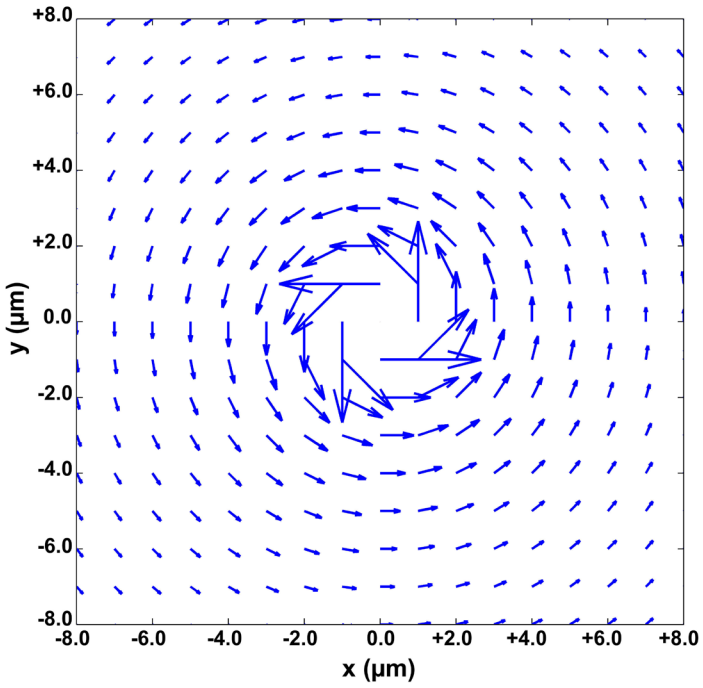

Fig. 2.3.7 Vector plot of the gradient of the phase in the proximity of a phase singularity (center) as it would appear for a left-handed ℓ = 2 vortex beam of microscopic dimension. The screw angle decreases inversely proportional to the radius (here: normalized radius). For illustrative purpose, the vectors are shortened by a factor of 6.

The Shack-Hartmann approach is exploited to observe such a behavior of propagating optical vortices with a high accuracy. This non-interferometric technique has the advantage over other methods that it performs a direct and unambiguous spatially resolved measurement of the OAM with a single shot. The screw is then directly derived from the vector field of the spot shifts:

$$\varsigma_{measured}(r) = \arctan\left(\frac{\langle sh(r,\eta)\rangle}{z}\right)\cdot V \,. \tag{51}$$

where z represents the distance to the lens or axicon matrix. For statistical reasons the measured shift length *sh(r)* is averaged over the azimuthal angle. Furthermore, a magnification factor V is added to the equation to consider also increasing or decreasing screw angles (by inserting a microscope objective or a telescope lens) by possible optical imaging systems.

2.4.4 Ultrashort pulsed vortices

The generation of hollow (doughnut) beams is of increasing interest for trapping and guiding atoms [Arl01], stimulated emission depletion (STED) microscopy [Hel94] and other applications. If a supplementary field singularity is involved (e.g., the central phase dislocation of a spiral phase plate), an orbital angular momentum appears. In certain applications, the additional degree of freedom is exploited to encode information or to transfer rotational energy to particles or cells in optical tweezers [Gri03]. Moreover, a flexible tailoring of pulsed vortex beams in spatial and temporal domain promises novel applications in filament control, particle acceleration, harmonics generation, plasma confinement, information processing, spintronics or time-resolved microscopy. As mentioned earlier, monochromatic doughnut modes of high contrast are obtained with spiral phase plates of azimuthally variable phase (0 to $2\pi\cdot\ell$, ℓ = integer order of angular momentum), diffractive optical elements, holograms, phased arrays (with reduced symmetry and parasitic oscillations) [Zho10], and photonic crystal fibers [Hu06]. At ever shorter pulse duration and increasing spectral bandwidth it becomes more relevant to preserve the temporal pulse structure. With regard to these requirements it is evident that with the approach of forked gratings difficulties emerge in terms of angular dispersion resulting in a spatial and temporal separation of the spectral components. However, the spatial separation is reversed in a 2f-2f setup with an additional nonforked grating or prism. The concept was first demonstrated by Bezuhanov et

al. by using photolithographically produced binary gratings and optical pulses of 20 fs pulse duration [Bez04]. In this setup, a nonforked grating was used to compensate the spatial dispersion of the second forked grating. Vortices of relatively low contrast and about 10 % efficiency were obtained in the first diffraction order of the CGH. The same setup was copied by another group to generate vortex pulses of measured 280 fs length [Mar05]. With CGHs programmed into a spatial light modulator, 80-fs Laguerre-Gaussian pulses were shaped from 6.4-fs pulses in a 4-f system with angular and group velocity dispersion compensation [Zey07]. Later, a modified version of the 2f-2f grating setup was applied by replacing the nonforked grating by a compensating prism pair and by removing the lenses. For the first time optical vortices of pulse durations of 17 fs were produced with the ability to handle also sub-10-fs pulses [Sch08]. With the approach based on polarization conversion and mode separation, the conversion of 120 fs Gaussian pulses into 150 fs vortices was demonstrated with high efficiency [Shv10]. Recently, Yamane et al. demonstrated the generation of 5.9-fs pulses (2.3 cycles) in an optical parametric amplification system by means of the aforementioned polarization technique [Yam12].

All these techniques to shape high-contrast ultrashort-pulsed hollow beams, however, require a laborious arrangement. To realize very compact and highly flexible shapers for pulsed vortex beams, the complex spatiotemporal performance of new active components at extremely short pulse durations has still to be studied. A promising approach can be found in diffractive optics, especially in circular and spiral diffraction gratings [Dys58, Mac93, Kor95]. Refractive and diffractive properties have a direct influence on the shape of the pulse in space and time. Thus, multiple features of pulse shaping can be combined in a single optical element. The optical properties of such spiral diffraction gratings play a particular role for a tailored manipulation of the spatiotemporal properties of localized wave packets. In this respect, it is, above all, the spatial overlap of each spectral component and a balanced positive and negative group delay dispersion, which deserve attention. In the literature it was shown before that with a so-called Lensacon and variable curvatures of the input wavefront (by adapting the angular magnification of the used telescope configuration) the necessary temporal dispersion is induced to suppress the temporal spread in a glassy bulk material [Son97]. This was the first experimental demonstration of Bessel-X pulses for a pulse duration about 210 fs. Very recently, the temporal focusing of ultrashort Bessel beams into Airy-Bessel light bullets was shown via a circular phase diffraction grating [Pik12].

To understand the basic physical behavior of spiral gratings it is necessary to know the grating period and the resulting deflection angle of the first diffraction order. With this principle, a

sufficiently accurate approximation of the real conditions is achieved. Based on the theoretical description of the angular dispersion as introduced in chapter 2.3.2, it is obvious that a circular or spiral grating enables the combination of a permanent recompression of dispersed ultrashort pulses with the nondiffracting behavior of Bessel beams, as shown in the example below.

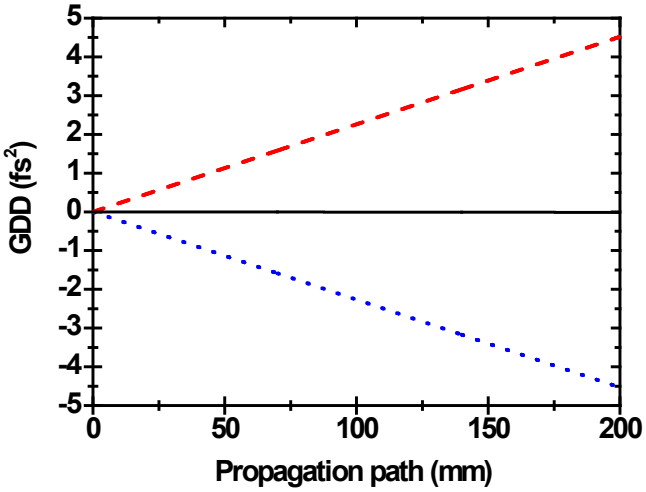

Fig. 2.3.8 GDD as a function of the optical beam path at a central wavelength of 800 nm: A permanent recompression of a nondiffracting beam is achieved by choosing a grating period of 200 µm. The red dashed line corresponds to the positive dispersion of air whereas the blue dotted line represents the additional negative GDD of the grating. The total amount is zero for all axial positions.

In the following calculations the DOE substrate thickness was neglected or the substrate-induced dispersion was precompensated by chirped mirrors, respectively. It was further assumed that the GDD of air is around +0.02 fs^2 at 800 nm and the grating period was set to be 200 µm. The grating equation (40) was used to obtain the dispersion relations. In *Fig. 2.3.8* the GDDs of air and grating are plotted in dependence on the optical beam path. In this case, both contributions balanced each other out perfectly and the total GDD (black line) is approximately constant over the entire range. This result illustrates the working principle of diffractive axicons and shows that nondispersive and nondiffracting pulses may be realized approximately as short as the input pulse. Thanks to this extraordinary spatiotemporal behavior, highly temporal localized wave packets of twisted or untwisted wavefronts are therefore now within reach, even though the experimental realization of such conditions is challenging. There are some difficulties that have to be faced. Apart from the supply of a pulsed laser source delivering single- or sub-cycle pulses, on the one hand side there is the substrate of non-negligible thickness adding a constant linear chirp to the spectral phase. A compensation is achieved either with chirped mirrors or a smaller grating period (higher spatial frequency). The latter one supports a significant drawback that it would increase the

GDD gradient in axial direction which can never be compensated by air dispersion (but of course at the plane of interest by material dispersion). On the other hand a grating period of 200 µm is relatively large and requires a sufficient number of illuminated grooves for a full grating effect, hence, the input beam diameter should be magnified. If the dispersion compensation has to be designed for minimum pulse duration within the substrate, the conditions are similar. The positive GDD of for example SiO_2 may easily be turned to zero for grating periods of about 5 µm. For practical applications, however, the focal range has to be located outside the material, but then the huge negative GDD is responsible for a rapid temporal broadening of the pulse. The specific design of the optical setup is here of determinative significance.

Orbital momentum beams or vortices occur as particular solutions of the wave equation like higher order Laguerre- or Bessel-Gaussian beams, which carry an ℓ times twisted phase front. Laguerre-Gaussian laser modes were the preferred modes of generation at the beginning of the research on OAM. These modes appear as rings with zero intensity in the center and are characterized by the spatial phase dependency (topological charge ℓ) as well as by the number of nodes in radially direction (number of rings). The best-known distribution is the TEM_{10^*} mode associated with a "doughnut" profile. In this frame it makes sense to distinguish between azimuthal Laguerre-Gaussian modes generated in cylindrical symmetric laser resonators and Laguerre-Gaussian beams converted from Gaussian mode (TEM_{00}) with the help of appropriate optics outside the cavity. Note that Laguerre or Bessel vortices behave very differently to small-core vortices according to the radial intensity distribution and propagation behavior.

The electric field distribution of a propagating single optical vortex centered at the origin may be expressed as:

$$E(r,\theta,z) = E_0 E_l(r,z)\exp(i\omega t)\exp\left[i\left(-kz + \ell\xi + \Phi_\ell(r,z) + \varphi_0\right)\right]. \qquad (52)$$

Written in cylindrical coordinates the representing variables are the optical angular frequency ω, the time t, the wave number k, the axial coordinate z, the topological charge ℓ, the azimuthal phase ξ and the additional constant phase φ_0. The real-valued constant E_0 describes the maximum field amplitude where otherwise the field envelope is given by E_ℓ which asymptotically vanishes for $r \to \infty$ and $r = 0$. The radially and axially dependent wavefront

curvature is determined by Φ_ℓ. The index ℓ gives further information about the wavefront and the envelope function. For ultrashort pulses the field changes to:

$$E(r,\theta,z) = E_0 E_l(r,z)\exp\left(-\frac{2\ln(2)t^2}{\tau_P{}^2}\right)\times \exp(i\omega_0 t+\varphi(t))\exp[i(-kz+\ell\xi+\Phi_\ell(r,z))] \quad . \tag{53}$$

It should be noted that this equation is only valid within the frame of a slowly varying envelope approximation (SVEA) where the pulse envelope in z-direction (or in time) is much longer than a cycle of the electric field:

$$\left|\partial_z E_0\right| << k_0\left|E_0\right| . \tag{54}$$

Any beam with a helical phase structure following a *exp(iℓξ)* dependence carries an orbital angular momentum and hence also higher order Bessel-Gaussian beams generated via spiral phase plates and axicons. The field amplitude of Bessel vortices is described as introduced in chapter 2.1 and 2.2 with the crucial difference to have inserted an additional phase function:

$$E(r,\xi,z) \propto \exp(ik_z z)\exp(i\ell\xi)J_\ell(k_r r) . \tag{55}$$

For the more interesting case of ultrashort pulses and the detection with a time integrating CCD-camera, the measured intensity is:

$$J_{PNB}(r)^2 = \int_{t_1}^{t_2}\mathrm{Re}\left\{\sqrt{Z}\cdot\exp\left[-\frac{\tau_a{}^2+t^2}{2\tau_0{}^2}\right]\cdot\exp\left[i\left(\frac{2\pi\cdot t\cdot c}{\lambda_0}+\ell\xi\right)\right]\cdot J_\ell(r)\right\}^2 dt . \tag{56}$$

The parameters are the same as in chapter 2.2 except that the Bessel function is more generally defined to cover also higher orders:

$$J_\ell(r) = \frac{1}{\pi}\int_0^\pi \cos\left[\frac{2\pi\cdot r\cdot c\cdot\sin(q)}{\lambda}-\ell q\right]\cdot dq . \tag{57}$$

These types of vortex beams (twisted localized waves) are a preferred object of interest in this thesis (see chapter 4.7) because of combining few cycles of the field with a distinct orbital angular momentum and a nondiffracting behavior. The spatial and temporal overlap of all spectral components plays an essential role to keep the contrast high and the pulse short. For that reason, diffractive spiral gratings seem to be the best choice of a tailored spatial and temporal beam shaping of ultrashort pulses for singular optics.

CHAPTER 3

3 Experimental techniques

3.1 Pulsed laser sources

In the experiments, two different Ti:sapphire laser oscillators served as light sources providing femtosecond pulses in the range of few-cycles of the electric field. For most of the experiments discussed below the shortest pulses available were used preferentially. Before experiments were performed, the laser beam parameters were measured carefully ensuring that the input parameters are close to the optimal values. However, a complete characterization is hard to realize because of a spatial dependency of spectrum, phase, pulse duration, polarization, etc.. Therefore, a set of relevant parameters was selected.

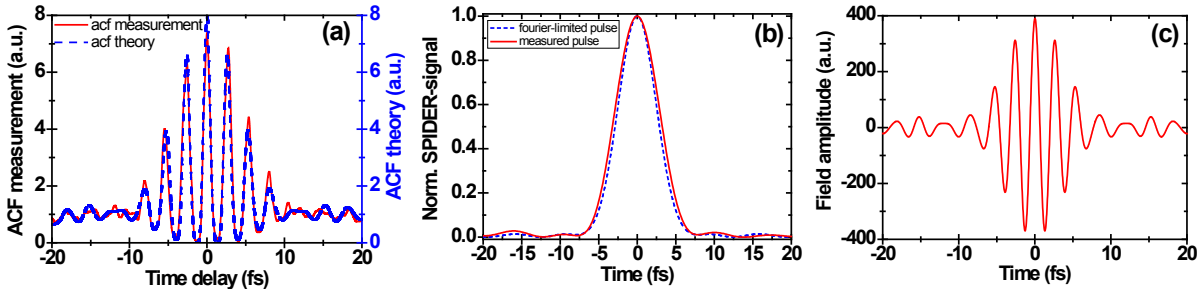

Fig. 3.1.1 Pulse characteristics of 'Laser B' (see *Tab. 3.1.1*): **(a)** Measured 2nd order autocorrelation (red solid line) and calculated autocorrelation from measured spectrum (blue dashed line), **(b)** Pulse shape and duration of 6.5 fs (red solid line) retrieved from SPIDER data. The Fourier-limited pulse is slightly shorter around 5.9 fs (blue dashed line), **(c)** Reconstructed electric field amplitude as a function of time.

The pulse duration was experimentally investigated both with the spectral phase interferometry for direct electric field reconstruction (SPIDER) method and second order

autocorrelation measurements (see chapter 3.3). Related results, in this case for 'Laser B', are plotted in *Fig. 3.1.1* including the retrieved electric field amplitude of the pulse. The graphs show a typical nearly Fourier-limited pulse at the output of the laser oscillator. The beam profiles and the spatially resolved spectral widths (standard deviation) of both lasers are found in *Figs. 3.1.2*. The measurement was performed by a spatially resolved spectral scan of the cross section of the laser beam at a distance of around 10 cm from the exit window of the laser oscillator. The spatial resolution (step width) was set to be 40 µm.

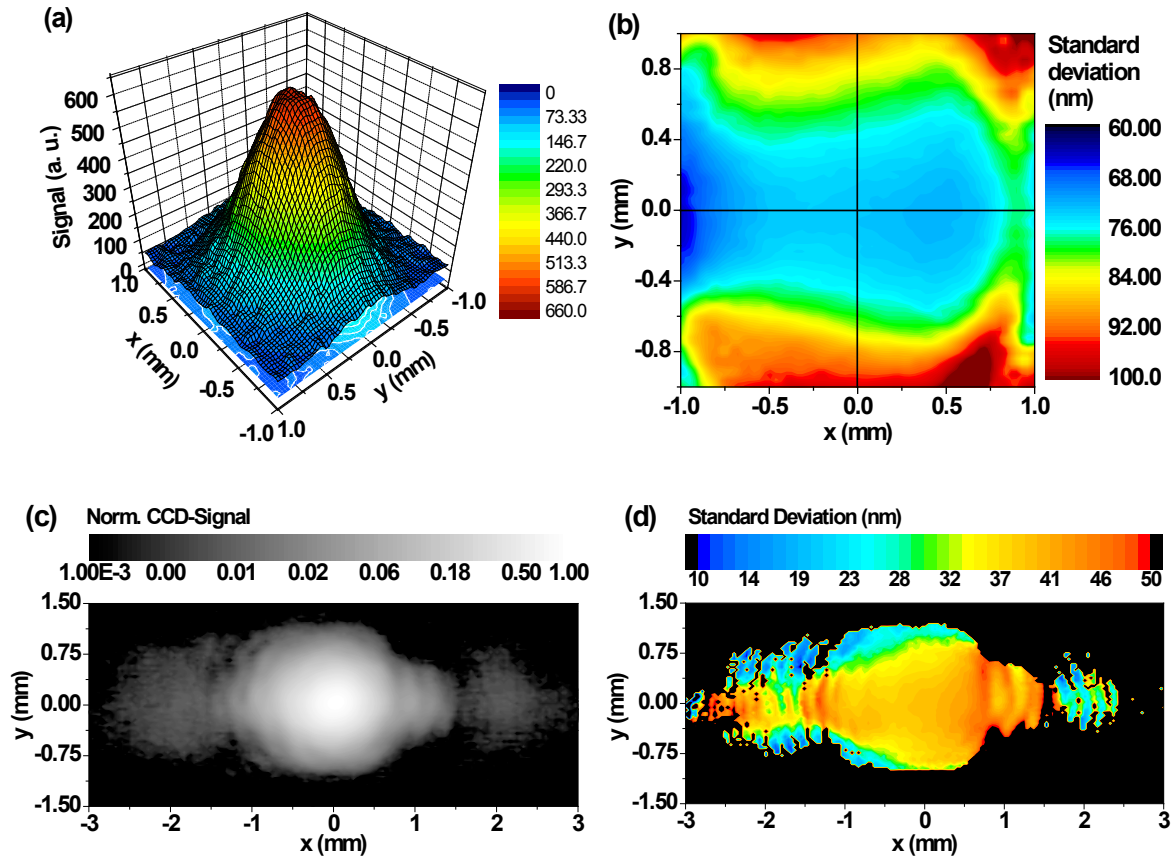

Fig. 3.1.2 Beam properties measured with a spatially resolving scanning fiber system: **(a)** 2D beam intensity profile of 'Laser B', **(b)** Spatial map of the spectral bandwidth (standard deviation) of 'Laser B'. The broad bandwidth in the upper and lower section of the beam is due to the significantly reduced signal-to-noise ratio, **(c)** beam intensity profile of 'Laser A' plotted in logarithmic scales, **(d)** Spatial map of the spectral bandwidth (standard deviation) of 'Laser A'.

Note that at lower intensities of the beam profile the shape of the spectrum changes. The spectra become more platykurtic or leptokurtic and thus the spectral width is increased or decreased. This effect implies a variation of the pulse duration with the spatial coordinate, however, the spectral phase has to be taken into account. The reason for the varying spectral width stems from the fact that in polychromatic Gaussian beams each spectral component has its own divergence and beam waist, forming spectral wavefronts with different radii of

curvatures [Por98, Car99, Fen00]. Furthermore, additional spectral-dependent phase and amplitude aberrations within the laser cavity are introduced by optical components such as gain medium (Kerr-lens, net gain), outcoupling mirror, etc.. This leads to a temporal separation of the spectral components and thus usually to a temporal broadening of the pulse in transversal direction. In chapter 4.5 it will be shown by the method of wavefront autocorrelation that the pulse duration shows indeed a spatial variation and that the shortest pulse is typically found at the beam center.

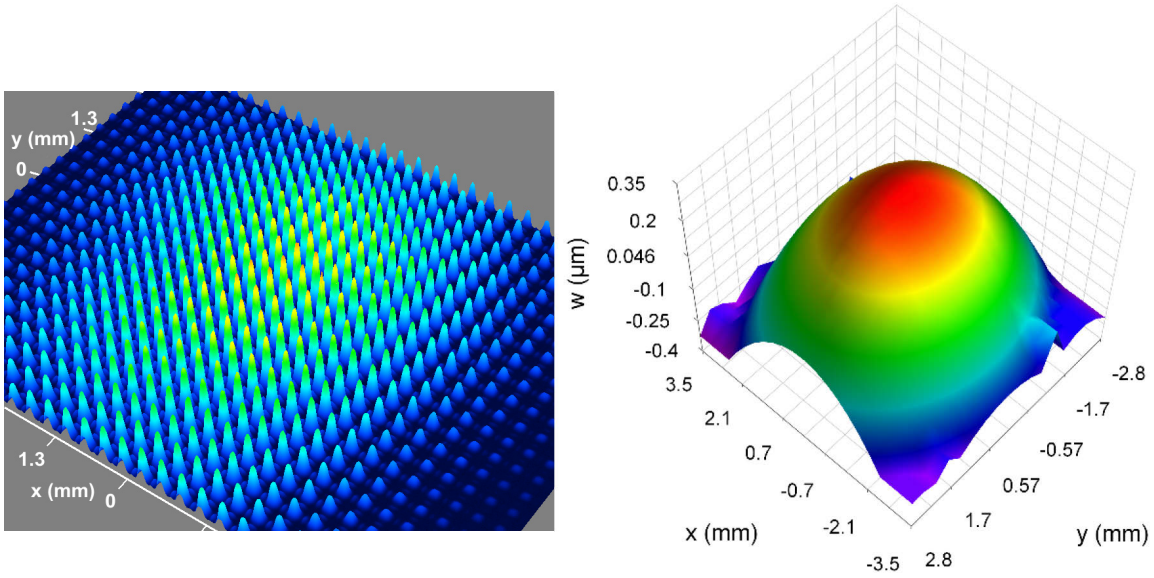

(a) **(b)**

Fig. 3.1.3 Wavefront characterization with a Shack-Hartmann sensor: **(a)** Spot arrays generated via microlenses illuminated by the laser beam, whose wavefront has to be measured. **(b)** Here, the retrieved wavefront is shown. As it is recognized, the wavefront is slightly elliptical.

The shortest pulses provide peak powers of 1.1 MW. Such powers are sufficient to measure a spatially resolved 2nd order autocorrelation with a high signal-to-noise ratio. This is very important for experiments in the next chapter with the goal of generating and measuring highly localized waves and complex combinations of them. However, the specific signal-to-noise ratio depends on the chosen nonlinear crystal, the numbers of sub-beams and the type of matrix detector.

In *Tab. 3.1.1* the main parameters of the laser systems are summarized. Using the example of 'Laser A' the beam divergence was measured using a commercial Shack-Hartmann wavefront sensor (Metrolux ML3743, spatial resolution 320 µm). The spot arrays in *Fig. 3.1.3(a)* provide information as to whether the actual wavefront (here of 'Laser A') elongates the spot positions with respect to a well-known reference. The retrieved wavefront of the cross section of the beam is illustrated in *Fig. 3.1.3(b)*. The laser produces an almost spherical wavefront.

Table 3.1.1 In this list the most important laser parameters of both Ti:sapphire laser oscillators used in the experiments (measured data) are shown.

Parameter	'Laser A' (FemtoSource Scientific Pro)	'Laser B' (Venteon Pulse One PE)
Pulse duration	12 fs	6.5 fs
Spectral bandwidth (FWHM)	90 nm	170 nm
Center wavelength	815 nm	815 nm
Modelocked output power	400 mW at 4.3 W (532 nm)	600 mW at 6.0 W (532 nm)
Pulse energy	5.3 nJ	7.5 nJ
Repetition rate	75 MHz	80 MHz
Beam diameter	2 mm	2 mm
Beam divergence (total)	< 2 mrad	< 2 mrad

The elongation data were recorded in the far-field at a distance of about 10 m from the beam waist of the pulsed laser. At this distance the expanded beam illuminates the complete microlens array, however, not all spots were taken into account for the analysis. The half-angle beam divergence θ is estimated by calculating the ratio of the beam radius w to the radius of curvature ρ:

$$\theta = \frac{w}{\rho}. \tag{58}$$

A beam radius of 5.5 mm and a radius of curvature of 9700 mm were measured for 'Laser A'. The uncertainty in measuring the beam radius and radius of curvature was about ± 0.1 mm and ± 100 mm, respectively. Therefore, the half-angle divergence is around 0.55 ± 0.03 mrad. A beam quality factor of M^2 = 1.2 ± 0.08 is derived, which was calculated from equations (8) and (19).

3.2 Pulse characterization methods

Characterizing ultrashort pulses is one of the key challenges in ultrafast optics. In best case, this comprises a complete description of the pulse properties (polarization, spectrum, phase, ampitude) delivering information on the Wigner function of the wave packet. A key issue is the measurement of the pulse duration. For relatively long pulses, that means pulses in the range of pico- to nanosecond time duration, the recording of the pulse versus time is realized electronically by fast photo diodes and if necessary in combination with streaking techniques. For pulses in the femtosecond range down to few cycles of the electric field one needs other methods to determine the temporal properties. It should be generally noted that for the measurement of the temporal information of a pulse a time-non-stationary filter (optical gating) is required, as it is achievable with a nonlinear crystal. A frequently applied method to determine the duration of few-cycle pulses is the measurement of the fringe-resolved 2^{nd} order autocorrelation (SHG-FRAC). Then, the autocorrelation trace allows to retrieve the pulse duration appropriately [Sor00]. For this purpose, the original pulse is split into two replicas. These two pulses are temporally superimposed collinearly in a nonlinear crystal like LBO, BBO or KDP. One of the pulse replicas is temporally delayed (by lengthening one arm of the interferometer) and the second harmonic light is recorded by a single photo diode or a matrix detector for each delay position. The resulting FRAC-trace is shown in *Fig. 3.1.1(a)*. In fact, without focusing the fundamental light into the nonlinear crystal, a matrix detector is able to perform a spatially resolved autocorrelation measurement. On the other side, the FRAC has some drawbacks. Firstly, for octave spanning spectra it is difficult to separate the fundamental spectrum from the converted one. Secondly, to calculate the pulse duration an assumption of the temporal pulse shape has to be made. Usually, in the experimental analysis a sech^2-shaped pulse is assumed. Nevertheless, a FRAC-trace contains more information than the pulse duration. Capable methods and algorithms were developed to extract the order of the chirp and, moreover, in combination with the first order interferogram such extended schemes allow to retrieve the spectral phase in many cases [Ben08].

A considerable improvement in the performance of the autocorrelation technique, however, is obtained by extending the measuring scheme by applying a spectrally resolved recording of the SHG-signal. The two-dimensional (wavelength vs. delay) parameter space is used to iteratively retrieve the spectral phase and thus the temporal shape of the pulse. This indirect method is known as frequency-resolved optical gating (FROG) [Tre02]. The kind of the FROG-trace depends on the specific type of gating which has different strengths and

weaknesses. The most important methods are polarization-gated (PG) FROG, self-diffraction (SD) FROG, transient-grating (TG) FROG, third-harmonic (THG) FROG, interferometric (I) FROG, cross-correlation (X) FROG [Del94].

Another method to retrieve the temporal shape of the pulse is the spectral phase interferometry for direct electric field reconstruction (SPIDER) [Iac98]. This concept is based on spectral shearing interferometry where the material dispersion is measured by analyzing the spectral interference pattern (increasing or decreasing fringe frequency). In the SPIDER scheme, first of all, the input pulse is split into two replicas. In a second step, one of the pulses is again replicated whereas the other one is temporally stretched into the picosecond range by transmitting the pulse through an optical material with a positive group velocity dispersion. Within the stretched pulse the optical frequency increases with time (up-chirped pulse). Both, the double pulse and the stretched pulse are focused into a nonlinear crystal to obtain two sheared pulses. The interaction geometry is noncollinear. The up-converted short pulses differ slightly with respect to the center frequencies. The SPIDER spectrogram of these pulses contains the necessary information (derivation of the spectral phase) to calculate the spectral phase of the pulse. There exist also modified SPIDER-setups like the down-conversion (DC), zero additional phase (ZAP), homodyne optical technique (HOT) and long crystal (LX) SPIDER [And08], to mention a few.

Spatially resolved autocorrelation

A spatially resolved measurement of the temporal properties of ultrashort pulses is of growing interest in modern physical research. It allows a detailed evaluation of the laser or setup conditions and enables an optimal performance. For instance, a linear increase of the pulse duration over the beam cross section can then directly be detected and eliminated or used for later analysis (correction). Commercially available SPIDER setups are not designed to cover a spatial resolution of the phase and amplitude of the pulses. Collimated beams like Gaussian or solitary needle beams are a basic precondition to run such a system accurately. Only then a tight focus (concave mirror) of the three pulses within the nonlinear crystal and a good signal-to-noise ratio is achieved. A spatially resolved measurement of the pulse, however, requires a modified SPIDER setup, including very sensitive detectors. An implementation of a spatially resolved FROG setup is of similar complexity. Nevertheless, methods exists, some based on SPIDER, FROG or STARFISH [Gal01, Akt03, Bow07, Alo10]. However, in the experiments for evaluating the spatiotemporal structure of laser pulses and HLWs the SHG-autocorrelation

was used exclusively. The advantages of a fringe resolved second order autocorrelation measurement with needle beams as an excellent tool for temporal mapping is discussed in the following and experimentally verified in chapter 4.5.

For a two-dimensional spatially resolved nonlinear autocorrelation the beneficial properties of Bessel beam arrays are exploited. This was demonstrated for the first time by Grunwald et al. by using thin-film micro-optical axicon arrays to perform a combined spatially resolved collinear autocorrelation and Shack–Hartmann wavefront sensing [Gru03]. However, Bessel beams characterized by ring patterns show a rather poor degree of spatial localization. Hence, it is highly desirable to have sub-beams in the array exhibiting a maximum localization in space and time. Needle beams and their exclusive properties appear to be the very best choice to achieve a robust measurement with well-separated beams. For that purpose, ultraflat axicons arranged in a matrix are programmed into LCoS-SLMs. This yields a flexible control of the needle beam parameters according to the measuring conditions. Apart from the advantage of a spatially non-integrating method, inaccuracies induced by spatial and chromatic aberrations of focusing optics (conventional lenses or mirrors) are a priori excluded because of very small conical angles, quasi aperture-less axicons (reduced diffraction effects) and an illumination of the sub-axicons with nearly flat wavefronts. The autocorrelation setup is highly robust against off-axis illumination, however, for a large oblique incidence >30° additional aberration corrections have to be implemented [Gru07]. Furthermore, the setup enables an accurate measurement of the pulse duration at low input intensities (oscillator pulses). The recording of autocorrelation traces via an EMCCD detector enables even measurements at single photon level, however, the Michelson interferometer (see *Fig. 3.3.4*) must be sufficiently stable with respect to temporal drifts.

The intensity distribution is detected in the plane of interest. At this plane, a nonlinear crystal with a high second order nonlinear coefficient is used, for instance, a high quality Beta-Barium-Borate (BBO) crystal of 10 µm thickness. The low thickness ensures an effective phase matching over a broad spectral range and thus a nearly undistorted retrieval of the pulse duration. Usually the step size of the delay arm is equal to 20 nm which corresponds to a sampling time of < 133 attoseconds. This is considerably more than the involved averaged jitter of around 50 as caused by interferometer and laser instabilities. It is expected that relative measurements may reach the sub-10 as range in time-resolution.

3.3 Liquid-crystal-on-silicon spatial light modulator

Liquid crystal (LC) based spatial light modulators (SLMs) were originally designed for high quality image projection systems and dynamic diffractive optical elements (DOEs). Such devices allow a purely electronic programming (i.e., without moving mechanical elements as in the case of MEMS). With the commercial availability of a new generation of high-resolution reflective phase-only liquid-crystal-on-silicon SLMs (LCoS-SLMs in *Fig. 3.3.1(a)*), components of significantly reduced dispersion became available. Their ease of use, high native resolution, moderate damage thresholds and phase strokes of up to 2π are further important advantages.

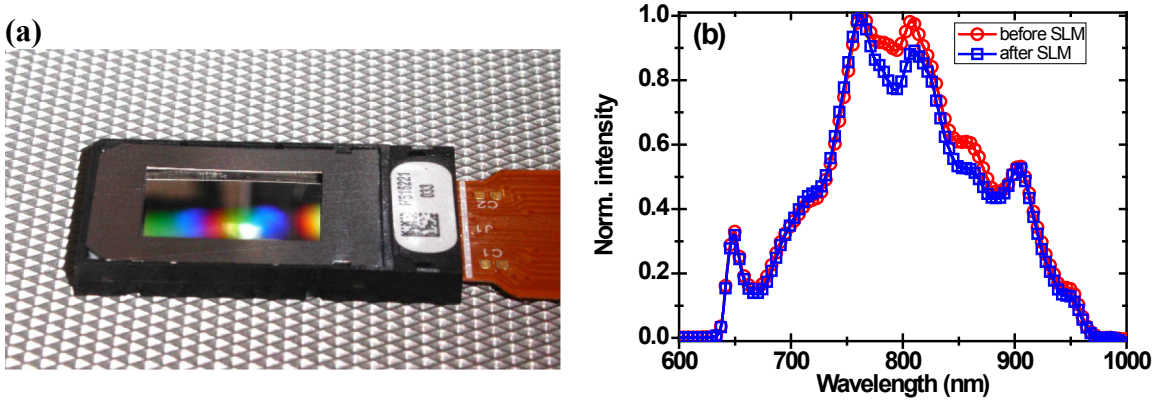

Fig. 3.3.1 LCoS-SLM and spectral transfer **(a)** View on the device with dimensions of 17 x 11mm in a protective housing, **(b)** Typical transferred spectrum (blue open squares) of an LCoS-SLM in comparison to the input spectrum (red open circles). Here, the light source was a Ti:sapphire laser oscillator from Venteon ('Laser B').

For applications in femtosecond range, in particular at pulse durations related to only a few cycles of the optical field, a careful optimization of all parameters is necessary and requires a deeper understanding of the relevant physical processes. For high-bandwidth few-cycle pulses, the spatial shaping is complex because of the spectral bandwidth and additional effects caused by high peak intensity and travel time differences. Therefore, one has to characterize LCoS-SLMs with respect to the temporal and spectral distortions (e.g. dispersion and/or diffraction caused by the pixels) of the ultrashort input pulse. A systematic investigation of the characteristics of LCoS-displays under such extreme conditions was reported in reference [Boc08a]. The spectral transfer characteristics is shown in *Fig. 3.3.1(b)*. There are no significant changes in the spectrum visible (nearly constant bandwidth). This property of the modulator ensures that Fourier-limited pulses of durations down to 4 femtoseconds (1.5 cycles of the electric field) can be applied. The efficiency (pure reflection) is limited to 55 % due to the pixelated structure of the display.

Obviously, it is of great interest to measure the phase delay as a function of the programmed gray level (corresponding to a certain voltage) as well as of the wavelength. For this reason, the phase shift was measured by spectrally resolved spatial interferometry. Here, the SLM was divided into a reference and signal branch illuminated by a reference and probe beam. The two beams were generated by a double pinhole placed close to the SLM. At a certain distance both beams overlap (due to diffraction) and create a spatial interference pattern. The detector was a scanning (one-dimensional) fiber-based spectrometer having a spatial resolution of 15 µm placed in the far field. The gray level of the probing display part was varied from 0 to 255 (8 bit) whereas the gray level of the reference part remain at 0. The resulting spatial displacement of the intensity maxima of the interference pattern is a direct measure of the applied relative phase between the two half-screens. From these data the spectral-dependent optical retardance is retrieved as shown in *Fig. 3.3.2(a)* .

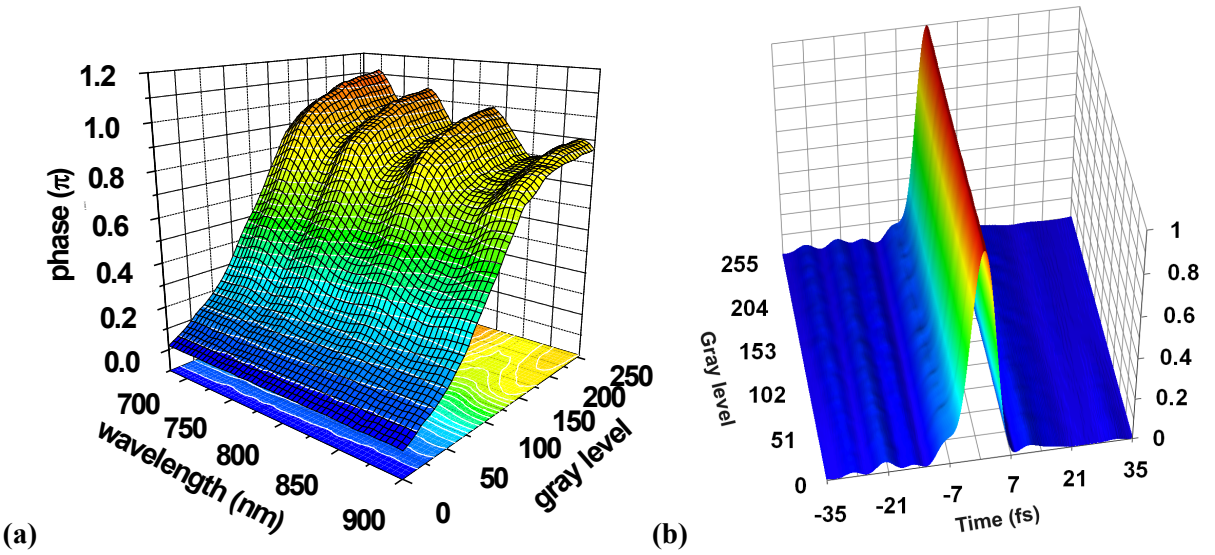

Fig. 3.3.2 Spectral and temporal properties of LCoS-displays: **(a)** Typical spectral-dependent phase delay as a function of the wavelength and gray level (Brillian SLM LCR-1080), **(b)** Typical pulse shape transfer in dependence on the programmed gray level (HoloEye Pluto-NIR2).

Here, a particular gray level corresponds to a certain voltage applied between the electrodes of the displays manifesting in a rotation of the liquid crystal. In the case of initially parallel aligned liquid crystals to the display surface an applied voltage turns the liquid crystals to a vertical position. For vertically aligned liquid crystal displays it is vice versa. The most commonly used liquid crystals are of uniaxial type, whose inhomogeneous refractive index is described by an orthogonal and parallel refractive index with respect to the molecule long axis. The rotation of the liquid crystal is achieved by an applied electric field. It tunes the effective refractive index of the material. The amount of phase retardation is determined by the input polarization. The maximum is reached when the input polarization is oriented along

the molecules' long axis. For uncalibrated displays the response of the phase retardation to the applied voltage is usually nonlinear. However, by knowing the exact response for each gray level a calibration can be implemented.

In close connection to these measurements it was found that the spectral phase exhibits slight oscillations. An independent validation of this behavior was found by the SPIDER method. A qualitative analysis of the layer structure revealed that the oscillations are originated in the existence of an asymmetric Fabry-Perót-Resonator known as Gires-Tournois-Interferometer (GTI) [Gir64, Apt06]. Hence, a pulse passing the LCoS-SLM experiences a certain but small temporal distortion by the formation of a low-contrast pulse train. In *Fig 3.3.2(b)*, the temporal evolution is shown as a function of the gray level retrieved form the data set. Here, the main pulse has a distinctly higher intensity in comparison to the pre- and post-pulses. In general, it was found that LCoS-SLMs have excellent spectro-temporal transfer properties to spatially shape extremely short pulses without significant distortions.

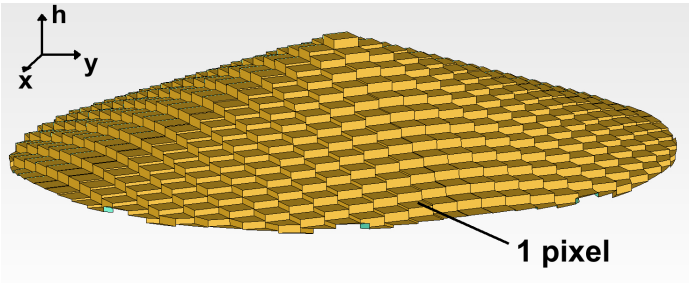

Fig. 3.3.3 Discretization of a conical axicon due to the discrete number of pixels and phase steps provided by a spatial light modulator. The size of the square pixels varies with the particular SLM design. A certain applied phase retardance is related to a certain height of a corresponding axicon mirror.

The axicon shape is generally approximated by programming a staircase-like phase structure into an LCoS-SLM. The phase resolution depends on the number of gray levels and the maximum phase value at the wavelength of interest. For a maximum phase shift of π or 2π at a center wavelength of 800 nm in 255 possible steps, the corresponding phase resolutions are 1.57 nm or 3.13 nm, respectively, as schematically illustrated in *Fig. 3.3.3*. The tolerable lower limit of the number of steps can only be discussed in the frame of rigorous diffraction theory (taking into account the ratio of a phase step to the transversal spatial period and wavelength). As a rule of thumb, however, one can apply the sampling theorem as known from signal theory. This consideration would deliver a minimum number of about 5 sampling points (phase steps) for a complete period of a periodically oscillating phase distribution. Microaxicons programmed in a liquid crystal layer provide a performance similar to those fabricated by using photolithography but with the advantage of high functionality.

Tab. 3.3.1 Properties of the liquid-crystal-on-silicon spatial light modulators (LCoS-SLM)

LCoS-SLM	Spatial resolution (Pixel)	Pixel size (µm)	Pixel pitch (µm)	Max. phase modulation (π)	LC-layer thickness (µm)	LC-layer alignment (µm)
SLM A	1920 x 1200	8.1	8.3	1.0 (@800 nm)	3	vertical
SLM B	1920 x 1080	8.0	8.2	2.7 (@800 nm)	4	parallel

In the experiments (see chapter 4), two different types of LCoS-SLMs of similar parameters but with different initial alignments of the liquid crystals come into play. The most important properties of both micro displays are summarized in *Tab. 3.3.1*. A linearization of the phase response with respect to the applied voltage was only performed for SLM B due to the huge initial maximum phase retardance. After calibration, the maximum phase modulation was significantly reduced down to 2π. The value is, however, still sufficiently high to realize highly localized wave packets (see self-apodizing condition). Generally, the experimental setup for the generation and spatiotemporal characterization is straightforward and held rather simple as shown in *Fig. 3.3.4*, excluding certain preliminary spatial shaping and dispersion compensation elements before striking the SLM. The temporal delay, which is necessary for measuring autocorrelation traces, is realized by a spectrally broadband, dispersion-balanced beam splitter in a Michelson interferometer arrangement. After passing the SLM, the HLWs are either detected in the fundamental frequency range (around the central wavelength λ_0 = 800 nm) by simultaneously obstructing one arm of the interferometer or in the second order frequency range (around the central wavelength λ_0 = 400 nm) by simultaneously displacing one of the interferometer mirrors to record the temporal structure.

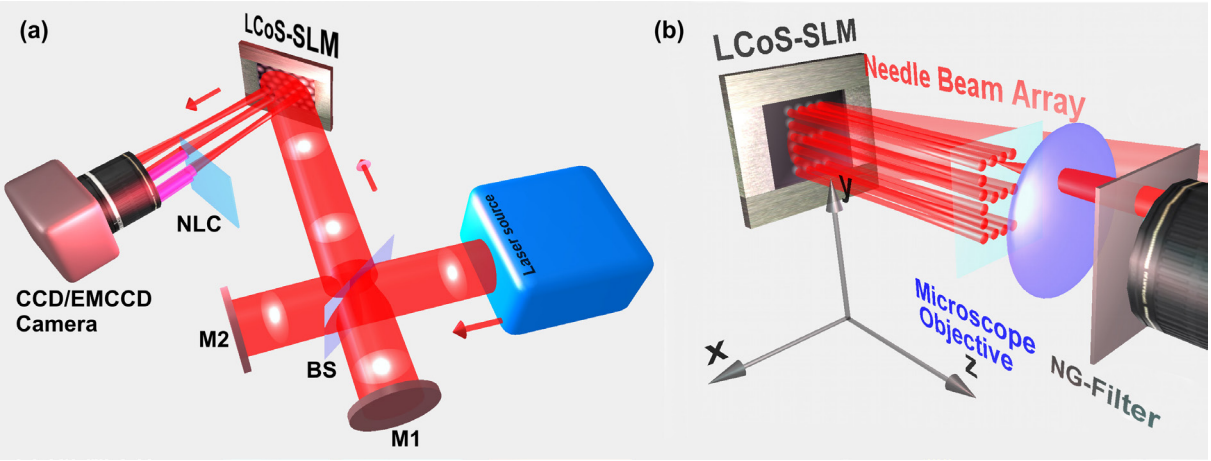

Fig. 3.3.4 Setups for the generation of HLWs with an LCoS-SLM: **(a)** Three-dimensional (x-, y-, z-direction) spatially resolved characterization with linear (direct detection of the fundamental light) and nonlinear (frequency up-converted light indicated by partially inserted NLC) methods, **(b)** a detail view on a modified setup characterizing complex light structures (e.g. a letter 'E'). The abbreviations are the following: M – mirror, BS – beam splitter, LCoS-SLM – liquid-crystal-on-silicon spatial light modulator, NLC – nonlinear crystal and (EM)CCD – (electron multiplying) charge coupled device.

3.4 Extended type of Shack-Hartmann sensor

Several concepts of reconfigurable Shack-Hartmann sensors (SHS) have been reported in the literature [Oli00] but only a few studies are dealing with liquid-crystal-based SLMs to rigorously generate reconfigurable arrays of sub-beams for wavefront detection. For that purpose, Fresnel-type microlens arrays were programmed into an SLM [Sei03, Rha04, Zha06]. The microlenses were designed to approximate multilevel micro-reliefs by appropriate sampling methods due to the pixelated structure of the device. The minimum number of pixels for the first Fresnel zone was specified to comprise at least 8 pixels, with the aim of a high-quality intensity distribution of the spots at a certain distance. Therefore, the focal length was also restricted to a minimum value in dependence on the pixel size and illuminating wavelength. Here, the minimum achieved focal length was about 30 mm. It was found that the intensity distribution of the light beams was disturbed by cross-talk and diffraction effects in dependence on the resolution of the SLM and the specific design of the diffractive optical elements (DOEs). For ultrashort pulses specific limitations arise according to the spatiotemporal and spectral transfer behavior of such DOEs.

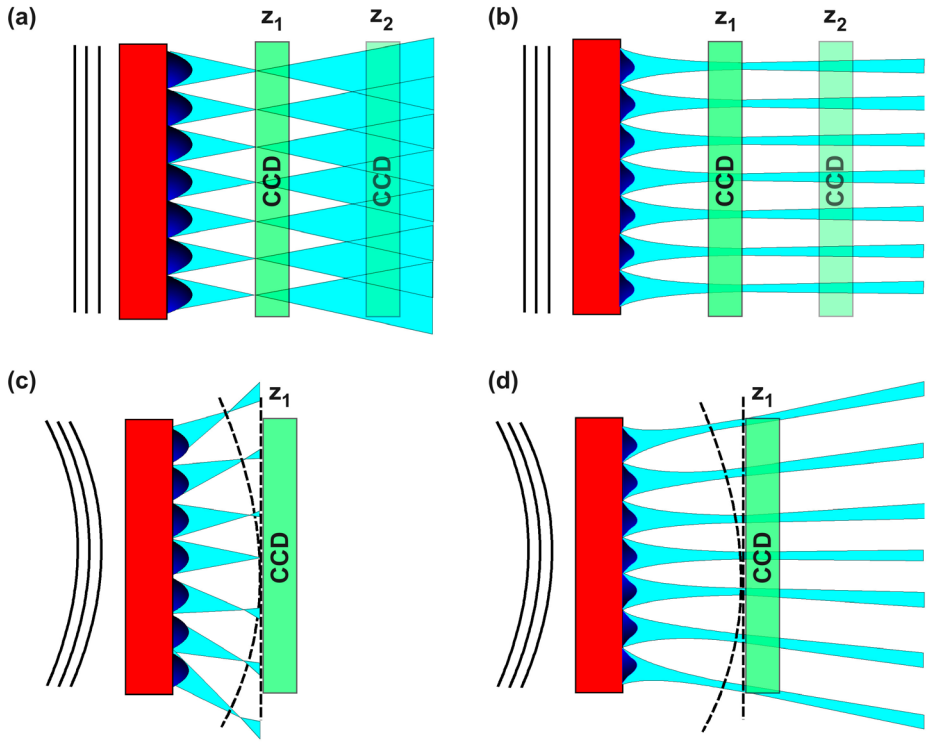

Fig. 3.4.1 Wavefront sensing according to the Shack-Hartmann principle: **(a)** Illumination of microlenses with a plane wave. The axial position of the detector is linked to the short focal length of the Gaussian-like beams. **(b)** Under the same conditions needle beams are much more tolerable with respect to the axial positioning. **(c)** The sub-beams generated by microlenses show an increased beam diameter and spot distortions when a strongly curved wavefront has to be detected. **(d)** This is almost completely suppressed if needle beams are implemented.

Generally, readout noise, dark current noise, photon noise, fixed pattern noise, background level, sampling error or an asymmetrically aberrated spot with side lobes are disadvantageous for the accuracy of Shack-Hartmann sensing and appear as centroid errors during analysis.
With respect to these influences it is absolutely essential that the spot deformations, cross-talk and diffraction effects are suppressed down to a minimum level to achieve a high spatial localization for an accurate retrieval of the spot position. Simultaneously, ultrashort pulses should keep as short as possible. A conservation of the pulse properties has the further advantage that it allows a simultaneous determination of the wavefront and a map of pulse duration (2^{nd} order autocorrelation) across the beam. It is therefore reasonable that needle beams are predestined to realize a robust and flexible Shack-Hartmann sensor for ultrashort pulses, achieving a high sensitivity (minimum detectable wavefront slope) at minimal analysis errors. Because needle beams show a high robustness against distortions and tilt-induced aberrations [Gru07], the center of gravity algorithm is more precisely, resulting in a higher centroid accuracy.

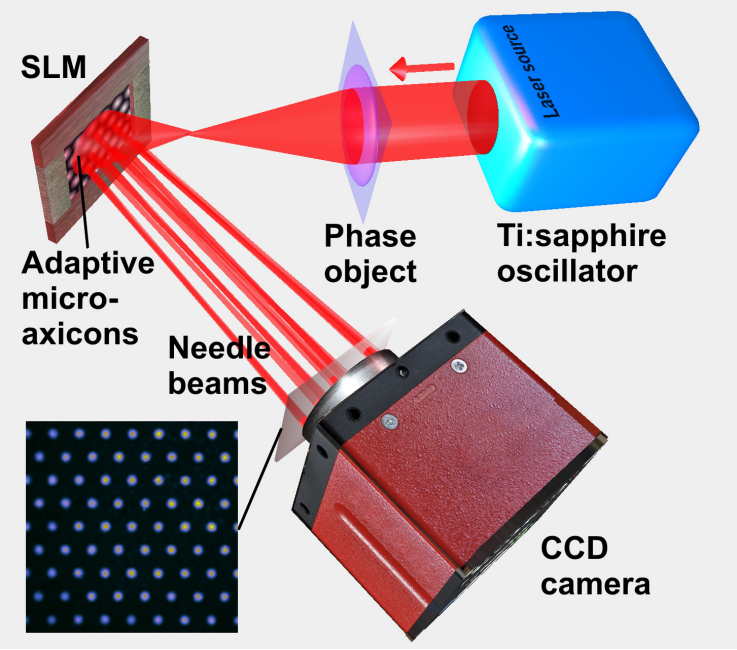

Fig. 3.4.2 Experimental setup for detecting arbitrary wavefront curvatures of ultrashort laser pulses by a reflective modified Shack-Hartmann sensor using hexagonal needle beam arrays (inset) for the wavefront analysis.

The major difference to established Shack-Hartmann sensors is that the setup is not critically dependent on a defined focal distance between microelements and matrix detector as required by a short depth of focus. This makes the setup relatively insensitive to a misalignment as long as the detector is placed somewhere within the non-diffracting zone. The distinct

advantages are schematically shown in *Fig. 3.4.1* by comparing positioning errors and spot distortion of Shack-Hartmann setups based on microlenses and microaxicons, respectively. A scheme of the needle-beam-based SHS is shown in *Fig. 3.4.2*. The experimental setup is similar to conventional arrangements. However, nondiffracting needle beams are used as sub-apertures and a reflective spatial light modulator is applied as a reconfigurable device. A detail description of the operating principle was given in the theory part (chapter 2.3.3) of this thesis. Note that for very high angles of incidence the shape of the axicons has to be adapted appropriately.

Using an LCoS-SLM with a high spatial resolution according to a pixel size of 8 µm and considering the aforementioned requirement of a minimum number of involved pixels, a non-diffracting zone of a length between $z \approx 0$ mm and $z \approx 2.5$ mm is expected for needle beams with a diameter ($1/e^2$) of 30 µm. The programming of axicon arrays with periods less than 200 µm (fill factor ~100%) allows a wavefront sensing with a high spatial resolution, much higher than in previous experimental setups reported in the literature so far. The beam width is larger in comparison to conventional sub-beams obtained by microlenses, however, it allows a binning of pixels to increase the signal-to-noise ratio (SNR). It should be noted that the retrieval error of the spot position is inversely proportional to the SNR value. A nonlinear image processing (frequency up-conversion) can be considered as well to further reduce the analyzing uncertainty of the spot position. The background noise is reduced and the beam width is narrowed.

CHAPTER 4

4 Experimental results

4.1 Programmable ultrashort-pulsed needle beams and flying images

The implementation of needle beams is realized by microoptical approaches of shaping Bessel-like sub-beams with finite, but extended nondiffracting zone under self-apodizing conditions. This concept becomes further attractive when combining it with the flexibility of programmable spatial light modulators for a high-accuracy phase control at ultrasmall conical angles and a defined background texturing. Here, a high-fidelity pulse transfer as required for a spatial shaping of few-femtosecond laser pulses is obtained with the LCoS-displays. This sub-chapter is concerned with the generation of radial symmetric HLWs possessing with a centered maximum (needle beams). With such micro-displays not only solitary needle beams of very extended focal zones but also arrays with dimensions in the micrometer range are shaped. *Fig. 4.1.1(a)* schematically shows interfering conical waves generated by arrays of axicons.

A detailed investigation of the propagation behavior of pulsed needle beam arrays is highly relevant with regards to the aforementioned applications. Thus, the experimental analysis addresses to the following aspects:

- Axial and radial intensity distribution (axicon, fraxicon)
- Correction of aberrations
- Spatial Talbot effect
- Spatially resolved pulse duration

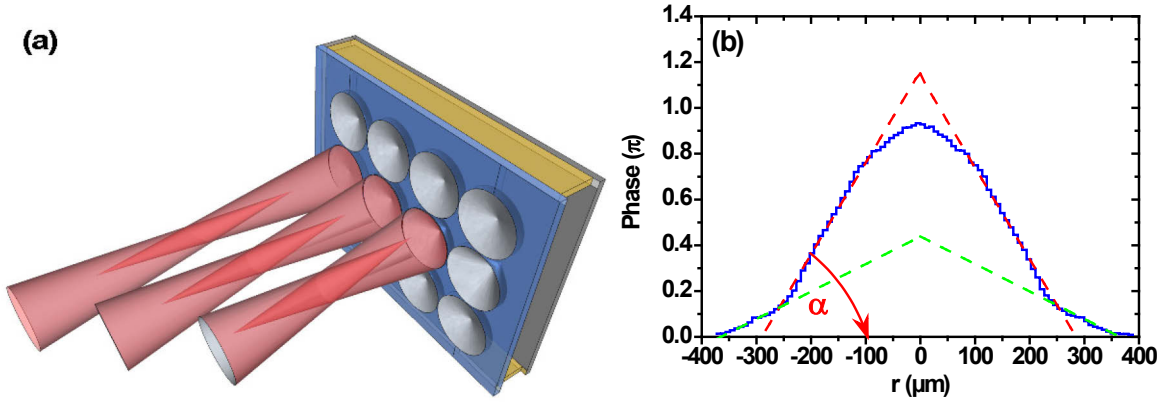

Fig. 4.1.1 Generation of polychromatic needle beams: **(a)** Scheme of typical micro-optical arrays for the generation of a matrix of needle beams via ultraflat axicons, **(b)** basic axicon profile for the generation of pulsed needle beams. To suppress diffraction effects on sharp edges, the chosen profile contains more than a single cone angle (indicated by the red and green dashed cones).

4.1.1 Needle beam twins

The basic phase profiles of the axicons (see *Fig. 4.1.1(b)*) were chosen to be the same for all experimental configurations. An optimized profile function is simply scaled down to achieve needle beams with beam radii in the sub-100 µm range. The basic axicon is designed to contain more than a single cone angle to suppress diffraction effects on sharp apertures. The axicon angle becomes increasingly smaller towards the center and the outer parts to achieve a "smoothed" apodization. The nondiffracting zone (constant intensity and beam radius) is then shorter than one could expect from the complete axicon radius. In the following, only the main axicon (red profile in *Fig. 4.1.1(b)*) angle θ will be specified. Additional modifications of the phase distribution will be evaluated separately.

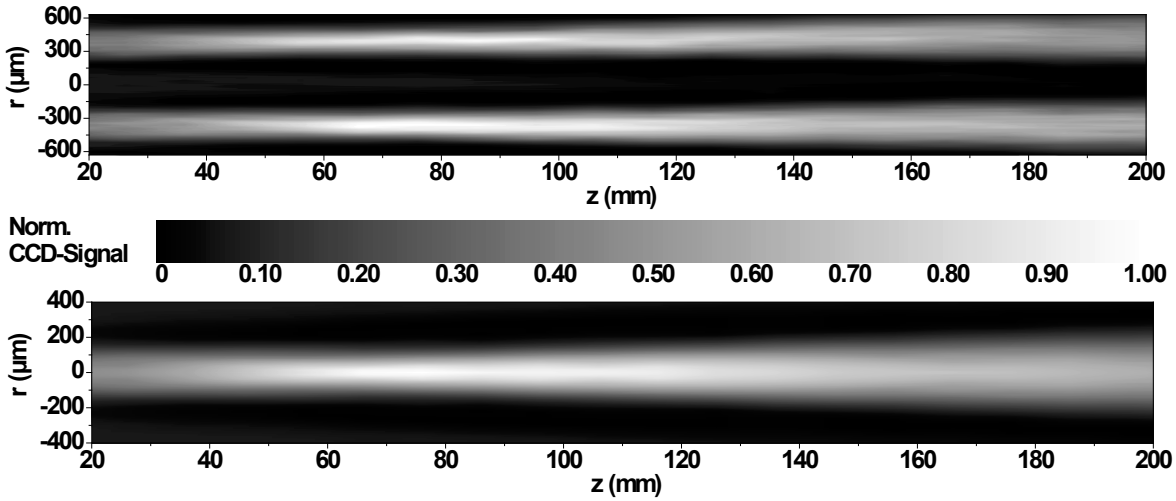

Fig. 4.1.2 Experimentally generated pulsed needle beams. The figure on top shows needle beam twins (without noise reduction). Both partial beams remain separated over an extremely long distance. To improve the analysis with respect to the propagation behavior, the intensity profile (bottom figure) was smoothed by averaging over >300 radial cuts with an incrementally increased cut angle.

A pair of axicons each of 760 µm in diameter was programmed into the SLM and illuminated by ultrashort laser pulses from 'Laser A' to analyze the typical axial and radial intensity profiles of polychromatic needle beams and cross-talk effects in arrays. The main conical angle was θ = 3 mrad. According to the introduced axicon shape, the nondiffracting zone should then theoretically arise between z = 25 mm and 90 mm. The measured axial intensity cuts of the double needle beams are shown in *Fig. 4.1.2(a)* and confirm the prediction in good approximation. To perform a better statistical analysis, the data of one of the needle beams were azimuthally averaged. The resulting intensity distribution and beam parameters as a function of axial distance are evaluated in *Fig. 4.1.2(b)* and *Fig. 4.1.3*. For comparison purposes, the theoretical beam parameters of an ideal monochromatic Gaussian beam are also included. It is noticeable that the needle beams propagate less nondiffracting. A range of the nondiffracting zone (almost constant intensity and beam radius) cannot be defined clearly because of the used axicon profile. Nevertheless, the Rayleigh length is defined by the distance from the beam waist to an $\sqrt{2}$-times expanded beam radius in accordance to the definition of a Gaussian beam. At this distance the intensity is halved. This Rayleigh criterion is used as a rough estimation of the length of the nondiffracting zone. However, a discrepancy appears (see a detailed discussion at the end of the chapter) in the retrieval of the range on the basis of expanding radius and decaying intensity yielding values of z_0 = 110 mm and 150 mm, respectively.

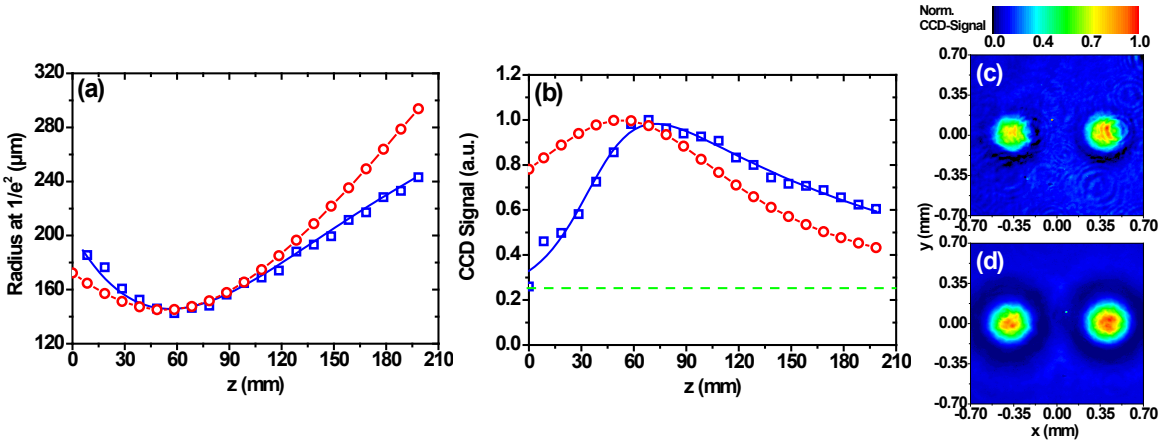

Fig. 4.1.3 Propagation parameters of one of the needle beams shown in Fig. 4.1.2: **(a)** Beam radius as a function of the distance in comparison to an ideal monochromatic Gaussian beam of comparable initial beam waist, **(b)** center beam intensity of a needle beam and Gaussian beam as a function of the axial coordinate normalized to the maximum CCD-signal. The green line indicates the initial intensity of the needle beam, **(c)** and **(d)** are the measured and normalized intensity cross sections of the twin needle beam at distances of z_1 = 18.5 mm and z_2 = 138.5 mm, respectively.

The cross-talk between neighboring sub-beams within arrays is reduced to a minimum level according to *Fig. 4.1.3(c,d)*. The two beams propagate over 200 mm with negligible cross-talking or blending effects. However, a very weak diffraction ring is visible at a distance of

z = 138.5 mm and becomes more pronounced with increasing distance. Thereby, the intensities of the needle beams and the diffraction ring become more and more equal.

A comparison between needle beams generated via axicons of different dimensions reveals that the expansion of the nondiffracting zone increases with the increasing axicon radius as expected from theory. The needle beams as shown in *Fig. 4.1.2* and *Fig. 4.1.5* were obtained for axicon radii R = 380 µm ('axicon A') and R = 100 µm ('axicon B'), respectively. The relative ratio of the nondiffracting zone to the beam waist radius is different for both beams. For 'axicon A' the aspect ratio of the resulting needle beams is 130 mm / 145 µm = 890 whereas for 'axicon B' the ratio is only 5 mm / 29 µm = 170. This fact is due to the quadratic dependence of the maximum extension of the nondiffracting zone on the axicon radius (see the self-apodizing condition).

4.1.2 Needle beams of extended depth of focus

Several strategies are examined to overcome the limitations by the maximum programmable phase difference of π and to achieve a large zone of nondiffracting properties. A first approach to reach higher values was to either use (1) a multiple reflection on the same SLM in a zig-zag path with an additional mirror, or (2) to arrange two separate SLMs of the same type in series. Another, alternative approach is (3) the zone axicon which was (referring to the Fresnel zone lens) called "fraxicon" and first proposed in [Gol06]. In this case, the depth of field is enhanced by stringing together a number of focal zones produced by discrete annular zones of a different (or the same) conical angle.

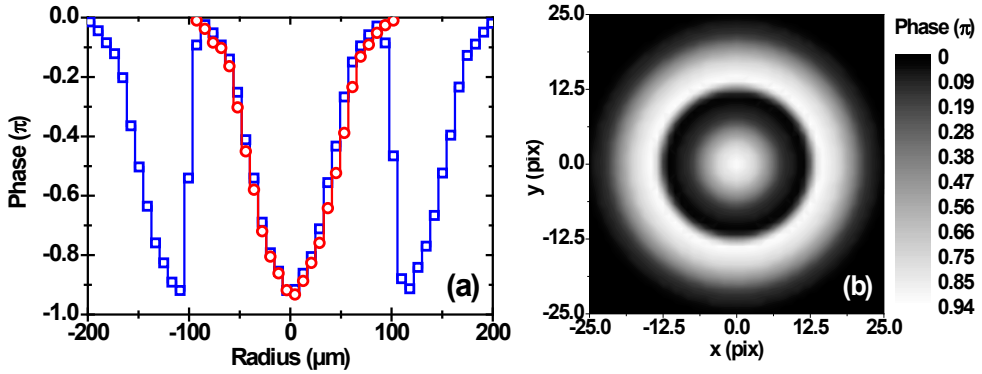

Fig. 4.1.4 Phase profiles of an axicon and a fraxicon: **(a)** Radial cuts of a wrapped (blue squares) and unwrapped axicon (red circles), **(b)** 2D phase distribution in the case of a fraxicon. Obviously, the axicon radius was doubled. This leads to an extended depth of focus.

This concept was experimentally realized by an axicon of a single phase-wrap with additional smoothed passage between the two conical parts (around R = 100 µm) to reduce diffraction effects as drawn in *Fig. 4.1.4*. In order to allow for a meaningful comparison, a continuous

and non-continuous axicon have been programmed to take account of the extended interference conditions. The diameters were D = 200 µm and D = 400 µm, respectively. The conical angles were identical and set to be around θ = 12 mrad for both axicons. In *Fig. 4.1.5* and *Fig. 4.1.6*, a comparison of the propagation properties of needle beams generated via a wrapped and an unwrapped axicon is shown. The axial position is different for both finite nondiffracting zones, however, the zone of the Fresnel-type axicon is clearly extended, almost doubled in length (Δz = 9 mm), at the cost of the number of needle beams (due to the increased axicon diameter and halved array period) within a given field of view.

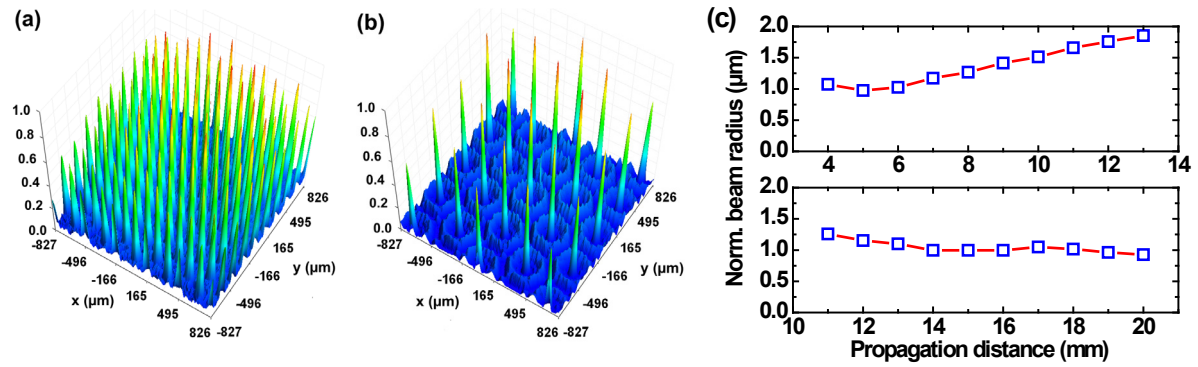

Fig 4.1.5 Arrays of degenerated Bessel-X pulses recorded by a CCD-camera: **(a)** Arrays of needle beams (array period p = 200 µm) at a distance of z = 7 mm, **(b)** arrays of extended-type needle beams (array period p = 400 µm) with doubled spatial period at z = 14 mm. The field of view is kept identical for both records, which is 1.65 x 1.65 mm^2. **(c)** Normalized beam radii of the conventional needle beam (top) and extended-type (bottom) as a function of the propagation distance.

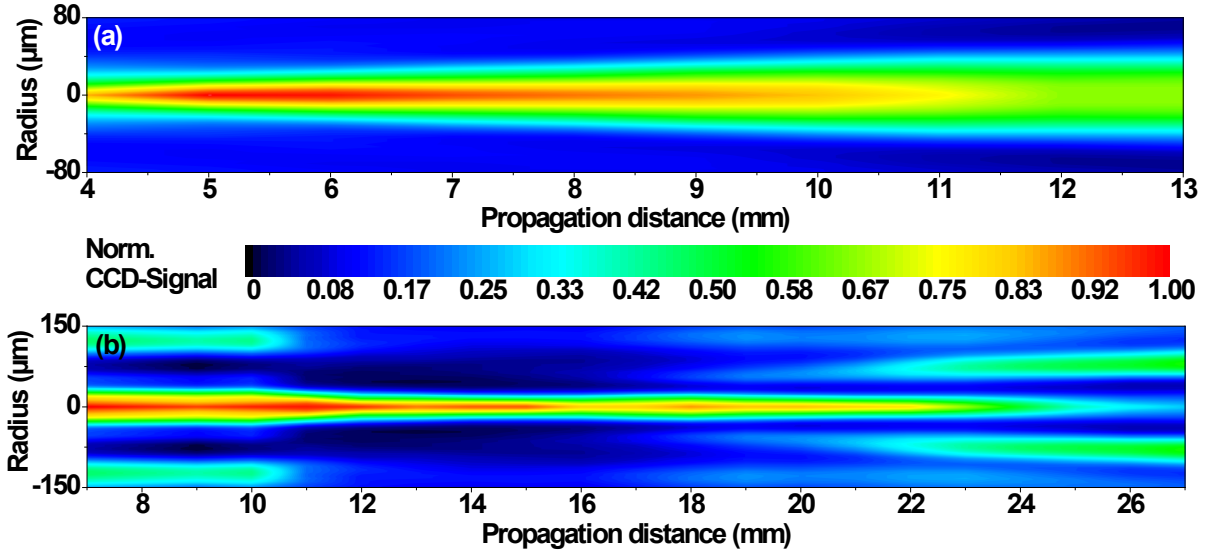

Fig. 4.1.6 Comparison of two pulsed needle beams and their nondiffracting zones for a conventional and a Fresnel-type axicon, **(a)** measured propagation behavior (time-integrated intensity profile) of a needle beam, **(b)** extended needle beam obtained by an additional cone structure around the regular axicon. The CCD-signal was normalized to its maximum within the measured range.

The $1/e^2$ beam radii for the conventional and extended-type needle beams were found to be 35 µm and 30 µm, respectively. Side effects of a combination of annular zones include additional rotational symmetric patterns surrounding the needle beam as plotted in *Fig. 4.1.6(b)*. However, within the fringe-less nondiffracting zone between z = 11 mm and z = 20 mm the effect is strongly suppressed. It is particularly noteworthy that the beam radius is approximately constant of this range with an almost constant intensity.

4.1.3 Aberration correction

Although microaxicons produce less aberrations than microlenses in the case of oblique incident light, very large angles (> 30°) require a correction of the induced aberrations. When the light beam illuminates the sample with a certain non-zero angle of incidence, the effective axicon shape changes from a circular to an elliptical area and the periodicity becomes shorter. For an optimized performance, both effects have to be reversed. In the experiments, an oblique angle of 50° was realized to test the ability of compensating aberrational effects by stretching the axicon into the corresponding direction. As schematically drawn in *Fig 4.1.7(a)*, the needle beams should show a uniform spot size over the cross section in spite of a large angle of incidence thanks to the nondiffracting properties.

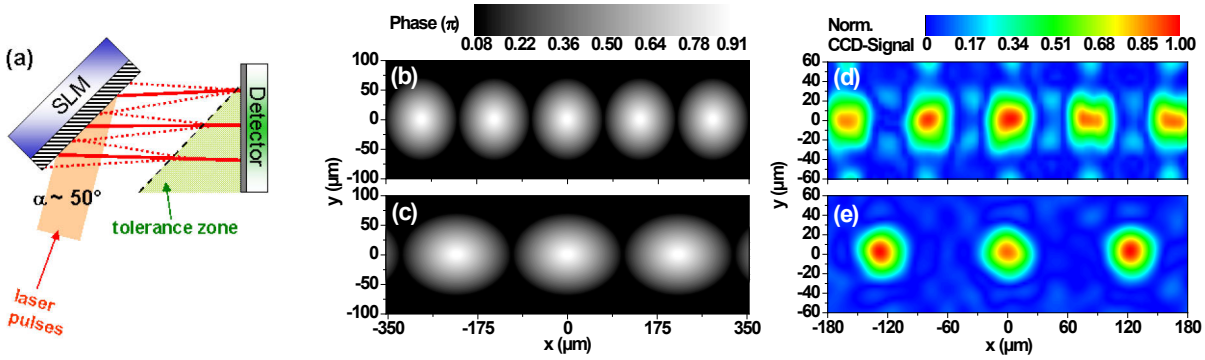

Fig. 4.1.7 Reshaping needle beams by correcting the aberrations induced at large angles of incidence: **(a)** The scheme shows the advantages of needle beams (red solid line) in comparison to conventional beams (red dotted line) generated with microaxicons and microlenses, respectively. **(b)** Initial rotational-symmetric axicon, **(c)** elliptical shaped axicons applied for the aberration correction, **(d)** corresponding aberrated needle beam array, **(e)** almost perfectly reshaped needle beam array.

The axicon itself has to be of elliptical shape to reshape the beam into a circular beam intensity profile with an improved energy concentration. In the particular case, the eccentricity of the axicons (p = 130 µm, θ = 11 mrad) was adapted from 0 (circular) to 0.47 (elliptical) with the final radii w_a = 70 µm (9 pixels) and w_b = 100 µm (13 pixels). The initial and final gray level distributions are compared in *Figs. 4.1.7(b, c)*. For each step of correction,

an image of the generated needle beam pattern was recorded by a CCD-camera at a distance of z = 6 mm (measured from the SLM-surface). The initial and reshaped needle beams are shown in the *Figs. 4.1.7(d, e)*. Simultaneously to the correction of the spot shape, also the lattice geometry was corrected from a rectangular (85 µm x 130 µm) back to a square shape (130 µm x 130 µm). In general, beam recovery is not restricted to one dimension. The free parameters allow to compensate distortions in any direction.

Figs. 4.1.8 (a, b) show two needle beam profiles captured at different transversal positions of the beam. The chosen axis was parallel to the direction of aberration or plane of incidence. Due to the large angle of incidence the total tolerance zone must be at least 3.3 mm. This is easily covered by the nondiffracting zone of the needle beams because both beams show similar beam profiles without additional distortions or cross talk effects. A closer look at the light distribution, however, reveals different beam radii due to the additional propagation path. A selected solitary needle beam was considered for a detailed analysis of the spatial uniformity.

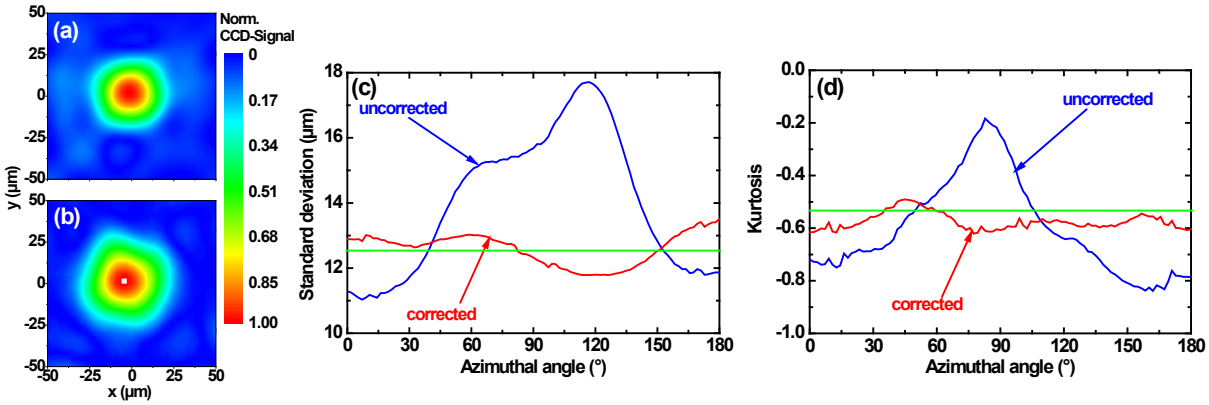

Fig. 4.1.8 Properties of aberration-corrected needle beams: **(a)** Reshaped spot intensity profile at x-position of x_1 = –1.375 mm, **(b)** and x_2 = +1.375 mm from the beam center, **(c, d)** comparison between aberration-uncorrected (blue) and -corrected (red) needle beam profiles by means of kurtosis and standard deviation. Centro-symmetrical cuts were analyzed as a function of the azimuthal angle. The green line indicates the ideal values for the standard deviation and kurtosis.

The *Fig. 4.1.8* illustrates by means of statistical parameters that the azimuthal uniformity is strongly improved by the above explained method of shape correction. Except of a weak oscillation, the standard deviation σ (*Fig. 4.1.8(c)*) of the beam intensity profile is almost constant at any azimuthal angle. The same applies to the kurtosis K (*Fig. 4.1.8(d)*) or "peakedness", respectively. The theoretical value (green line: K = -0.53) of the kurtosis of an ideal needle beam is found to be in good agreement with the corrected spot shape. The standard deviation and the kurtosis were calculated by:

$$\sigma = \sqrt{\frac{\sum_{i=1}^{n}\left[(r_i - r_{CG})^2 I(r_i)\Delta r_i\right]}{\sum_{i=1}^{n}\left[I(r_i)\Delta r_i\right]}} \tag{59}$$

$$K = \frac{\sum_{i=1}^{n}\left[(r_i - r_{CG})^4 I(r_i)\Delta r_i\right]}{(\sigma)^4 \cdot \sum_{i=1}^{n}\left[I(r_i)\Delta r_i\right]} - 3 \tag{60}$$

where r is the radial coordinate and $I(r)$ the radial-dependent intensity.

4.1.4 Diffraction-less self-imaging effect

The propagation behavior of a matrix of needle beams at distances beyond the depth of focus was also investigated. Specifically, for arrays of needle beams, a periodical reconstruction of the needle beam distribution is indicated. This self-imaging effect is due to interference conditions applied by the axicon arrays. An analogous phenomenon in optics is well-known as the Talbot effect [Tal36, Ray81, Cow57, Loh88, Ber96] and is based on the redistribution of light by periodical phase and/or amplitude objects. The integer Talbot distances $L_{T,diff}$ are defined as the planes where the initial field self-images can be calculated by the following formula:

$$L_{diff} = N\frac{2a^2}{\lambda} \qquad \text{N} = 1, 2, 3 \ldots , \tag{61}$$

where a is the spatial period of the initial pattern, λ the wavelength, and N an integer number. However, this diffractive Talbot effect is not applicable under the described experimental conditions. Diffraction effects are mostly suppressed in the case of phase-apodized axicon profiles. For this reason, only the specific interference conditions are responsible for the self-imaging effect (analogous to the Talbot effect). From the conditions one can define the following new relation:

$$L_{\text{int}} = (2N+1)\frac{a}{2\langle\theta\rangle} \qquad \text{N} = 1, 2, 3 \ldots , \tag{62}$$

A matrix of 36 x 36 elements was programmed into the SLM to measure the diffraction-free, polychromatic self-imaging effect at appropriated distances. The pulse had a duration around 10 fs directly behind the reflective LCoS-SLM because of the incomplete compensation of material dispersion within the beam path. The following experimental conditions were applied: Axicon diameter D = 120 µm (7 pixel), averaged conical angle $<\theta>$ = 7.5 mrad (maximum θ = 17 mrad), array period p = 100 µm, angle of incidence of around γ = 50°. The needle beam width ($1/e^2$) in the plane at z = 7 mm was measured to be w = 60 µm. The original pattern is repeated at a distance of z = 21 mm. The equation of the diffractive Talbot effect, however, leads to a wrong distance of $L_{T,diff}$ = 25 mm. In contrast, the diffraction-free self-imaging delivers a value around $L_{T,int}$ = 20 mm, which is close to the measured one. For both calculations a central wavelength of λ_0 = 800 nm was assumed.

The ring-shaped pattern should not be confused with the far-field of typical Bessel beams, which is also a ring. In this case, the hexagonal structure is responsible for the ring or more precisely for the honeycombed structure. The intensity is inverted similar to a photo-negative. Here, the diverging parts from the central axicon beam interfere with the converging parts of the 6 surrounding axicons. An extended depth of field was obtained by the decreasing axicon angle towards higher radii. Therefore, the end of the first Bessel zone (depth of focus) is achieved where the two comb-like pattern are meshed with each other as presented in *Fig. 4.1.*9. This happens at the axial position of around z = 10 mm.

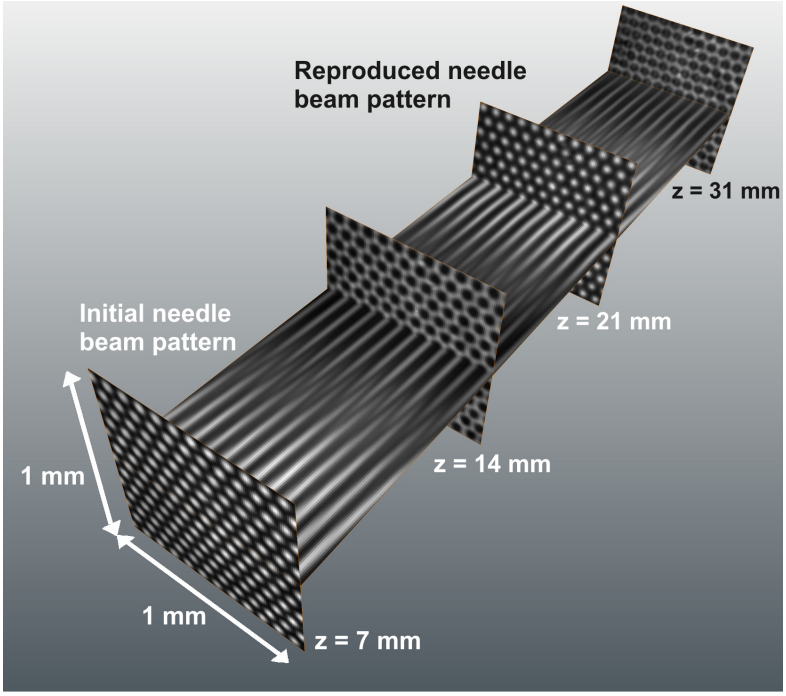

Fig. 4.1.9 Self-imaging of an array of needle beams at sufficiently large distances. In the experiments an axicon array of 36 x 36 elements was directly programmed into an SLM each having a diameter of 120 µm (not shown here). The angle of incidence was around 50° so that an aberration correction was included in the phase distribution. Please notice the inversion of positive and negative patterns.

4.1.5 Spatiotemporal properties of needle beams

The spatial reshaping of a Gaussian input profile into an array of nondiffracting sub-beams or more complex structures on the one hand side requires a simultaneous conservation of the pulse on the other hand side. For that purpose, it is necessary to take a detailed look at the spectral amplitude and phase, especially for the extended-type of needle beams. A spatially resolved second order autocorrelation via a 10 µm (broadband phase-matching) thick BBO crystal as a frequency converter was implemented to visualize the temporal behavior.

A hexagonal array of axicons (matrix period 720 µm, axicon radius R = 760 µm, conical angle θ = 2.3 mrad) was programmed into the SLM. The resulting phase mask was then illuminated by 'Laser B', delivering nearly Fourier-limited coherent light pulses in the range of 6.5 fs. The angle of incidence was around 43°, so that the beams were corrected for aberrations. The spatially resolved autocorrelation was measured by an EMCCD-camera within the nondiffracting zone at a chosen distance of z = 100 mm. At this distance, the radial beam radius w was found to be around 150 µm.

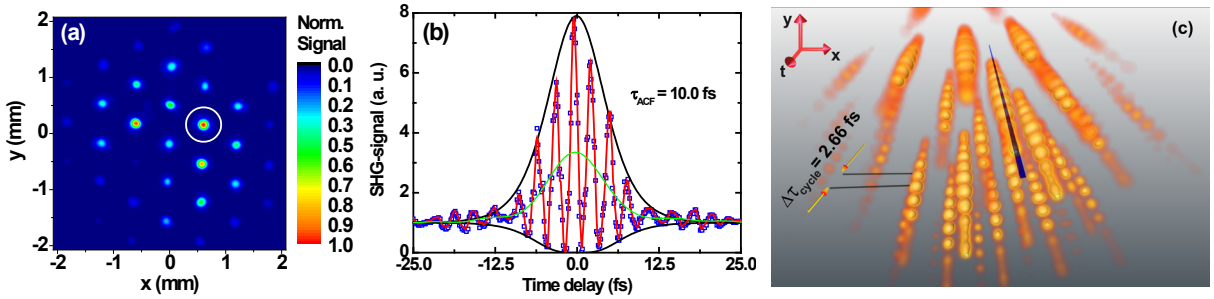

Fig. 4.1.10 Nonlinear characterization of multiple few-cycle wave packets at a distance of 100 mm generated by an array of conical profiles (axicons) programmed in the phase map of an LCoS-SLM: **(a)** detected light distribution by a EMCCD-matrix detector, **(b)** extracted 2nd autocorrelation trace of a selected needle beam (green solid line: low pass filtered autocorrelation function, black solid line: upper and lower envelope of sech^2-shape), **(c)** Spatiotemporal structure visualized by post-processing data of spatiotemporal 2nd order autocorrelation (fixed DC term added, size and brightness encoded according to the absolute value, perspective drawing of the isosurface with vanishing point). The line in (c) and the marked area in (a) indicates the corresponding needle pulse whose autocorrelation is shown in (b).

The frequency-doubled beam array is illustrated in *Fig. 4.1.10(a)*. It shows a hexagonal arrangement of spots each representing an independent highly localized wave packet (hail of light bullets). The missing needle beam at the spatial position x,y = 0.5 mm is due to a shadowing effect by dust on the surface of the nonlinear crystal or other light absorbing barriers within the detection system. *Fig. 4.1.10(b)* shows that the pulse at the output (τ_p = 6.8 fs) is negligibly broader than the input pulse. In both cases, a secans hyperbolicus pulse shape

was assumed. The spatiotemporal reconstruction of the complete 2D-autocorrelation data in *Fig. 4.1.10(c)* is interpreted as a visualization of the electric light field distribution in free space assuming a Fourier-limited pulse. The distances of neighboring maxima indicate the cycles of the electric field (2.66 fs at 800 nm central wavelength).

The results demonstrate that the extended-type of needle beams shows excellent nondiffracting properties in the spatial domain. For ultrashort pulse applications the behavior in the temporal domain is of interest as well. The resulting interference field is more complicated (diffractive + conical waves) for Fresnel-type axicons than for unwrapped axicons and results in a more complex temporal behavior. Thus, it is necessary to measure the pulse duration not only at a single axial position but also as a function of the distance.

A fraxicon similar to profile shown in *Fig. 4.1.4* was programmed into the SLM but with a modified parameter set: matrix period p = 1200 µm, axicon radius R = 600 µm, conical angle θ = 4.0 mrad. Again the micro-display were illuminated by 'Laser B' with pre-chirped (negative quadratic phase) pulses. The needle beams behave like nondiffracting beams within the measured range as shown in *Figs. 4.1.11(a-c)*, however, the needle beam expands slightly faster than in the case discussed above. This is due to the comparable axicon diameter and input Gaussian beam diameter and its beam divergence. The result of the temporal second order autocorrelation traces at various axial distances (step size: 10 mm) is shown in *Fig. 4.1.11(d, e)*. The pulse duration is about 6.9 fs independently of the axial position.

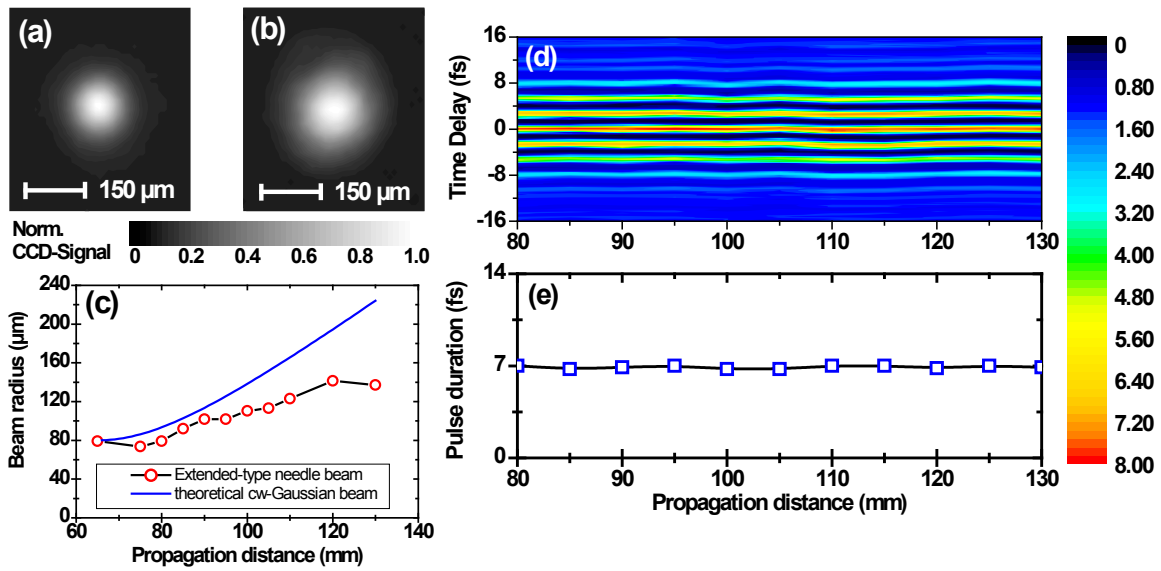

Fig. 4.1.11 Nondiffracting and nondispersing properties of extended-type of needle beams: **(a)** Needle beam profile at z = 65 mm and **(b)** z = 105 mm, **(c)** beam radius ($1/e^2$) of the needle beam (red open circles) as a function of the axial distance in comparison to a monochromatic Gaussian beam (blue solid line) **(d)** 2nd order autocorrelation trace as a function of propagation distance, **(e)** retrieved pulse duration (around 6.9 fs) at selected axial distances.

4.1.6 Beam parameter product of needle beams

It should be noted that the propagation behavior of microscopic needle beams is completely different from the properties of Gaussian beam foci [Ald02]. This fact is demonstrated by the contradiction of different values for the Rayleigh range using the Rayleigh criterion (doubled beam area at half intensity) as specified above. The contradiction becomes more pronounced with decreasing diameter of the needle beams.

For this purpose, the above discussed case of needle beams with a radius of 145 µm are analyzed to test the proposal of a tailored beam quality factor suitable to describe the propagation properties of needle beams qualitatively. For the standard deviation of the smallest beam radius and main spatial frequency, values of 73 µm and 1/(1300 µm) were found, respectively. The corresponding minimum quality factor is then:

$$M_{NB}{}^2 = 24 \cdot \sigma_0 \sigma_\infty = 24 \cdot 73\mu m \cdot \frac{1}{1300} \frac{1}{\mu m} = 1.35\,, \tag{63}$$

showing that this needle beam is not optimally shaped yet. The reason is the relatively large axicon diameter compared to the input Gaussian beam. Under this condition, the k-vector distribution and divergence reduce the quality of the needle beam. The axial dependence of the quality factor is plotted in *Fig. 4.1.12*. The increase shows that the nondiffracting behavior of this needle beam is only achieved in the range between z = 30 mm and z = 90 mm where $M^2 < 1.41$.

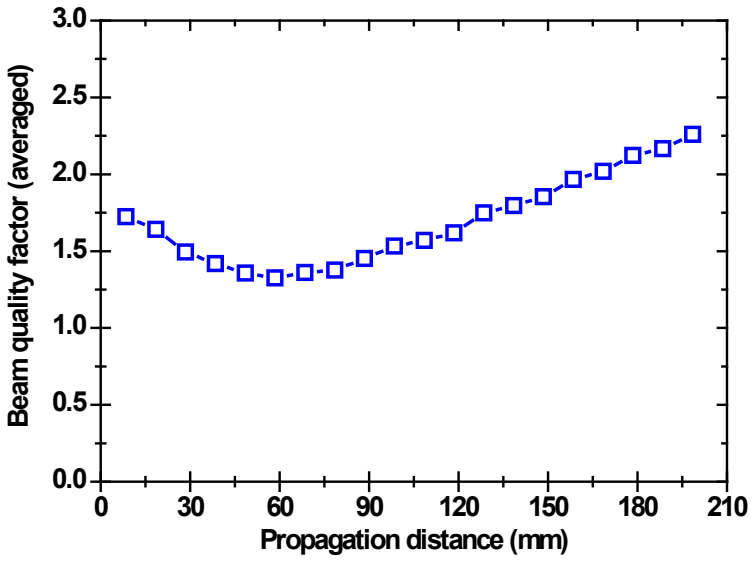

Fig. 4.1.12 The graph shows the axially dependent spatial beam quality factor $M_{NB}{}^2$ of a needle beam.

4.1.7 Limitations of spatial shaping

Needle beams or highly localized wavepackts are generated by writing ultraflat axicon profiles into an SLM, with the advantage of a temporal nondispersing and spatial nondiffracting propagation, extraordinarily high angular tolerance and self-reconstructing capabilities in space and time. However, in the generation process there are two main issues of concern, i.e., the accuracy of the axicon profile defined by the spatial resolution of the SLM and the nondiffracting zone restricted by the particular axicon diameter and profile.

It was shown that the influence of the pixel grid of the SLM (as a two-dimensional grating) on the shaping conditions is rather negligible. This is valid when the first and higher diffraction orders are deflected sufficiently far away from the important zeroth-order beam. To give an example, the zone of an undisturbed propagation is achieved at axial distances of about 10 mm assuming a pixel period of about 8 μm and an input beam diameter of 2 mm. The situation becomes more critical when HLWs are shaped in proximity to the SLM. Then, the diffraction orders superimpose coherently and the beam intensity profile is significantly deformed. Certainly, the spectral separation is small at these short axial distances. Nevertheless, the diffractive Talbot effect may have an important influence on the pulse duration for axial distances very close to the SLM (near-field, < 300 μm). For this reason, it is not applicable to program axicons beyond the Shannon limit (here: with diameters less than 5 pixels). A further criterion examined is that an implementation of a smoothed axicon shape can not be realized because of the low pixel number. Thus, diffraction effects at the aperture are enhanced, resulting in significant distortions of the beam. In conclusion, the signal-to-background ratio and beam quality are mainly influenced by the particular chosen phase pattern. The applied interference conditions (considering spatiotemporal effects) is the decisive factor here.

The nondiffracting zone of HLWs is exclusively determined by the diameter of the axicon like in the case of finite Bessel-like beams. Thus, the equation

$$z_{\max} = \frac{R^2}{\lambda} \tag{64}$$

defines the maximum extension of the nondiffracting zone, as shown in *Fig. 4.1.13(a)*. Obviously, it shows a quadratic dependence. This behavior is linked to the self-apodizing conditions for obtaining needle beams. It must be noted that in the case of phase apodized

axicons the range of superposition is extended due to the very small angles at the center and the rims. This is schematically visualized in *Fig. 4.1.13(b)*.

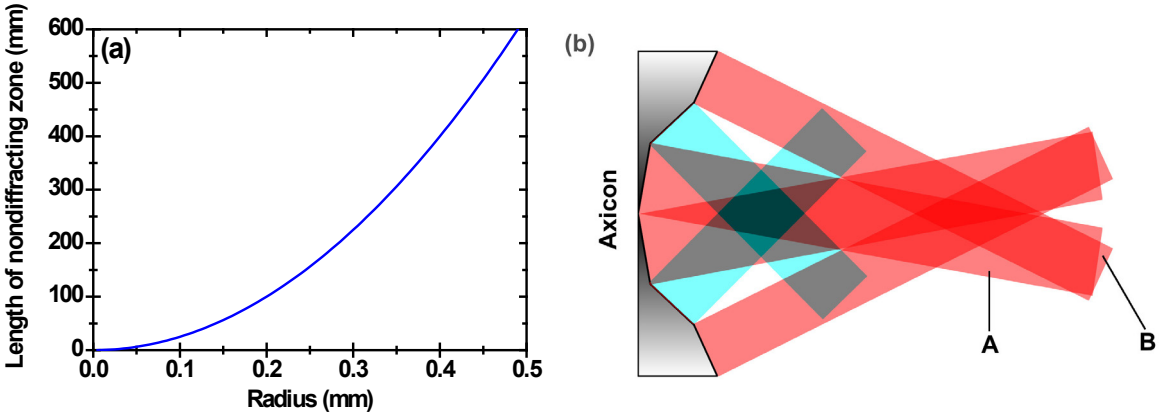

Fig. 4.1.13 Depth of focus of needle beams: **(a)** Maximum depth of focus as a function the axicon radius, **(b)** scheme of the interference conditions for non-conical axicons. The blue parts corresponds to waves with a relatively high conical angle whereas the red parts are waves deflected from the center (A) and outer part (B) of the axicon. The axicon angles are deliberately exaggerated to emphasize the interference conditions.

With this approach, needle beams as parts of arrays remain spatially separated over much longer distances in comparison to needle beams generated by pure conical shapes. However, the beam expands during the propagation. A detailed view on the results of the self-imaging effect in chapter 4.1 reveals an extension from z_{max} = 3.5 mm (conical axicon profile) to z_{max} = 7 mm (Gaussian-like axicon profile).

The conditions and procedure for the generation of needle pulses specified in the entire section are an important contribution to understand the spatiotemporal peculiarities of highly localized wave packets. They will be used in the following to analyze the more general case of ultrashort pulsed light beams with nondiffrating, nondispersing properties. Independent on the final light distribution the basic generating phase profile is always an ultraflat axicon. A generalization of this term is the aim of the next two sections.

4.2 Pulsed hollow beams with zero orbital angular momentum

The excellent propagation behavior of needle beams has revealed the potential of other axicon-type shapes to generate ring-shaped needle beams as discussed throughout this chapter. Hollow beams are generated by programming reflective axicons of W-shape into an LCoS-SLM. The procedure was similar to that used in the generation of quasi-nondiffracting needle beams. The described concept is easier to implement in comparison to methods using an axicon telescope configuration or adding a spiral phase. This is valid for both solitary and multiple hollow beams. Contrary to higher order Bessel beams, the formed tubular beams propagate fringeless over a large depth of focus and thus concentrate the energy in a single ring without parasitic oscillations. Note that without further efforts such beams carry no orbital momentum due to the diverging and converging partial wavefronts generated by the W-shaped axicon. The resulting interference pattern forms a quasi-nondiffracting beam similar to a needle beam but showing a central minimum.

Conical shapes were adjusted by adding a certain Gamma-function to the linear gray level distribution. This ensures a fast and simple access to reshape a general input function. In the experiments this was exploited to produce a high contrast ratio and a linearization of the gray level dependent phase response. The axicon was divided into two independent parts for a more flexible shaping of the hollow beams: (i) the inner part of convex shape with radius r_i and (ii) the outer part of concave shape with radius r_a. Both radii were tuned, however, the total radius $R = r_i + r_a$ was programmed to have always a constant value. A fine-tuning of the ring diameter of the generated hollow beam was achieved by a fine adjustment of the conical angles. In the following section, aberration-uncorrected and -corrected single and arrayed tubular beams are analyzed with respect to their spatiotemporal propagation behavior.

4.2.1 Solitary hollow beams

The curves in *Fig. 4.2.1(a)* show the realized solitary axicon profile and a fit function. To reduce the diffraction at sharp phase rims, a super-Gaussian shape (exponent 2.5) was implemented. The axicon angles for the rims are almost zero. This is understood as an axially increasing aperture, suppressing unwanted diffraction. Consequently, with this phase apodization, axial intensity oscillations were discriminated to a large extent. Axicon diameter and maximum axicon angle at the center wavelength were chosen to be D = 2.8 mm and θ = 2 mrad, respectively. The overall averaged angle was $\langle\theta\rangle$ = 1.6 mrad. The phase pattern was illuminated with 12 fs pulses from Ti:Sapphire laser oscillator (‘Laser A’).

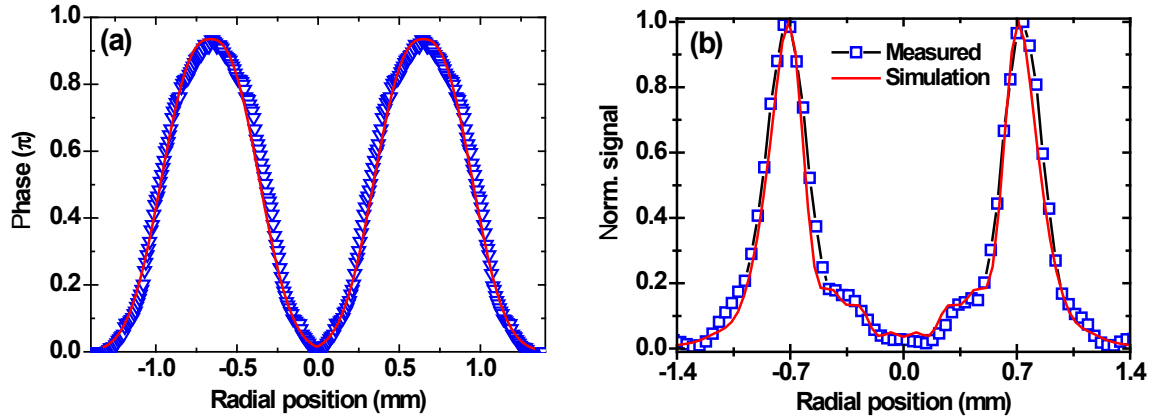

Fig. 4.2.1 Toroidal axicons and hollow beams: **(a)** Theoretical (red solid line) and experimentally approximated (blue triangles) radial phase distribution of the toroidal axicon programmed in the SLM (super-Gaussian, order 2.5). The total axicon diameter was set to be D = 2.8 mm with a maximum angle α_{max} = 0.060°. **(b)** Radial profile of the tubular beam at z = 300 mm measured (blue squared dots) and simulated data (red solid line).

The detected and background-corrected ring-shaped tubular beam (blue squared dots in *Fig. 4.2.1(b)*) is free of parasitic side lobes but shows a small tail towards the center. For simplicity, pixel separation (diffraction), exact axicon shape and discrete phase steps are ignored in the numerical simulations. Only a linear torus axicon consisting of a concave and convex part was considered. Here, the axicon base angle was set to be α = 0.8 mrad for the inner part as well as for the outer part referring to the programmed axicon. Under Gaussian beam illumination, both propagating wavefronts superimpose on each other and form a ring-shaped intensity profile, shown as the red solid curve in *Fig. 4.2.1(b)*. The obtained theoretical result (numerical simulation executed with "Virtual Lab") fits very well to the measured data. The full intensity reconstruction of the 3D dataset for the measurement and simulation, respectively, is visualized in *Fig. 4.2.2(b,c)*.

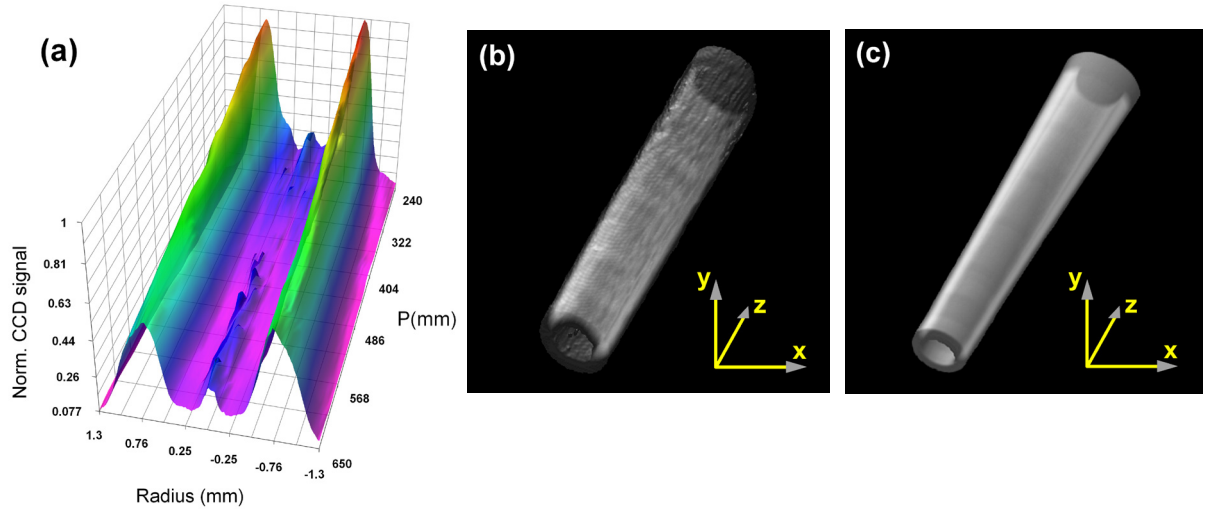

Fig. 4.2.2 Axial and radial intensity distribution of a solitary hollow beam: **(a)** Axial intensity cut through the center of the an ultrashort-pulsed solitary dark hollow beam generated with an LCoS-SLM. 3D reconstruction of the measured **(b)** and simulated **(c)** structure of the extended intensity propagation zone (axial distances z: 240-640 mm, FOV about 1.6 x 1.6 mm^2, incident angle 20°).

Maxima of intensity and contrast appear at different distances (z_{imax} = 240 mm, z_{cmax} = 410 mm) as shown in *Fig. 4.2.2(a)*. Close to the SLM, the initial Gaussian profile looks still undistorted (no tubular structure). Then, the central part of the beam shaped by the central region of the axicon starts diverging whereas the outer part begins to converge. The ratio of both propagating parts is expected to be unbalanced within the relevant range. This is on the one hand due to the natural divergence of the input laser and results in a smaller converging angle. On the other hand side it results from the different energy ratios at the center and at the edge of the beam spot. The ring contrast is almost constant over the entire range and achieves averaged values of about 65 % (C_{max} = 75%).

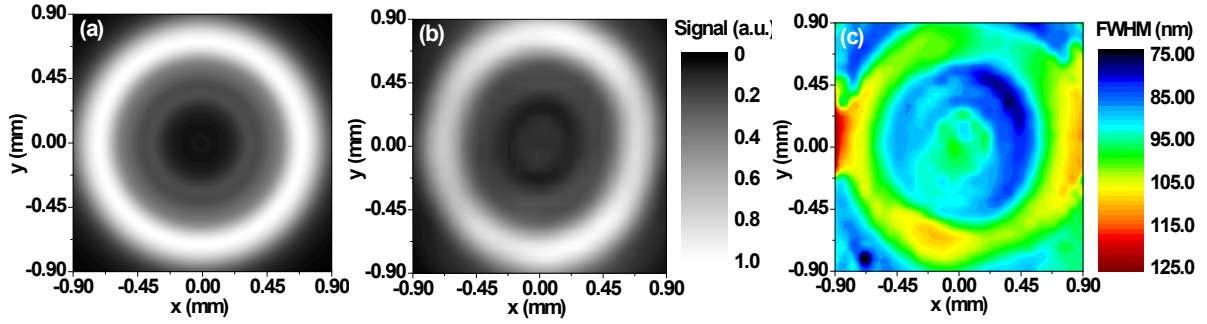

Fig. 4.2.3 Intensity and spectral properties of the hollow beam. The data were obtained by a spatially resolved measurement of the spectrum across the beam profile at a distance of z = 300 mm via the fiber-based scan method (resolution 15 µm): **(a)** Theoretical and **(b)** measured spectrally integrated intensity distribution, **(c)** map of the spectral width (FWHM) retrieved from spectral data.

Temporal and spectral transfer were studied by spectral mapping and autocorrelation at a distance of z = 300 mm from the display with a spatial resolution of 40 µm. The retrieved intensity profile is shown in *Fig. 4.2.3(b)* in comparison to the simulated distribution in *Fig. 4.2.3(a)*. Both the eccentricity (e = 0.32 ± 0.04) and the azimuthally dependent intensity fluctuations are caused by the off-axis illumination. Consequently, the focal strength was then slightly different in each direction resulting in a more homogenized intensity pattern. For the few-cycle hollow beam (see below) these two drawbacks were compensated by narrowing the axicon in the corresponding direction taking an unchanged phase stroke into account. The spectral map in *Fig. 4.2.3(c)* indicates a homogeneously distributed spectral width (FWHM) within the ring structure. Within this range, the pulse duration did not change significantly if a non-varying spectral phase at each spatial position was assumed. By comparing averaged input and output spectra, only a small reduction of the FWHM by chromatic aberrations in the SLM is observed (3 nm). The pulse duration as retrieved from the intensity autocorrelation was determined to be in the range of 23 fs measured at various position of the hollow beam. The pulse broadening is primarily caused by dispersion in the cover glass of the SLM. For the analysis, marginal pre- or post-pulses were neglected.

A second series of experiments was performed with 'Laser B' providing shorter pulses. Here the temporal dispersion induced by the cover glass was precompensated by double chirped mirrors inserted between Laser and SLM. Independent measurements (SPIDER) of the pulse duration at positions close to the SLM confirmed the recompression to pulse durations of τ = 6.5 fs. Minimal effects of spatial aberrations caused by oblique illumination were corrected. The propagation behavior of the frequency converted hollow beam (λ_0 = 400 nm) is plotted in *Fig. 4.2.4*, starting at the maximum intensity and smallest beam radius. The intensity was normalized for each measured distance step. Spatially resolved 2nd order autocorrelation traces were recorded at various distances. In *Fig. 4.2.5* only the spatially integrated autocorrelation is shown. The wave packet is nondispersing and nondiffracting (yellow line at $1/e^2$) within the error bar of the retrieved pulse duration and the radius of the dark region. In comparison to the previous hollow beam this is a significant improvement, especially in the longitudinal localization of such short pulses.

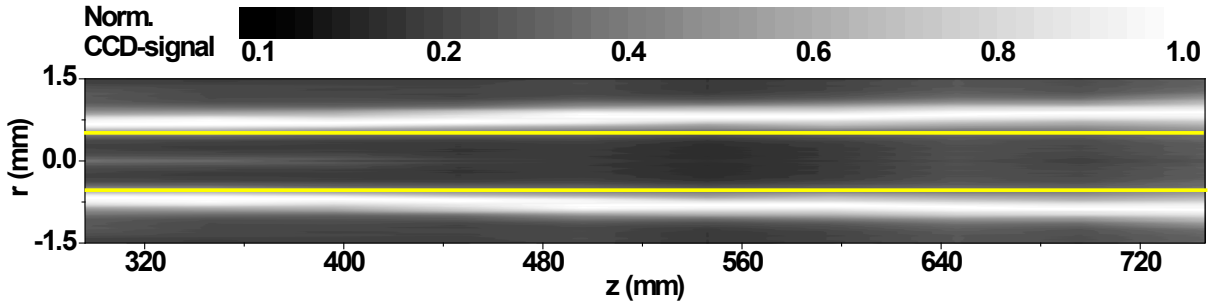

Fig. 4.2.4 Nondispersing and nondiffracting solitary hollow beam. Axial propagation behavior retrieved from azimuthal averaged intensity cuts. Each cut profile was normalized to its maximum intensity. The yellow line indicates the position of equal intensities.

The thickness of the light ring increases over the measured propagation distance while the size of the dark region is nearly constant. Specifically, a thickness of D = 420 µm was measured at a distance of z = 300 mm whereas the thickness increases to D = 660 µm at z = 750 mm. This value is still a 2.3 times smaller than the expansion factor of a monochromatic Gaussian beam at the same wavelength (λ_0 = 800 nm) and distance (z = 750 mm). No significant broadening of ring thickness and diameter is observed when investigating the evolution of the hollow beam only within the Rayleigh range (between 300 mm and 475 mm) defined by a Gaussian beam of equal waist size. In this range, the intensity is also almost constant.

For comparison, autocorrelation measurements of the unshaped Gaussian beam with passive SLM acting as a mirror were performed. *Fig. 4.2.5(a)* shows that the τ_p = 6.4 fs hollow beam pulse experiences no broadening in the time domain while propagating over large depths of

field. In contrast to this, the Gaussian beam is obviously affected by dispersion, the pulse duration increases from τ_p = 6.4 fs to 8.3 fs (*Fig. 4.2.5(b)*). The amount of broadening is close to the theoretically predicted value if one assumes a dispersion length of 720 mm in air.

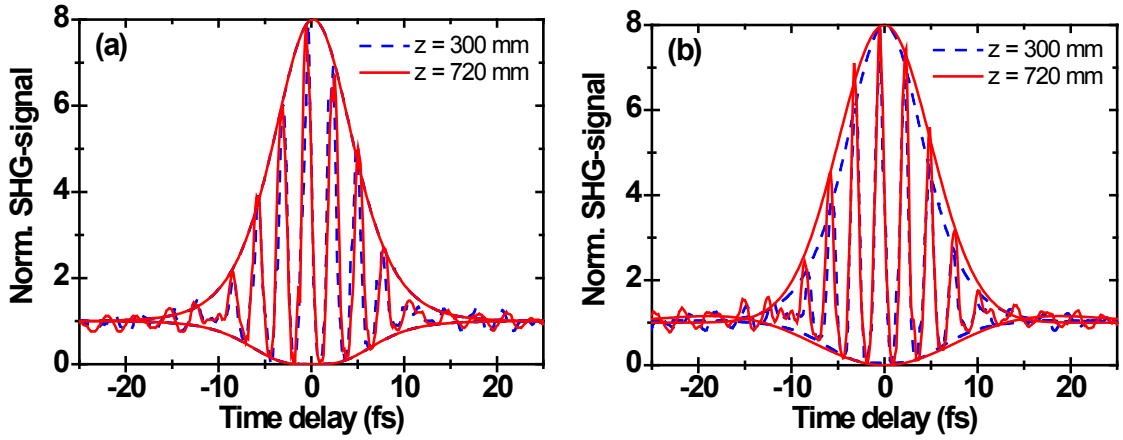

Fig 4.2.5 Second order autocorrelations of the hollow beam and the Gaussian beam at two distances from the SLM (blue: z = 300 mm, red: z = 720 mm): **(a)** 2nd order autocorrelations of a solitary hollow beam autocorrelations, **(b)** 2nd order autocorrelations of the unfocused Gaussian beam.

4.2.2 Arrays of hollow beams

Arrays programmed in pixilated SLMs are generally constrained to a limited number of pixels for each element in comparison to the above discussed solitary axicons. The discretization appears now more relevant with respect to the final shape and the induced diffraction caused by huge phase steps from pixel to pixel. Two cross-cuts of a solitary microaxicon are plotted in *Fig. 4.2.6(a)* showing two different states of the inner and outer radius. Both curves are approximately fitted by a super-Gaussian functions of the same order as in the case of the single torus axicon.

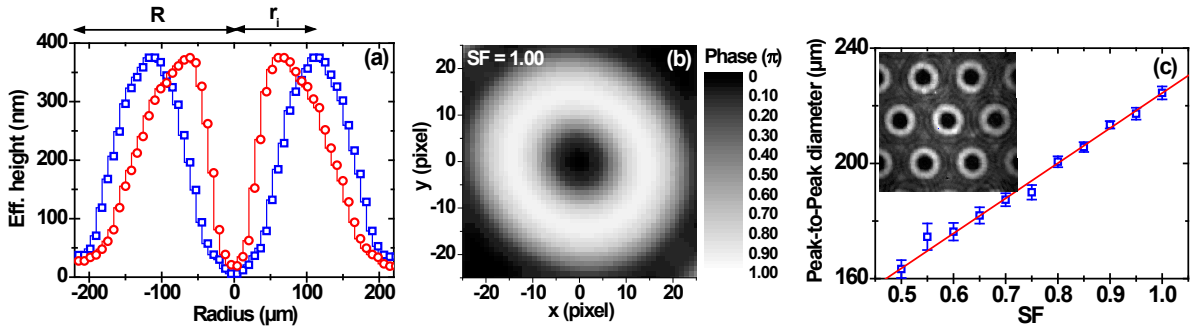

Fig. 4.2.6 Tunability of the inner and outer radius of microaxicons to influence directly ring diameter of the resulting hollow beam: **(a)** Axicon phase function for two symmetry factors *SF* = 0.5 (red circles) and *SF* = 1.0 (blue squares), respectively, **(b)** Corresponding gray level representation of the spatial phase distribution for *SF* = 1.0 with a slight ellipticity for aberration correction, **(c)** Tuned peak-to-peak ring diameter of a hollow beam. The inset shows the hollow beam array for a *SF* = 0.8 at a distance of *z* = 8 mm.

The higher the gradient of the effective refractive index change of the LC-layer is the higher is the deflection angle. This relationship is expressed as an effective height of the

programmed axicon. In the presented case the radial position of the maximum height varies between 65 µm and 114 µm for SF = 0.5 and SF = 1.0, respectively. The ratio $SF = 2r_i/R$ defines the symmetry of the axicon shape. Note that the total radius R remains unaffected while the W-shape is tuned. The corresponding maximum diameter was set to be around 450 µm. For each element an area of 56 x 56 pixels was used (*Fig. 4.2.6(b)*). However, an aberration correction was implemented corresponding to an elliptical shape. The programmed fill factor was about 97 %.

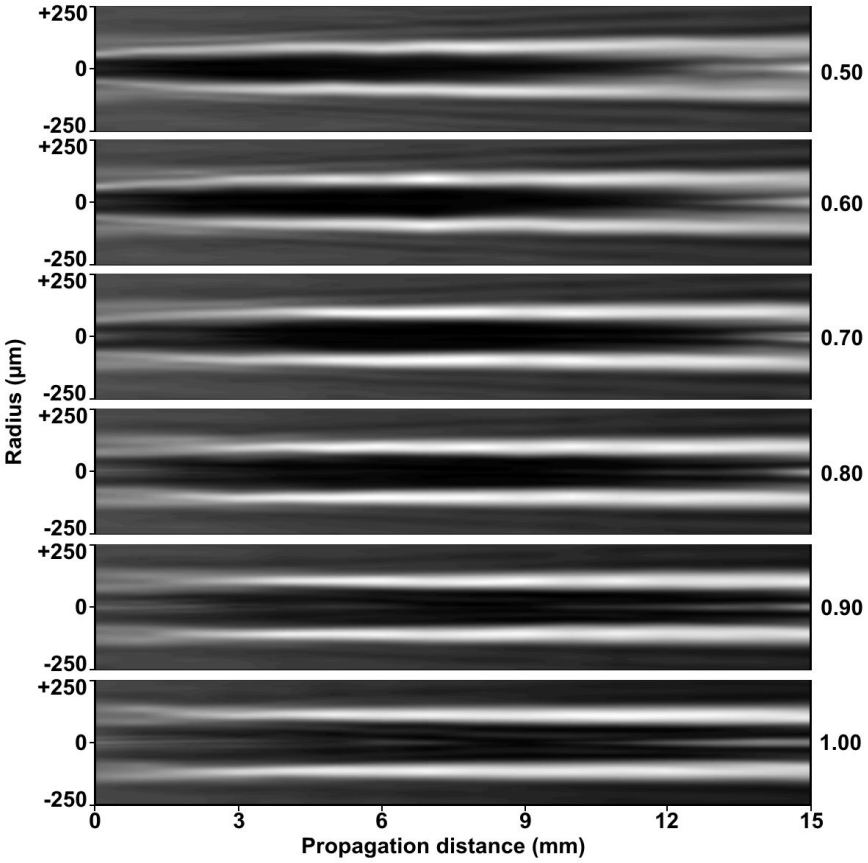

Fig. 4.2.7 Axial evolution of the ring shape for a solitary hollow beam extracted from the array. From top to bottom the symmetry factor is tuned between 0.5 and 1.0 in steps of 0.1. Here the field of view is chosen to be 490 µm (radius) x 15 mm (distance). The nondiffracting character of the dark hollow beams is clearly visible.

For the case, that the two radii of the axicon are unequal at a fixed axicon height of h = 400 nm (π), the wave vectors are generally oriented in slightly different directions as a result of two not identical axicon angles. This comes along with axial-dependent diameters of the hollow beams and ring thicknesses as shown in *Fig. 4.2.7*. A further aspect is the axially curved structure, however, the contrast is very low with respect to the surrounding parts and the bending is located very close to the SLM. In the case of SF = 0.5 the radial position of the peak value (start: 55 µm, end: 90 µm) increases asymptotically with increasing distance. These caustic effects are due to the different axicon angles used for the generation.

The peak-to-peak diameter was controlled by the axicon symmetry as shown in *Fig. 4.2.6(c)* at a fixed axial position. A section of tubular beam arrays is shown in the inset. A nearly linear dependence of the symmetry factor was found. The diameters expand whereas the periodicity stays constant. Based on the aforementioned experimental boundary conditions hollow beams with diameters in the range of 160 µm – 230 µm were produced.

The involved pixel number for the inner radius is strongly reduced to 7 pixels for $SF = 0.5$. The phase difference from pixel to pixel was then around 100 nm. Hence, an induced diffractive effect is observed (*Fig. 4.2.7*) in weak concentric rings around the dark hollow beams radiating outwards. With increasing *SF*, however, the amount of diffraction decreases, so that the background fluctuations get more homogeneously distributed. Notice that for the conical profile of an axicon the phase step height should be less than $\lambda/4$ to satisfy the requirement of a continuous phase profile. Otherwise, these elements resemble more diffractive than refractive micro optics.

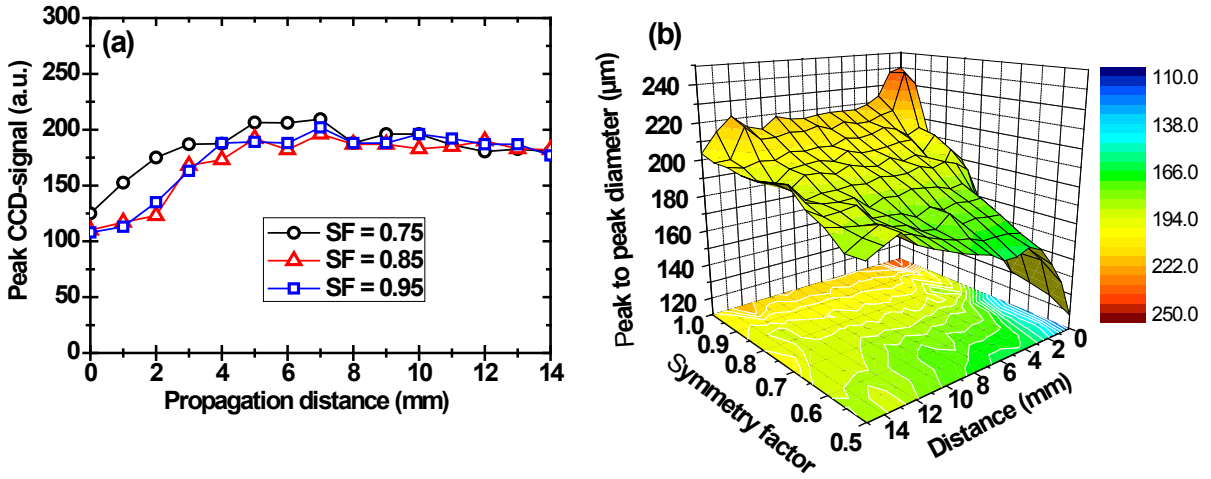

Fig. 4.2.8 Propagation properties of microscopic hollow beams: **(a)** Evolution of the peak intensity for different *SFs*. **(b)** Peak to peak diameters as a function of the axial distance and shrink factor.

The real profile of smoothly decaying phase leads to a very small amount of deflection at the outer parts, hence, a remaining background level is detected. Most of the disturbance of ring-shaped intensity profile origins in interference effects caused by optical density filters within the imaging path of the CCD-camera. Looking at $SF > 0.75$ within the first two millimeters, the conical wave parts are still separated from each other so that the principle of Bessel beam generation is visualized. The shape of the dark region depend strongly on the peak separation. At a distance of $z = 8$ mm all hollow beams exhibit the highest contrast ratio independent of the particular *SF* value of the torus axicon. The beam is not attributed to a spreading of the diameter or laser energy decrease, especially for *SF* values between 0.75 and 1.00 as it is shown in *Fig. 4.2.8*. However, the contrast due to the central dark region and surrounding part

has to be taken into account. The contrast is obviously zero directly on the SLM surface because of the absence of interference. Generally, the contrast exceeds 50 % for distances greater than 2 mm or 4 mm, respectively, depending on the programmed symmetry factor. The pseudo nondiffracting characteristic with high contrast extends at least over a range of 12 mm discarding *SF* values below 0.6. In the experiments, the pulse duration for the hollow beams was in the range of 20 fs but can be adapted to 6.5 fs as it was shown above for the solitary hollow beam.

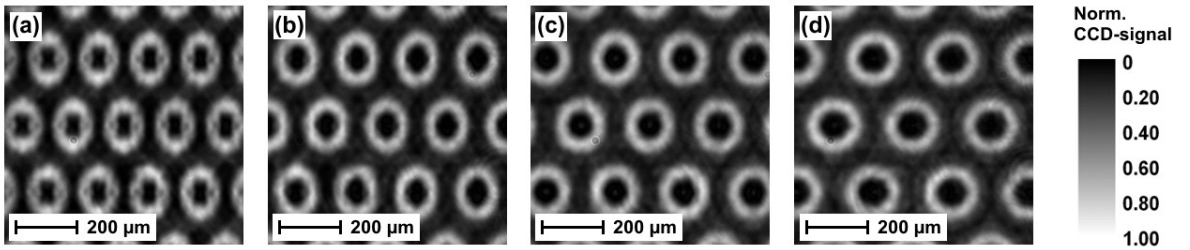

Fig. 4.2.9 Normalized intensity distribution (background corrected) of arrays of hollow beams at different states of the aberration correction. The axicon was deformed from a circular into an elliptical shape. The following factors are related to ratio of the long axis to the short axis of the axicon element: **(a)** 1.00, **(b)** 1.18, **(c)** 1.36, and **(d)** 1.54.

A correction of the beam aberration at large angles of incidence was obtained in the same way as realized for needle beams. The evolution from aberrated to nearly distortion-free hollow beams is presented in *Fig. 4.2.9*. The chosen angle of incidence was about 50°. All hollow beams within the array show a clear elliptical shape when a correction of the spatial aberrations is excluded. The intensity distribution of the ring varies considerably with the azimuthal angle. The reason are the non-equal sizes of the axicon profile at oblique incidence, resulting in an asymmetric interference pattern. The original circular shape (see *Fig. 4.2.9(d)*) is recovered for eccentricities of the axicon shape of $e = 0.76$.

As mentioned recently, the introduced needle beams are not restricted to rotational-symmetric distributions with maximum intensities located in the center. It was shown how with axicon profiles of toroidal shape hollow beams were obtained contributing nondiffracting and nondispersing properties. It is an essential feature that the invariance of the temporal structure of nondiffracting pulses is also valid for ring-shaped or even more complex degenerated Bessel-X pulse as introduced in the next chapter.

Up to now, such localized waves were only be reported as pulsed Bessel or Airy-Bessel beams still exhibiting transversal oscillations, which limit the spatial localization. With the introduced approach, a broad range of axicon phase masks were programmed into the SLM to realize various shapes of highly localized wave packets showing nonspreading properties

independent on the specific spatial distribution. Mathematically, HLWs were generated from needle beams by applying simple geometrical transforms (linear stretching and/or rotation). This leads to modified symmetry properties at persistently small spatial and temporal distortions at pulse durations down to a few femtoseconds.

4.3 Highly localized wave packets (HLWs) as generalized light bullets

Selected highly localized wave packet distributions were discussed in the previous two chapters, including needle and hollow beams. These particular types of beams are part of a bigger family of basic generalized functions, which can be derived from specific shapes of symmetric and asymmetric axicons. In this chapter, other pulsed, nondiffracting light fields are examined. In chapter 4.4 it is shown how such HLWs are used as building blocks for more complex pulsed light fields.

Starting from the radially symmetric needle beam, HLWs are obtained by specific mathematical transforms modifying the symmetry of the beam or combining multiple coherent sub-beams to nondiffracting patterns of higher complexity. A common property of all members of this family of generalized needle beams is to localize the energy in defined minimum volumes of space-time compared to Bessel beams where it is spread over an infinite (theory) or finite (experiment) number of fringes. Here the term “highly localized beams” (HLB) is used for this new particular class of ultrashort-pulsed nondiffracting wave phenomena.

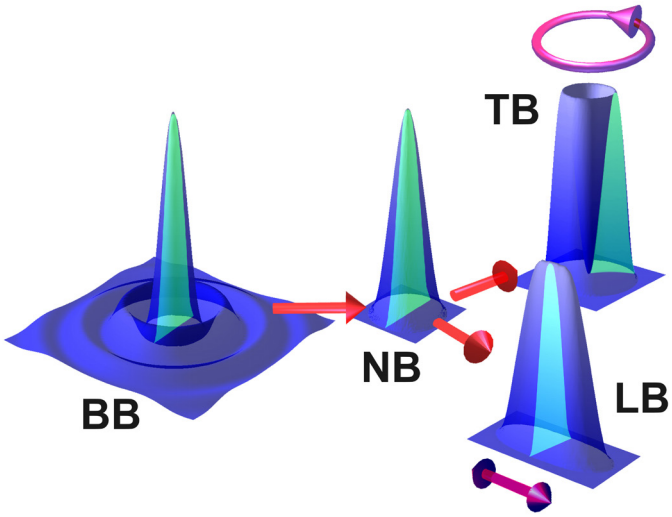

Fig. 4.3.1 Principle of generating highly localized wave packets (HLWs). Self-apodized (diffraction-free) spatial filtering of a pulsed Bessel beam (BB) is used to generate a radially symmetric needle beam (NB). By linear and circular transform algorithms (circular and double arrow), non-radially symmetric profiles of stretched (linear beam, LB) and tubular structure (tubular beam, TB) are obtained. The propagation remains quasi-nondiffracting in the spatial and temporal domain.

A scheme of selected spatial shapes (intensity distribution) is drawn in *Fig. 4.3.1*. In the following experiments, only selected transition shapes were realized, however, other configurations are possible. Here, the degrees of freedom for an axicon shape programmed into a spatial light modulator are reduced to a minimum number of shape parameters: averaged axicon angle, angle distribution function, axicon size and symmetric or asymmetric

spatial shapes (*Fig. 4.3.2*). On the one hand, the spatial phase map mainly determines the spatial intensity distribution (line, ring or other shapes). On the other hand, the precise interference conditions are manipulated by the particular phase function (linear, Gaussian, etc.). A change of the shape parameters is exploited to cause a change of the nondiffracting zone properties. The relationship between spot profiles and propagation characteristics can be significant (e.g. fraxicon) and may be used to increase the performance of pulsed nondiffracting complex light fields. The advantage of refractive-based ultraflat axicons with a fixed phase profile exploiting the maximum phase range between 0 and π is that they are scalable. With decreasing axicon size the expansion of the beam decreases as well. The boundary condition to obtain a needle beam is intrinsically fulfilled at any size of the axicon.

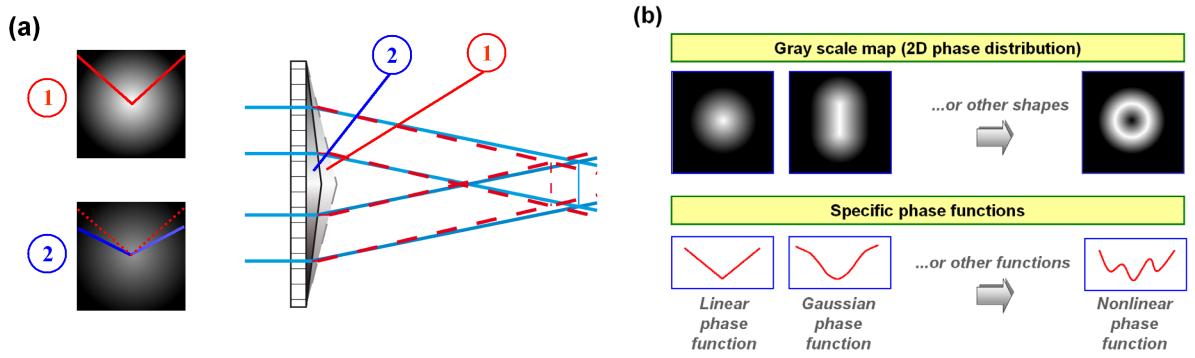

Fig. 4.3.2 Scheme demonstrating the flexibility of programming different axicon-like phase distributions into an SLM: **(a)** Scheme of tuning the axial center position of the nondiffracting zone of needle beams by changing the axicon angle (gray level tuning) **(b)** Corresponding gray level maps of selected types of axicon shapes with conical and non-conical intersections.

4.3.1 Spatially chirped microaxicon arrays

The principle of tunable needle beam dimensions was explored by programming arrays of axicons of various size into the SLM. Radii ranging from 70 µm to 170 µm were used whereas the corresponding phase mask in *Fig. 4.3.3(a)* additionally reflects the spatial arrangement. 'Laser A' served as a pulsed light source delivering pulses around 12 fs (at 800 nm center wavelength). A pulse duration of about 20 fs was measured after passing the SLM. *Figs. 4.3.3(b,c)* show the intensity distribution at two representative distances z = 2 mm and z = 7 mm. The intensity profiles appear to be fringe-less independently on the axicon size as expected. For each column, needle beams of various beam diameters (covering values from 60 µm to 150 µm at $1/e^2$) and depths of field are generated whereas the position of maximum intensity appears to be shifted along the optical axis. Hence, the finite nondiffracting zones were manipulated by adapting only the axicon size concerning to their beam structure including diameter, depth and axial location as well.

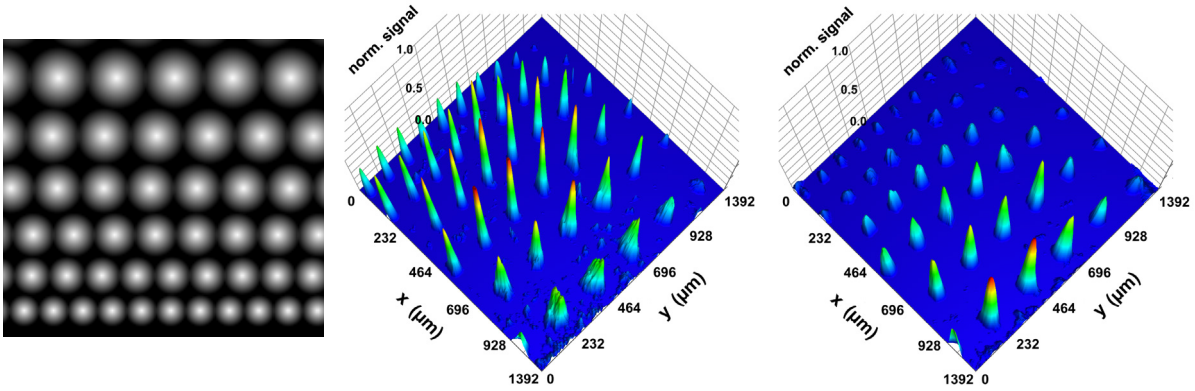

Fig. 4.3.3 Array of locally adapted needle beams with a global phase envelope function (part). The beams were generated by programming discretized phase maps in a PAN-type LCoS-SLM via variable gray value maps: **(a)** Thus, axicons of variable diameter and angle were programmed (left: 1.7 x 1.7 mm^2 field of view). **(b)** Intensity plot at an axial distance of 2 mm (middle), **(c)** intensity distribution dimensions at an axial distance of 7 mm (right) from the array center.

4.3.2 Highly localized wave packets

More complex HLWs were generated, measured and analyzed by programming modified axicon phase distributions into the SLM as reproduced in *Fig. 4.3.4* and by using shorter pulses ('Laser B'). In this scheme, the columns represent the length of the axicons whereas the rows define the expansion of the central dark spot. The shapes were manipulated by the size and angle of the inner and outer axicon.

Table 4.3.1 Parameters for generalized axicon phase masks and intensity distribution of frequency-converted (SHG at 400 nm) HLWs measured at distance of z = 80 mm (n,m indicates the matrix elements).

Axicon parameters							Needle beam properties		
(n, m)	$2r_i/R$	R_l (µm)	R_s (µm)	α_i (mrad)	α_a (mrad)	E_a	d (µm)	E_n	τ_p (fs)
(1,1)	-	430	430	-	2.0	1.0	55	1.0	6.5
(1,2)	-	1420	430	-	1.8	3.3	45	6.6	6.5
(1,3)	-	2620	430	-	1.8	6.1	45	12.0	6.5
(2,1)	0.5	600	600	4.5	2.2	1.0	65	1.0	6.5
(2,2)	0.5	1070	570	4.5	2.2	1.9	85	2.6	6.6
(2,3)	0.5	1500	630	4.5	2.2	2.4	85	4.0	6.4
(3,1)	1.0	620	620	2.0	2.0	1.0	55	1.0	6.5
(3,2)	1.0	1120	680	2.0	2.0	1.6	55	2.1	6.5
(3,3)	1.0	1460	680	2.0	2.0	2.1	60	2.7	6.5

Therefore, in *Tab. 4.3.1* the most important parameters are summarized: Inner radius r_i, total radius R, axicon dimensions R_l and R_s parallel to the long and short axis, inner and outer axicon angle α_i and α_a, HLW's structural width d as the standard deviation, ratio of the long axis to cross axis for the axicons and needle beams E_a and E_n, pulse duration τ_p. The second

order autocorrelation traces and intensity distributions were simultaneously recorded by an EMCCD-camera. Therefore, the central wavelength of the recorded and spectrally integrated light pulses was λ_0 = 400 nm due to the frequency-doubling step.

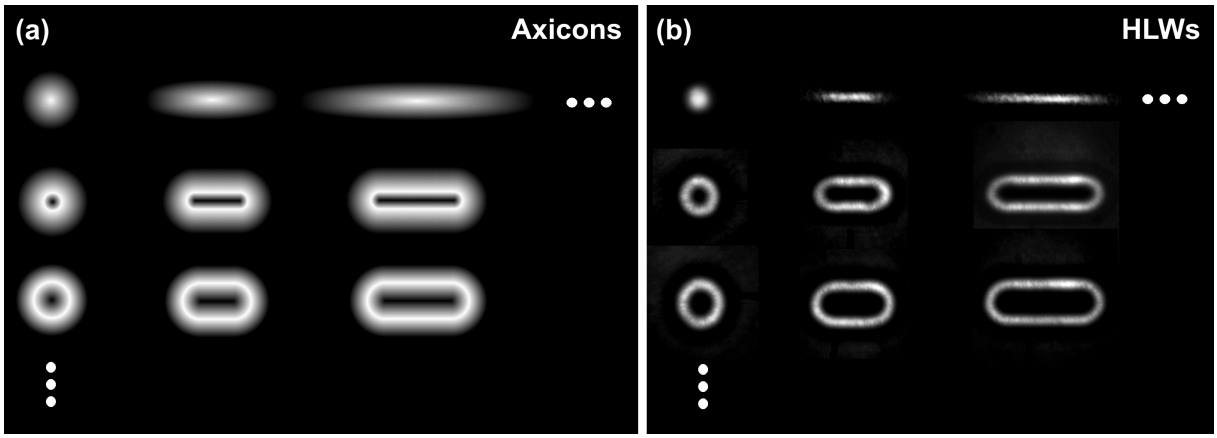

Fig. 4.3.4 Basic scheme of generalized highly localized wave packets: **(a)** Phase mask of conical-like and toroidal-like axicon structures as building blocks for more complex distributions, **(b)** corresponding intensity distribution (after frequency-doubling) measured at a distance of z = 80 mm. The parameters of the axicons within the n x m matrix are summarized in *Tab. 4.3.1*.

The resulting intensity distribution and pulse duration were measured at the same axial distance for all HLWs. The optimal depth of field, i.e. the case of maximum intensity within the Bessel zone, was adapted to the detector distance of z = 80 mm for each HLW individually. Although the spatial scalability of needle beams was exploited here, it must be assumed that the transformation did not affect the spatiotemporal properties but just the dimensions of the HLWs (as can be verified in *Tab. 4.3.1*). Thus, the propagation properties of only a selected HLW is outlined in detail with respect to the temporal and spatial domain. Specifically, the HLW generated with the axicon (3,2) is used as a representative example of the extraordinary types of nondiffracting and nondispersing wave packets with non-rotational spatial distributions.

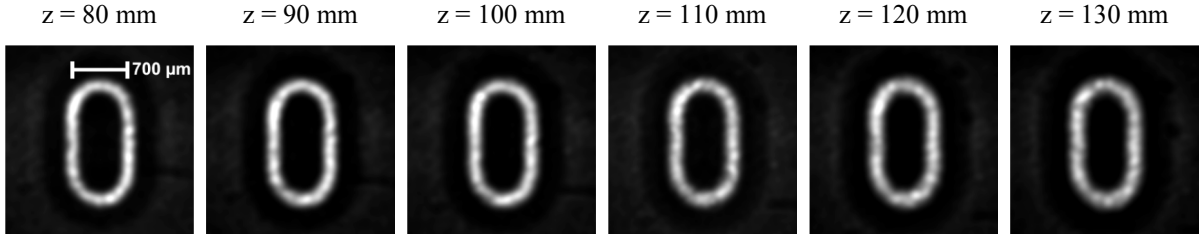

Fig. 4.3.5 Measured spatial intensity distribution of a selected complex HLW showing a nondiffracting propagation behavior over a distance of at least 50 mm. The field of view is about 2.7 x 2.7 mm^2.

The sub-type of modified Bessel beams behaves nondiffracting within the measured range as shown in *Fig. 4.3.5*. The ‘stadium’-like wave packet keeps its spatial expansion in vertical

and horizontal direction (D_v = 1400 µm, D_h = 700 µm) and its ring width (d = 100 µm) over the entire observed range and beyond. Fluctuations in the intensity are due to the roughness of the SHG-crystal and spectral filters within the beam path of the setup. The radius of curvature measured from two focal points of the stadium is the same as it was originally programmed and were specified to be roughly 300 µm.

Measurements of the pulse duration at selected axial distances (within the range of the interference zone) reveal a nondispersing propagation of the highly localized wave packet. The time-dependent electric field distribution is visualized in *Fig. 4.3.6(a)* by a three-dimensional representative reconstruction based on the measured spatially-resolved autocorrelation data. The pulse duration at a selected single point was measured to be in the range of τ_p = 6.5 fs ± 0.2 fs. The 2nd order autocorrelation traces in *Fig. 4.3.6(b)* are representative for all generated HLWs as shown above.

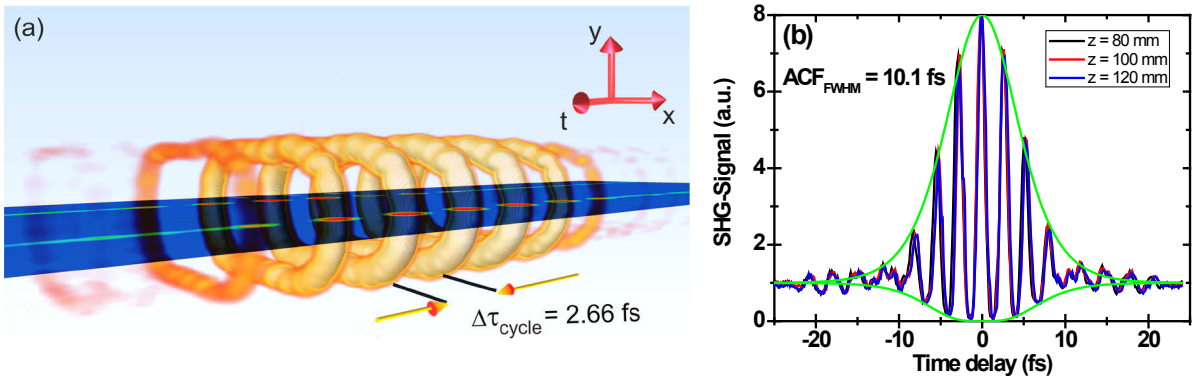

Fig. 4.3.6 Spatiotemporal measurement of the 2nd order autocorrelation trace of the HLW (3,2) at selected axial distances: **(a)** 3D-dimensional representation of the corresponding spatial electric field distribution approximated from autocorrelation data (z = 80 mm) with the scales given in *Fig. 4.3.5*, **(b)** autocorrelation traces at a single point (8x8 µm^2) but various distances (black line z = 80 mm, red line: z = 100 mm, blue line: z = 120 mm). The full-width-at-half-maximum width of the trace at each axial position implies a pulse duration τ_p = 6.5 fs assuming a sech^2-function.

On the one hand, a minimum number of axicon zones and minimum conical angles have to be chosen to introduce minimum temporal distortions at very short pulse durations. On the other hand, far more complex patterns can be implemented comprising the usage of modified axicon profiles and combination. The final pulse structures and propagation patterns are the result of the spatiotemporal interference of contributions from all local conical areas. This concept is comparable to the holographic reconstruction of objects where wave vectors of different amplitude and phase are superimposed and each wave vector is related to another degree of freedom. For instance, a particular light distribution is obtained when a number of needle beams (sub-type of an HLB) are spatially arranged in systematic order. This is the main concern of the next paragraph. In those cases the entire complex light beams propagate without spreading in space and time due to the nonspreading properties of the sub-beams.

4.4 Nondiffracting complex patterns composed of multiple HLWs

The following concept supports the decomposition of complex images into constituting building blocks of simple spatial geometries (lines, circles, rings, etc.) as proposed in the chapter before. Then, each part of a discretized input image includes an independent sub-beam of nondiffracting propagation behavior. The entire image pattern is then of course also nondiffracting in space and nondispersing in time over a finite range. For the first time, nonspreading patterns were shaped from near-infrared pulses as short as 6.5 fs. Adaptive arrays of local phase axicons allow the generation of different kinds of nondiffracting beams or patterns at extreme parameters: (i) extremely short (few-cycle range) pulse durations (ii) ultrabroad spectral bandwidths, and (iii) large angles of incidence. A further advantage is the achievement of relatively low cross-talk effects over considerable long distances. This enables a stable propagation of complex "flying images" in free space with a high recognizability over a large depth of field.

The complete arrangement was designed to satisfy the requirements of a low-dispersion setup by using double-chirped mirrors as introduced in the other experiments. Defined simple and complex beam patterns were generated by phase maps composed of individual local phase axicons of variable size, arrangement and conical angle. With this concept, shapes like simple imprints or images (decomposed into simple geometrical shapes) can be mimicked.

4.4.1 Nondiffracting image patterns with needle beams

Since the arrangement of needle beams is not strictly limited to hexagonal or other periodic structures, selected needle beams were switched off (on), and non-periodically arranged. Following this approach, a physical realization of Saari's proposal of spatiotemporally nondiffracting "flying images" was realized on a few-femtosecond time scale [Saa96]. For demonstration purposes, a well-recognizable pattern (letter "E") was inscribed into the beam intensity profile of an ultrashort pulses laser source (‘Laser A’). Fifteen identical axicons were necessary to form a letter “E”. For this, the appropriately arranged Gaussian-like axicons of the radii R = 250 µm with an averaged main conical angle of θ = 5.4 mrad were programmed into the LCoS-SLM. The phase profile was chosen to exhibit a soft decrease at the rim (no sharp edges) to prevent unwanted diffraction effects (phase apodization) as shown in *Fig. 4.4.1(a)*. Simultaneously, this fading leads to an axial shift of the distance where neighboring sub-beams start to overlap, resulting in an extended propagation depth and a reduction of cross-talk. The axicons were merged together in such a way that the final

horizontal and vertical period were about 320 µm whereby a special overlapping algorithm was introduced to preserve the gray level distribution of the individual axicons (without obscuring each other). Specifically, each axicon gray value map was corrected depending on distance and diameter of the surrounding axicons. The linear part of the axicon was set between a radius of R = 40 µm and R = 140 µm. It implies a resulting nondiffracting zone ranging from z = 7.5 mm and z = 26 mm.

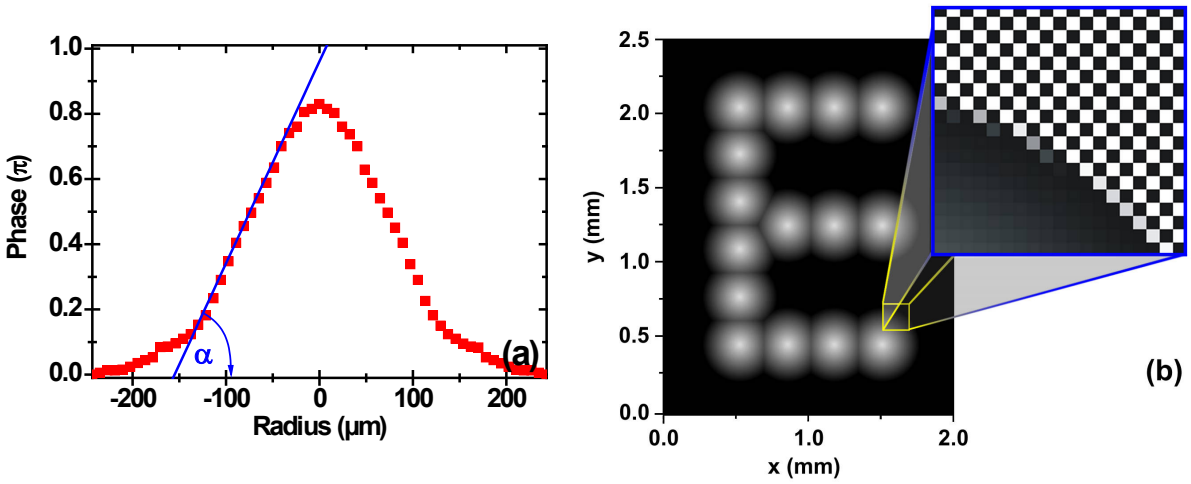

Fig. 4.4.1 Concept of flying images demonstrated by programming the letter "E": **(a)** Real phase distribution of the programmed axicon with a main axicon base angle of α = 2.7 mrad, **(b)** Gray scale (corresponds to a certain phase retardance) map of fifteen elements programmed in the LCoS-SLM (diameter: 62 pixels, period: 40 pixels). The inset indicates the checkered phase pattern programmed in the gaps for contrast improvement (period: 2 pixels).

To study the propagation conditions including spatiospectral and spatiotemporal contrast ratio and cross-talk, three basic geometrical arrangements of gray value addressed phase axicons were realized for the following situations: (i) programming single needle beams (to totally exclude any cross talk effects), (ii) programming complex ray patterns consisting of reconfigurable arrays of needle beams, and (iii) arrays like (ii) but with an additional background management. In the third case, a checkered phase pattern acting as a diffractive cross grating was programmed in the spaces between the programmed binary phase axicons. The pixel pattern between the axicons was chosen to be unstructured (i.e. with homogeneous phase) in the first and second case. The highly diffractive background pattern was used to study the influence of surrounding high-spatial-frequency textures and, in particular, to separate unshaped light from the main propagation direction of the shaped sub-beams. The geometrical arrangement is illustrated in *Fig. 4.4.1(b)* with the addition that the inset is attributed to the diffractive checkered gray value background patterns.

A central aspect of the propagation analysis is the axial evolution of the radial shape function. Its mathematical description should be compact and selective but keeping track of significant

physical information. Therefore, well-known tools of higher order statistical moments were applied. In particular, the fourth order statistical moment K (kurtosis, see chapter 4.1) of central cuts through measured profiles in transversal direction was calculated to extract specific information about peakedness (positive value) or flatness (negative value). This enables to evaluate also non-uniform shapes with high sensitivity. The propagation dependent kurtosis of the transversal shape functions in *Fig. 4.4.2(a)* is nearly identical for single (blue curve) and arrayed needle beams (green curve) if no additional grating is programmed in the dead space. However, the presence of such a phase structure (black curve) leads to significant deviations over most parts but a convergence between z = 38 and 50 mm. The abrupt changes of the kurtosis from positive to negative values is attributed to the peculiarities of the formation of realistic broadband Bessel-like beams of finite energy in contrast to idealized Bessel beams. Furthermore, contributions from the inner part of the illuminated axicon, where the axicon angles are distinctly smaller, additionally disturb the beam intensity profile and leads to a non-Bessel-like central lobe.

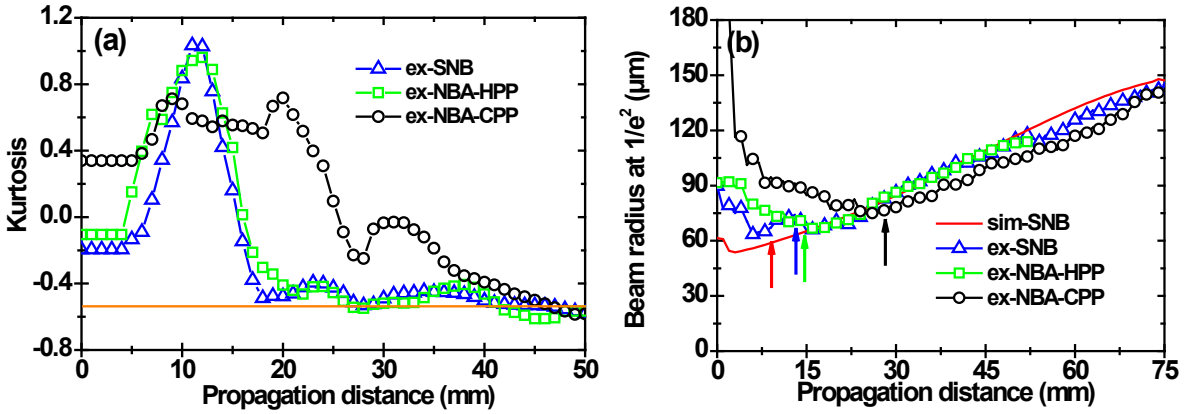

Fig. 4.4.2 Beam propagation parameter in dependence on the axial distance z: **(a)** Measured kurtosis of the radial shape. The kurtosis for an ideal squared Bessel function is marked with the orange horizontal line. **(b)** Averaged beam radii as a function of the distance measured for all three types of beams in comparison to the simulated evolution of a solitary needle beam. The arrows indicate the positions of maximum intensity (colors of the related curves). The abbreviations used are: solitary needle beams (ex-SNB), simulated solitary needle beam (sim-SNB), needle beam array with homogeneous phase pattern between axicons (ex-NBA-HPP), and array with checkered phase pattern between axicons (ex-NBA-CPP).

The deviations from the kurtosis value of –0.53 of the central maximum of an ideal squared mathematical Bessel function J_0^2 are a quantitative measure of the deviation from the conicity of the generating wave. On the basis of this criterion, the range between z = 19 mm and z = 50 mm is well approximated to the central envelope function of the squared Bessel function J_0^2. This is valid for both solitary needle beam and sub-beams of needle beam arrays with homogeneous background. The radius at the waist of the needle beam (z = 19 mm) was

found to be around w = 70 µm. In the case of a checkered phase pattern in the dead space between the axicons, J_0^2 is approximated from larger distances (about z = 38 mm).

Tab. 4.4.1 Propagation parameters of sub-beams of different types of beam arrays compared to a solitary needle beam.

Pattern	Beam waist w_0 (µm)	Axial position z_1 (mm)	Beam radius at $2^{½}w_0$ (µm)	Position z_2 (mm)	Aspect ratio z_2/w_0
Solitary beam	66.8	12.6	94.5	35.0	520
Array (homogeneous phase pattern between axicons)	68.9	16.0	97.5	39.0	560
Array (checkered phase pattern between axicons)	77.3	24.8	109.3	52.0	670

The comparison of relevant beam parameters in *Tab. 4.4.1* indicates no significant changes of the propagation properties on the phase structure between the intermediate gaps of the letter 'E'. This was proved by switching from a solitary needle beam to an array of needle beams with non-textured background. The position of the beam waists, however, was found to be slightly shifted towards the CCD detector if the checkered phase pattern was applied. Axially-dependent beam radii extracted from measured and simulated data are shown in *Fig. 4.4.2(b)*.

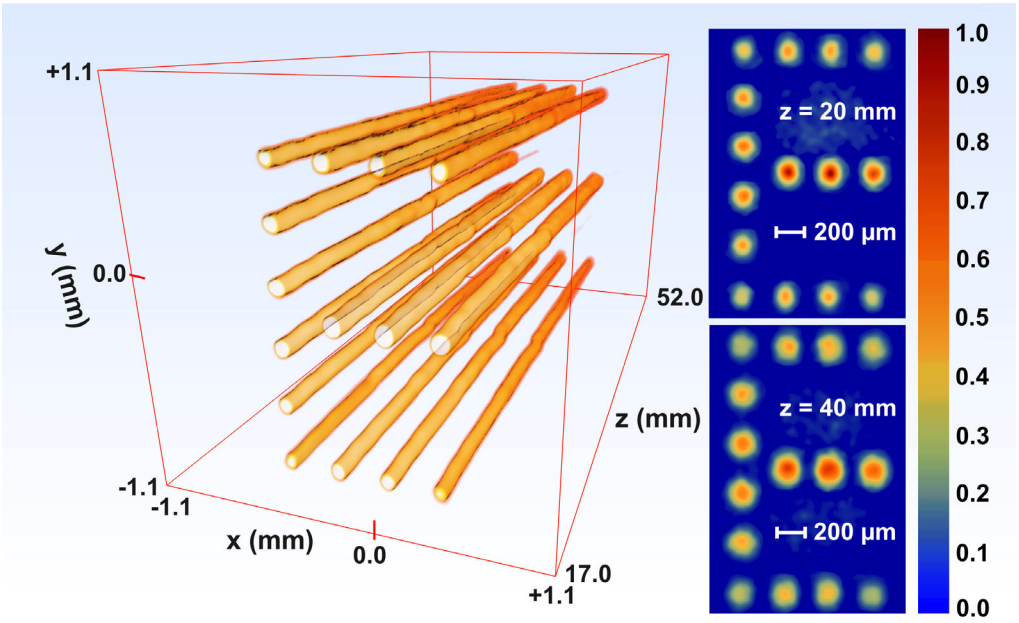

Fig. 4.4.3 From tomographic data this 3D representation of the "E" was retrieved. The insets show the flying image at z = 20 mm and z = 40 mm, respectively. In both CCD-recorded images an additional background correction was applied by introducing a phase-pattern in the gaps between the axicons. The pattern dimensions (related to the centers of sub-beams) here are Δx = 972 µm and Δy = 1620 µm.

Each waist radius was determined by sectional fitting the progressing curve by a 3rd order polynomial. In the case of a non-uniform gap structure, the beam radius increased

significantly in the proximity of the SLM where a transient superposition of needle beam and the radiation diffracted at the checkered phase area is expected. For $z > 25$ mm, the axial dependence of the radius was found to be nearly identical again for all curves including the simulation. That implies that the cross-talk between adjacent optical channels remains low over large propagation distances.

The "flying image" is visualized in *Fig. 4.4.3* rendered by a tomography-based software analysis for 3D-reconstrunction. The image is reconstructed over large depth of field. The diameter of individual sub-beams increases from $w = 140$ µm to $w = 220$ µm, containing "light sheets" (spatially coherent few-cycle pulses) propagating along this path without temporal or spatial broadening. The pulse duration of a selected needle beam within the structure was found to be around $\tau = 20$ fs, i.e., slightly more than the duration of the input pulse. The spectral properties of such needle beams were also measured. The results are compared with the theory in *Fig. 4.4.4* by taking the measured spectrum as initial values for the simulation, which shows a very good agreement.

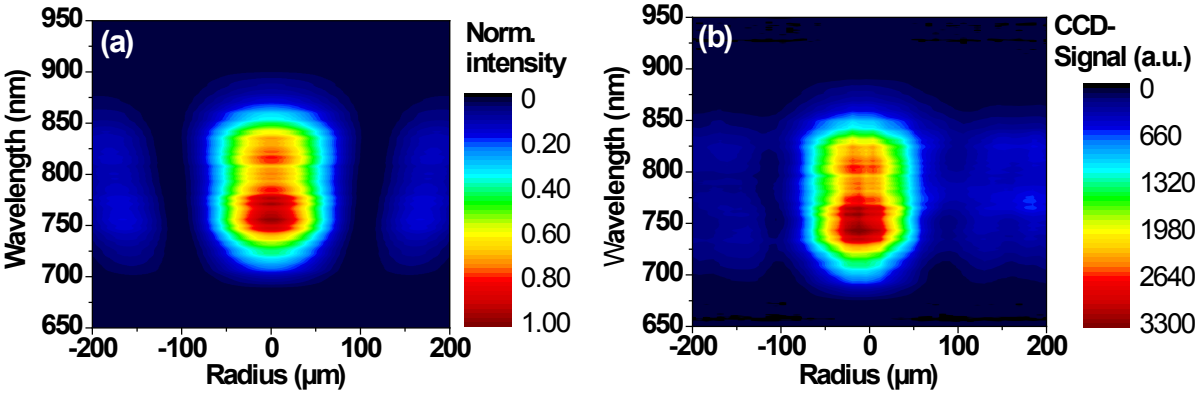

Fig. 4.4.4 Theoretical and measured spatially resolved optical spectrum of a needle beam as used for the construction of the "flying image": **(b)** Simulation of the spatiospectral distribution of a needle beam with weak fringes based on input spectrum of a 'Laser A', **(b)** measured spatiospectral behavior of selected a needle beam of the same size generated with an ultraflat axicon programmed into an SLM (same parameter as in the simulation).

4.4.2 Decomposition of an image into HLWs

Another example of a phase (gray level) distribution and the resulting light concentration properties are illustrated in *Fig. 4.4.5*. The axicon radius was set to be around 60 µm, so that the main axicon base angle achieves values about $\alpha = 6.7$ mrad (conical angle: $\theta = 13.4$ mrad), except the axicons forming the outer frame of the logo. The nearly undistorted propagation of the ultrashort pulsed pattern (logo of MBI) of only $\tau = 6.5$ fs with relatively small feature size is well recognized, however, it is strongly distorted at distances > 5 mm. Here, the structure

width (at $1/e^2$) of the letter 'M' is about d = 35 µm at z = 1 mm and d = 62 µm at z = 5 mm. This gives rise to an extremely large aspect ratio of z/w > 200 (nondiffracting length z to beam radius w) as a measure for the depth of the focal zone. The high image resolution was chosen to ensure that the whole logo fits within the diameter of about 2.5 mm of the input beam. The cross sections show that cross-talk effects between neighboring axicon structures lead to unwanted interferences disturbing the quality of the image.

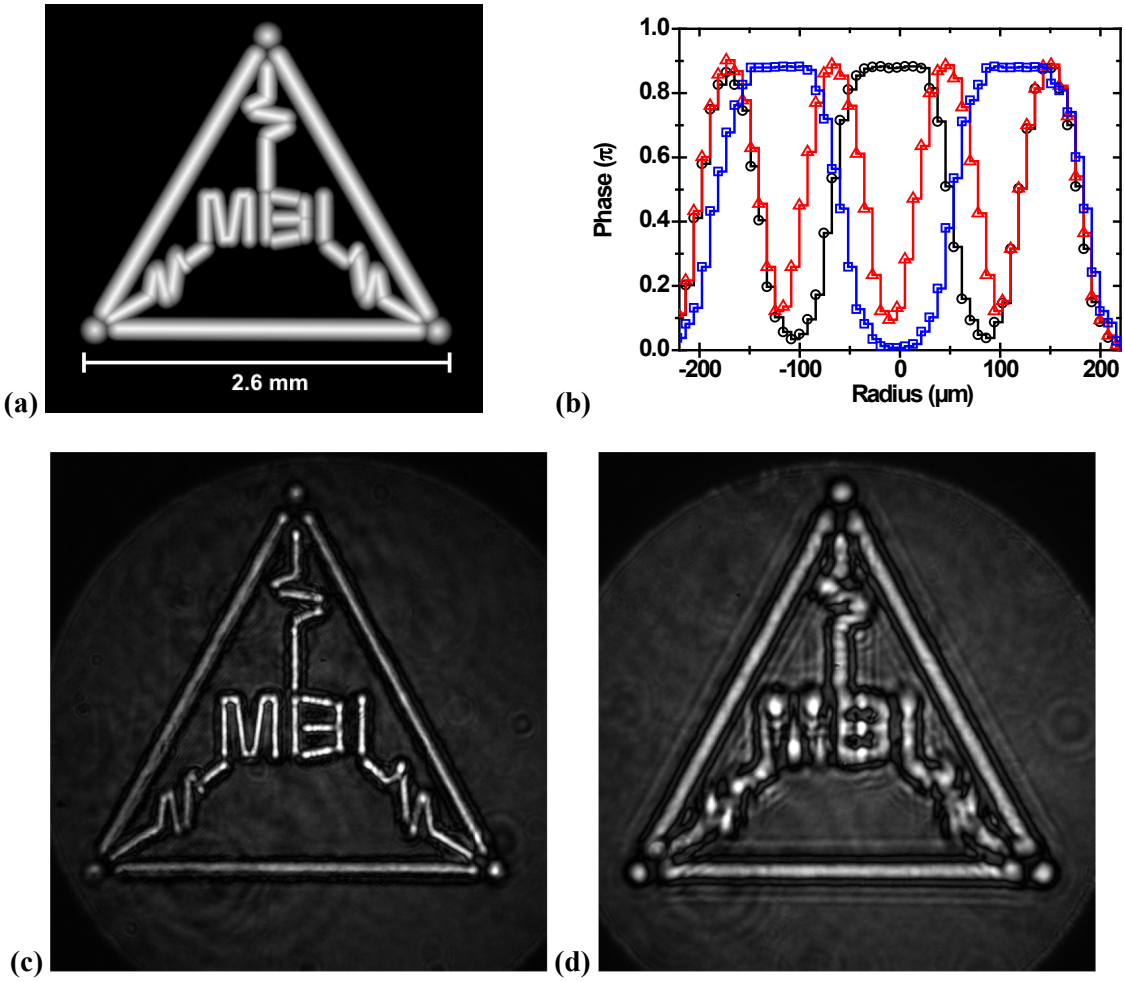

Fig. 4.4.5 The MBI-Logo as an example of an ultrahort pulsed complex light field showing a nondiffracting propagation behavior: **(a)** Particular phase pattern (gray level representation) encoded into the SLM, **(b)** phase profile cuts through the letter 'M' at three selected positions (bottom horizontal cross-cut: black circles, middle: red triangles, top: blue squares). The intensity distribution was recorded at **(c)** z = 1 mm, and **(d)** z = 10 mm;

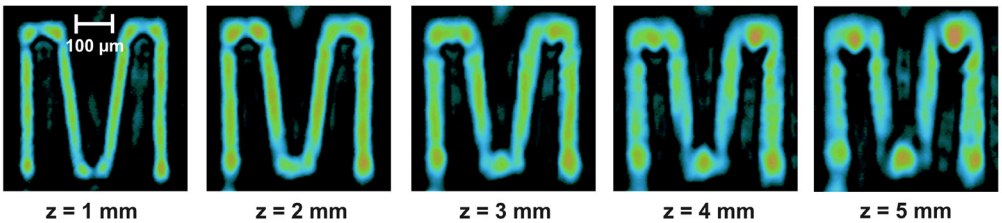

Fig. 4.4.6 Magnified section of the MBI logo showing the letter 'M' at distances from z = 1 mm to z = 5 mm. The field of view is here 360 x 360 µm^2.

4.5 Two-dimensional spatially resolved nonlinear autocorrelation

As reported, HLWs have specific advantages to Gaussian beams, especially when microscopic sized, few-cycle pulsed beams have to be generated without affecting the temporal properties. This gives rise to a plenty of applications like a spatially resolved 2nd order autocorrelation to measure the temporal properties of pulsed lasers.

4.5.1 Autocorrelation of a needle beam

Before a spatially resolved characterization of pulsed laser beam is performed it is essential to ensure that only negligible temporal distortions are introduced by the setup. That means, a pulse broadening by material dispersion (e.g. by the cover glass of the SLM) should be reversible without much effort (mainly quadratic phase: < 100 fs^2). The capability of the setup of a high-fidelity 2nd FRAC measurement was tested at different pulse durations and axicon sizes. In both autocorrelation measurements, needle beams of specific characteristics were generated due to the usage of different types of LCoS-SLM within the particular setup. In the first case, the axicon shape was programmed to be a Gaussian-like function (smoothed profile) as it was already shown in *Fig. 4.4.1(a)* whereas in the second case the profile was of pure conical shape. The axicon radii were set to be R = 300 µm (main θ = 4.0 mrad, outer part θ = 1.3 mrad) and R = 180 µm (θ = 4.0 mrad) whereas the axicon pitch was p = 560 µm and p = 340 µm, respectively. In both cases, a slight overlap between the axicons has been introduced.

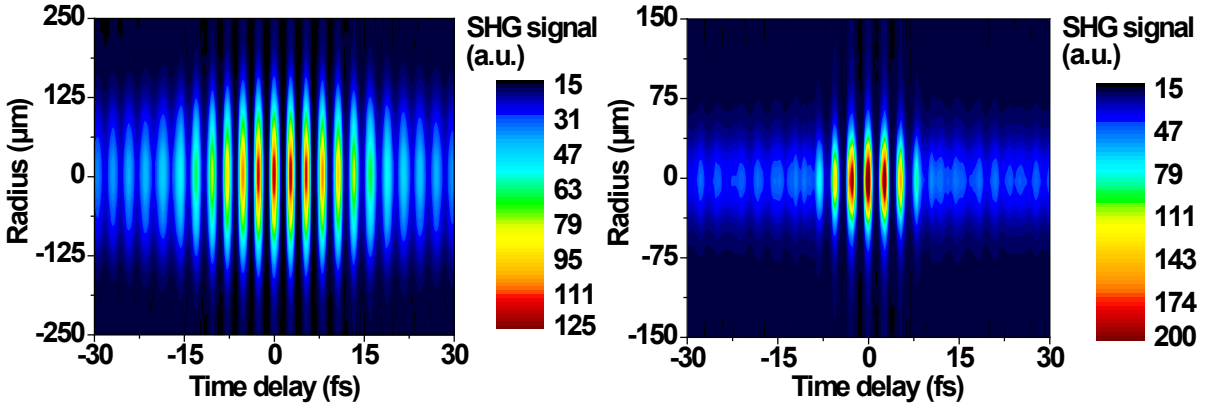

Fig. 4.5.1 Comparison of two second order autocorrelation traces (azimuthal averaged) of pulsed needle beams with pulse durations of 15 fs (left) and 6.5 fs (right).

The two pulsed needle beams were extracted from an array, whereas the generation was supported by the two above mentioned modelocked Ti:sapphire laser systems providing input

pulses in the range of 13.0 fs (‘Laser A’) and 6.5 fs (‘Laser B’). The spatial intensity distribution of both nondiffracting needle beams of micrometer dimensions were recorded by an EMCCD-camera (Andor iXon 885). The plane of interest, i.e. the axial positions of the SHG-crystal at z_A = 130 mm and z_B = 40 mm, were imaged by a microscopic objective. Beam widths ($1/e^2$) in the range of about w_A = 140 µm and w_B = 60 µm are retrieved at a central wavelength of λ = 400 nm based on the digital photographs. Pulse durations (FWHM) of τ_A = 20 fs and τ_B = 26 fs were measured without compensating the introduced positive quadratic phase introduced by the material dispersion of the cover glass. Therefore, a single bounce on a pair of double chirped mirrors was inserted in the setup to achieve again pulse durations close to the input values. The resulting radially dependent autocorrelation traces of the recompressed needle beam pulses are displayed in *Fig. 4.5.1*. Two phenomena are clearly visible: (i) the trace width is constant over the radius and (ii) the temporal localization increases towards shorter pulses. Even at radial positions with lower signal, an unaltered pulse duration is found. Albeit, in the outmost regions the signal-to-noise ratio is decreased significantly, resulting in an increased inaccuracy of the pulse duration data. For the corresponding laser system a pulse length of 15 fs and 6.5 fs can be calculated. It should be noted that for the retrieval of the pulse duration for the longer pulses a Gaussian pulse shape was assumed whereas for the shorter pulses a sech^2-function was the basis for the analysis.

4.5.2 Pulse duration map

Arrays of needle beams enable the spatial mapping of the pulse duration with a certain spatial resolution defined by the array period. Such a second harmonic spot array (at zero time delay) arranged in a rectangular grid is shown in *Fig. 4.5.2(a)*. Here, the same axicon phase profile was used as it was recently applied to 6.5 fs pulses as described.

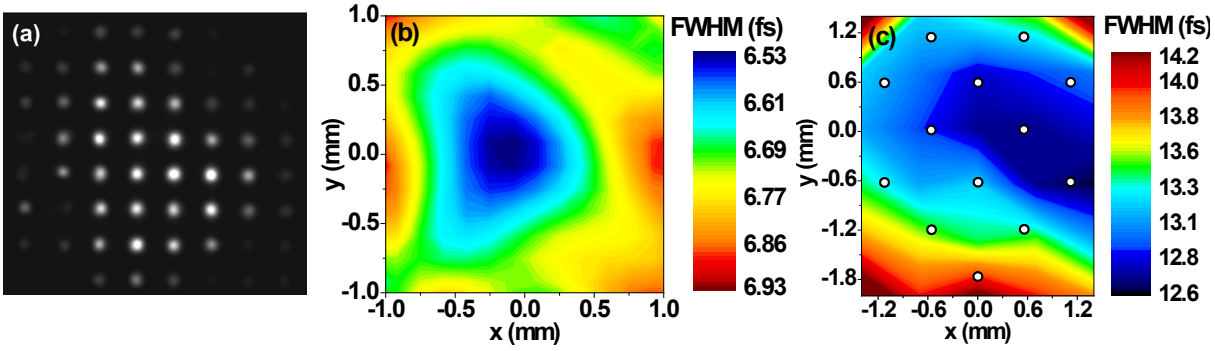

Fig. 4.5.2 Wavefront division for spatially resolved pulse diagnostics: **(a)** Second harmonic spot arrays for a two-dimensional autocorrelation measurement with a field of view of about 2.4 × 2.4 mm^2, **(b)** Retrieved pulse duration map of the Ti:sapphire ‘Laser B’ oscillator measured with needle beams. At the same time the zero position represents the peak intensity of the Gaussian beam envelope. **(c)** Measured pulse duration map of ‘Laser A’ where the white dots represent the measuring positions.

At the SHG-crystal plane (z = 40 mm) the needle beam width was about w = 200 µm. It was found that the pulse duration across the beam profile shows a spatial dependence (see *Fig.4.5.2(b)*) as it is typical for broadband ultrashort laser pulses. For the Venteon Pulse One PE ('Laser B') laser oscillator, the pulse duration at the center of the Gaussian beam distribution (point of highest intensity) is shorter than at the outer parts. A similar behavior was also measured for the other mode-locked Ti:sapphire laser oscillator as plotted in *Fig.4.5.2(c)*. When the two temporal maps are compared, it is apparent that the spatial fluctuations of the pulse duration are much more pronounced for the shorter pulses (relative to the averaged pulse duration).

4.5.3 Aberration induced distortions

At large angles of incidence, the induced spatial aberrations disturb the needle beam profile significantly. Autocorrelation traces were recorded under both conditions to observe, characterize and compare the spatiotemporal properties of aberration-corrected and -uncorrected needle beams. For that purpose, a huge angle of incidence was realized (≈ 43°) in the setup so that the needle beams were strongly perturbed by the spatial aberration of the axicon arrays (matrix period 720 µm, axicon radius R = 760 µm, conical angle θ = 2.3 mrad). The detected signals from the uncorrected pulse appear with spatiotemporal distortions (but in comparison to the spatial ones with less strength) as shown in *Fig. 4.5.3(a)*. A nearly undisturbed spatiotemporal autocorrelation trace (see *Fig. 4.5.3(b)*) was recorded for the corrected beam, neglecting the temporal fluctuation (stability of the interferometer) at a time delay of +3 fs. The spatial localization was clearly improved.

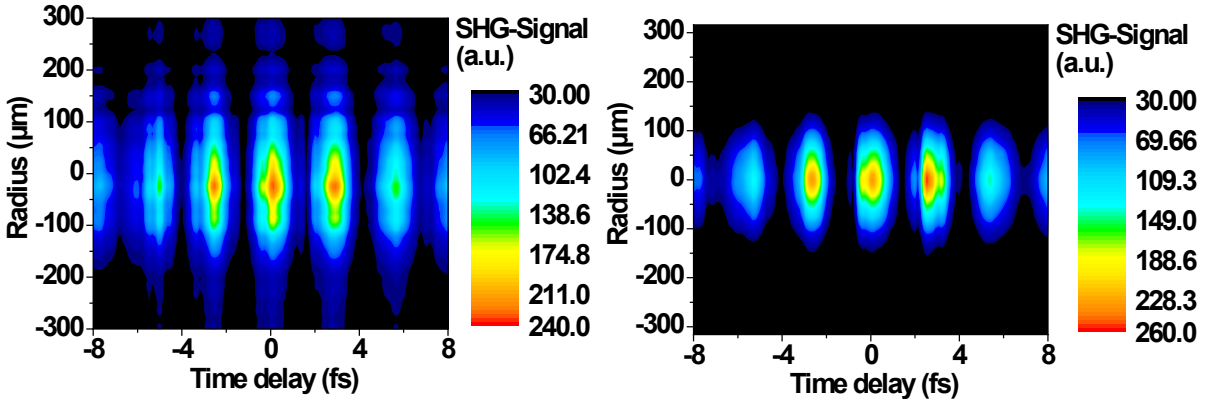

Fig. 4.5.3 Comparison of aberration-uncorrected (left) and –corrected (right) second order autocorrelation traces of a pulsed needle beam.

The best fits of the upper and lower envelope of the corrected and uncorrected autocorrelation traces extracted from a radial distance of r = 180 µm are plotted in *Fig. 4.5.4*. For the uncorrected case, the fit curve was a Gaussian function (*FWHM* = 10.5 fs) whereas in the corrected case, the closest approximation of the envelope was obtained by a sekans hyperbolicus function (*FWHM* = 9.8 fs). The temporal distortions induce an increase of the autocorrelation width of 0.7 fs which is significantly above the error bar (< 4 %) of typical autocorrelation measurements. A comparison with the original input pulse reveals that the fully aberration-corrected beam approximates the best representation of an undistorted measurement of the temporal properties. At the same time, the conclusion of this important result clarifies the necessity of a well-performed correction of the aberrations.

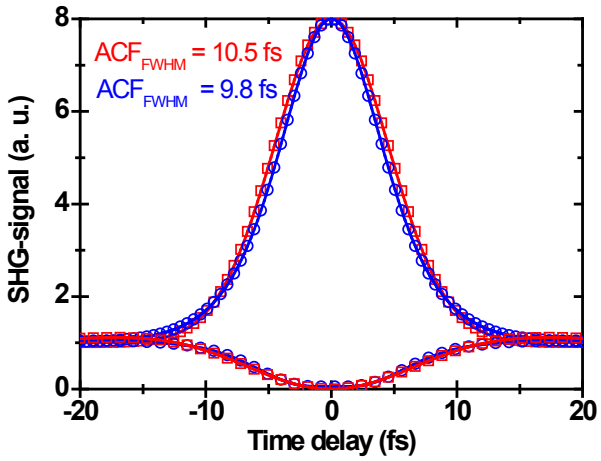

Fig. 4.5.4 Upper and lower envelope of the autocorrelation traces measured for the aberration-uncorrected (red open rectangles) and –corrected (blue open circles) needle beam

4.5.4 Temporal delay mapping

Arrays of autocorrelation traces contain more information about the pulse as simply the pulse duration at various positions. The results shown in *Fig. 4.5.2* further reveal relative phase delays across the beam profile to be analyzed. A wavefront curvature (see *Fig. 4.5.5*) is clearly identified without any need of a reference measurement (self-referency) as it is necessary for Shack-Hartmann sensors. It was found that the relative resolution was about 10 attoseconds, however the experimental fluctuations were much higher (standard deviation of around ± 20 as). In this experiment, the total wavefront represents a sum of the natural laser divergence and the lens effect of the LCoS-SLM surface.

The maximum delay in horizontal direction at an radius of 1 mm is approximately τ_d = 100 as (30 nm). The vertical and horizontal cuts through the temporal mapping data were fitted by quadratic regression curves (red line). This enables to calculate a radius of curvature. For the

direction perpendicular to the polarization of the E-field a wavefront curvature of about 33 m (without SLM: 4 m) is found. This curvature is much higher than in the other direction. Consequently, it implies that the SLM introduces a focusing effect on the light beam due to the convex shape of the its surface.

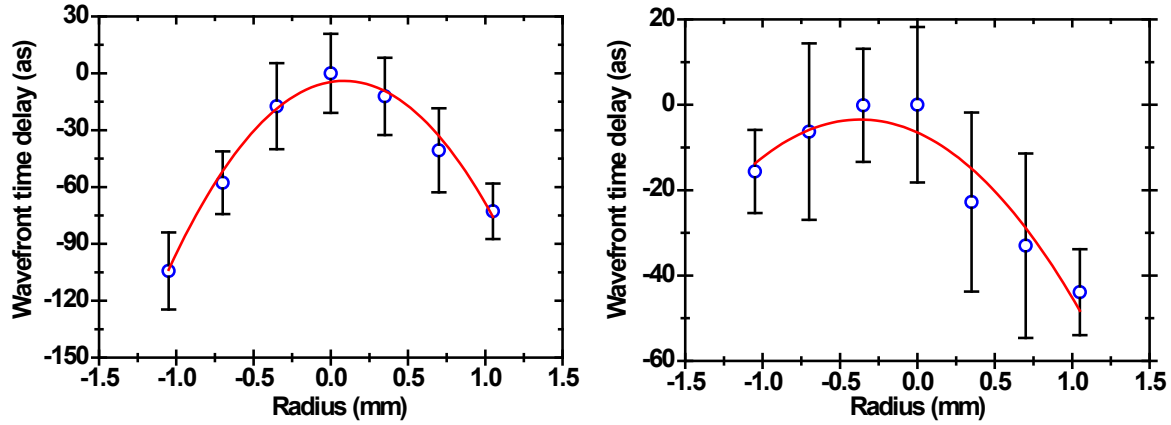

Fig. 4.5.5 Time delays in horizontal (left) and vertical (right) direction along central cuts through the cross section of the laser beam (including error bars). The basic data set was identical to that used in *Fig. 4.5.3* for the pulse duration map.

4.6 Application of HLWs for high fidelity wavefront sensors

Apart from the measurement of a pulse duration map, a matrix of sub-beams (needle, hollow, stadium-like beams, etc.) permits also the possibility to simultaneously measure the wavefront. A strict adherence to a constant matrix period, radial symmetric spots or uniform spot sizes is not mandatory in the case of adaptable HLWs. A programmable device has much more obvious possibilities in creating new schemes of Shack-Hartmann-based measurements. For instance, the encoding of certain spatial shapes into needle beams has the enormous advantage that the range of detectable radii of curvature is dramatically increased. However, the number of individually encoded needle beams must be sufficient and a reliable reference point with a negligible spot shift (zero shift) has to be determined. It is absolutely comprehensible that more complex Shack-Hartmann-patterns lead to more complex analyzing parameters or algorithms.

4.6.1 Wavefronts of small radius of curvature

To evaluate the sensitivity of this type of SHS in a first approximation, a test lens with a focal length of about 1 m focal length was used. It was found that the radius of curvature is around $\rho \approx 493$ mm which corresponds to a focal length of 1.09 m at a wavelength of $\lambda_0 = 800$ nm. To evaluate the wavefront properties by the SHS, the lens was placed shortly before the SLM (with an rectangular array period of $p = 340$ µm) and illuminated by an ultrashort pulsed laser beam with pulse durations of about $\tau = 6.5$ fs. The distance of the SLM to the CCD-detector matrix was chosen to be $z = 80$ mm. At this distance a good compromise between angular sensitivity and spatial resolution was found.

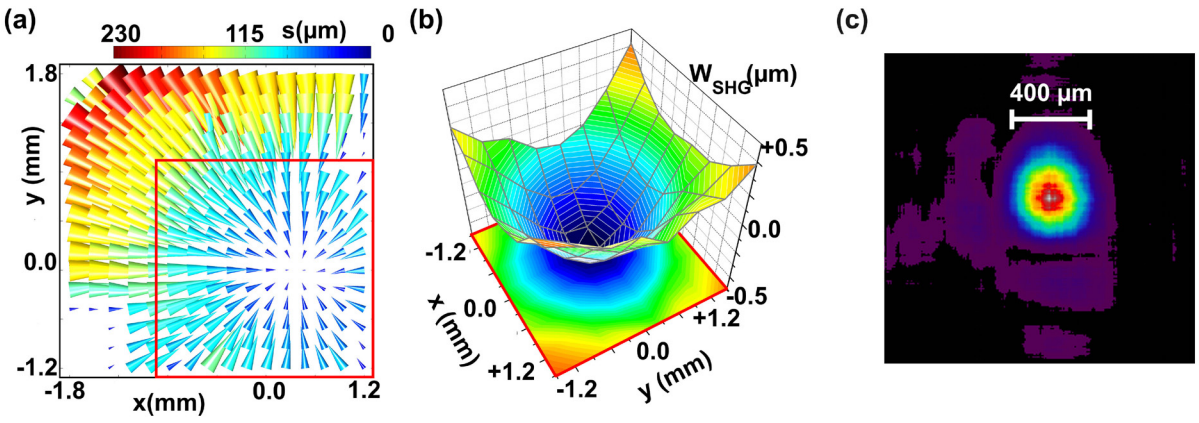

Fig. 4.6.1 Wavefront measurements of a $f = 1$ m refractive lens: **(a)** Vector plot of discretely measured elongations of the needle beams at an axial distance of $z = 80$ mm, **(b)** reconstructed SHG-wavefront after adaptive beam correction, **(c)** intensity profile retrieved from wavefront data at the focal plane ($f = 1100$ mm).

By a 10 x 10 matrix of needle beams (R = 85 µm) it was easy to detect the wavefront slope of this weakly focusing lens. The underlying data of the reference spot arrays were the same as used for the pulse duration map. Elongations of up to 230 µm within a field of view of 1.2 x 1.2 mm^2 show that the sensitivity is sufficient to detect even larger radii of curvature. The spatially dependent elongations are shown in *Fig 4.6.1(a)* as color-coded vector cones. Without much efforts, radii of curvature of up to ρ = 10 m are possible to detect with the use of these needle beams. After recalling some mathematical preliminaries introduced in the theory section, a corresponding wavefront is calculated as illustrated in *Fig 4.6.1(b)*. With the SHS, a laser divergence of θ = 1.72 mrad at 400 nm corresponding to θ = 2.43 mrad at 800 nm was measured. According to the input radius of w = 2.7 mm at the SLM position a focal length of f = 1.1 m can be calculated. This result was confirmed by an independent measurement with a white light interferometer. The retrieved spatial intensity distribution at the focal plane is shown in *Fig 4.6.1(c)*.

4.6.2 Wavefronts of large radius of curvature

Thereby, the wavefront detector should be able to capture strongly and weakly curved wavefronts simultaneously. For this purpose, an additional amplitude modulation is necessary to encode a distinctive feature into the intensity distribution of individual needle beams. The encoding scheme must ensure that the decoding algorithm is capable to capture the encrypted information. For a given number of distinguishable shapes there exists an optimal alternating 2D-arrangement to achieve the best performance. That is, specifically, the maximum spatial distance between two identical shapes within an orthogonal (or hexagonal) matrix. Obviously, this requirement cannot be fulfilled for the whole set of shapes, however, the number of violations may be minimized. The evaluation of such a deterministic algorithm is not trivial and would far surpass the actual aim of the thesis. In the simplest case, where only two distinct shapes have to be taken into account, the disposition of the elements would be chessboard-like. In following, this approach was extended to rotate every second encoded spot by a certain angle.

An example of such an encoding is shown in *Fig. 4.6.2(a)* where each beam, no matter which spatial shape (circular or dumbbell) was chosen, is nondiffracting and pulsed (< 10 fs). The spots can be retraced even outside their unit cells by means of the individual relative phase or angle of rotation as shown in *Fig 4.6.3*.

For demonstration purposes, a lens of 10 mm focal length was placed at 40 mm before the SLM. The encoding scheme was as follows: six cylindrical-like axicons were arranged around

a symmetric one and each of them rotated by 60° with respect to its neighbor. The long and short axis radii of the axicons were set to be R_l = 105 µm and R_s = 70 µm (also for the symmetric one), respectively. The array periods along both axes were p = 150 µm. The beam was hitting the SLM at a relatively large angle of incidence of about γ = 38° which required a slight correction of the induced aberration. A section of the resulting wavefront of the strongly divergent beam was then recorded with a CCD-camera at a distance of 5 mm (nondiffracting zone) from the SLM.

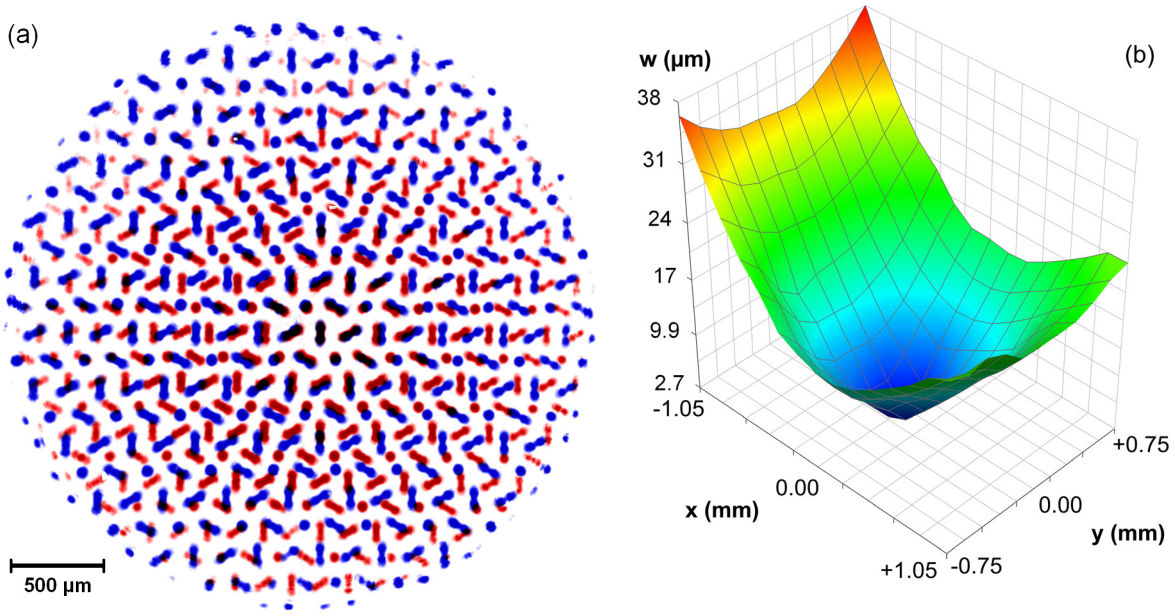

Fig. 4.6.2 High resolution wavefront sensing with single shot capability via shape-encoded nondiffracting beams arranged in a hexagonal array: **(a)** Overlaid hexagonal spot patterns measured with (blue) and without (red) the object (lens of 10 mm focal length). The picture shows the individual encoded needle beams of circular and dumbbell shapes within a field of view of about 3.1 x 3.1 mm^2. A negligible spot shift is indicated by black tones. **(b)** The retrieved wavefront is characterized by a relatively small radius of curvature indicated by large values of w.

From measured data, beam widths (at 1/e^2) of 150 µm and 60 µm can be retrieved confirming the asymmetric shape of the needle beams. The minimum line diameter of the dumbbell beams and the diameter of the circular beams were chosen to be the same. The spectrally integrated wavefront of a Ti:sapphire laser oscillator ('Laser B') after passing the lens is shown in *Fig. 4.6.2(b)*. The curvature of this wavefront reveals a half beam divergence angle of θ = 0.2 mrad which is in good approximation given by $\theta = D/f$ (where D represents the beam diameter at the lens plane and f the focal length of the lens).

The three distinct angles of 60°, 120° and 180° as used in the example are distinguishable by the radial intensity lobes as a function of the azimuthal angle. The method of rotating cuts and the subsequent analysis of the data reveals the required information of the particular spatial

positioning. This can be done on the basis of simple parameters like the beam width. In the given example, the strength of the oscillation amplitude of the beam width is consistently high as shown in *Fig. 4.6.3*.

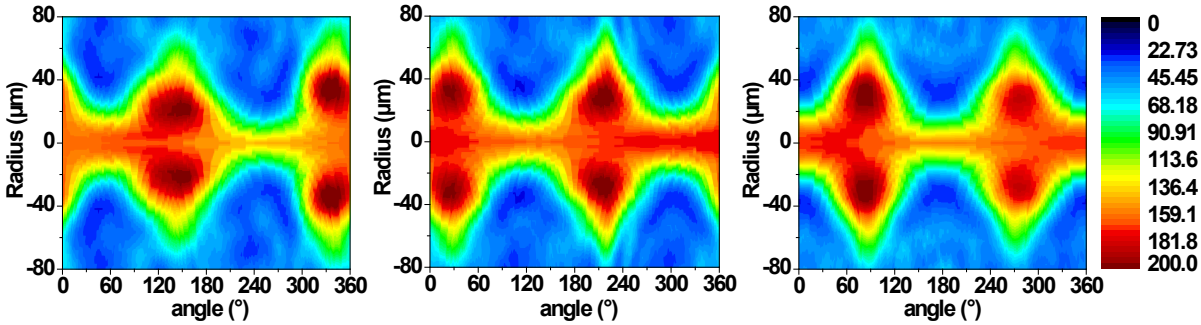

Fig. 4.6.3 Azimuthally dependent intensity profile of the needle beams generated via dumbbell-shaped axicons aligned at angles of –30° (right), +30° (middle) and +90° (left).

4.6.3 Resolution limits

Needle beam based Shack-Hartmann sensors enable to detect wavefront aberrations with a high sensitivity so that for example also weak rotationally tilted wavefronts are measurable. The essentiality of the high sensitivity is founded in huge lever arm (extended depth of focus) of the needle beams. The larger the distance between the generating microaxicons the higher is the deflection angle and the angular resolution. Furthermore, non-conical axicons have distinct advantages according to an improved separability even at large distances.

In the example, as shown in *Fig. 4.1.2(a)*, needle beams propagate over 300 mm without cross talk effects. The minimum deflection angle is then $5 \cdot 10^{-5}$ rad assuming a minimum detectable elongation of the needle beams of 16 µm (2 detector pixels) at a distance of 200 mm. The resolution can be significantly improved through sub-pixel interpolation algorithms. Note that this resolution is obtained without a microscope objective (telescope). The deflection angle may be further increased by inserting a beam expander. Then, the following proportionality is valid:

$$\theta_{defl} \propto \frac{D_{CCD}}{D_{SLM}}, \tag{65}$$

where D_{SLM} and D_{CCD} represent the beam diameters at the SLM and detector plane, respectively. Nevertheless, a large matrix detector area is necessary to detect the complete beam profile.

4.7 Few-cycle vortex pulses

4.7.1 Spiral gratings

In the following, pure binary diffractive axicons (spiral gratings) with a constant spatial frequency are introduced and their application for shaping few-cycle vortex pulses is demonstrated. It will be shown by corresponding experimental results that over a certain distance a high-contrast and temporally localized ultrashort vortex beam is generated. Two cases can be distinguished: (i) spiral grating axicons etched in a material, as was the case here, and (ii) spiral grating axicons programmed into an LCoS-SLM. In the second approach, the substrate can be simply replaced by a fully free-programmable device to create vortices with a higher flexibility.

Tab. 4.7.1 Properties of the spiral diffractive axicons

Label	Diameter (mm)	Phase levels	Height (nm)	Topol. charge ℓ	Period (µm)
SE1	2	2	800	2	9
SE2	2	4	1800	1	15

Both approaches are reliable methods to produce higher order Bessel beams with orbital angular momenta. In this chapter only the particular approach of a tailored grating design etched in a 3 mm thick SiO_2 substrate is discussed in detail. The $\ell = 2$ momentum beam is generated by a binary double spiral grating while that diffractive axicon producing an $\ell = 1$ momentum has a 4-step phase function in a single spiral structure. The radii of both elements were approximately 1 mm. Typical parameters like grating period and height were extracted (see *Tab. 4.7.1*) from white light interferometric data like in *Figs. 4.7.1(a,b)*.

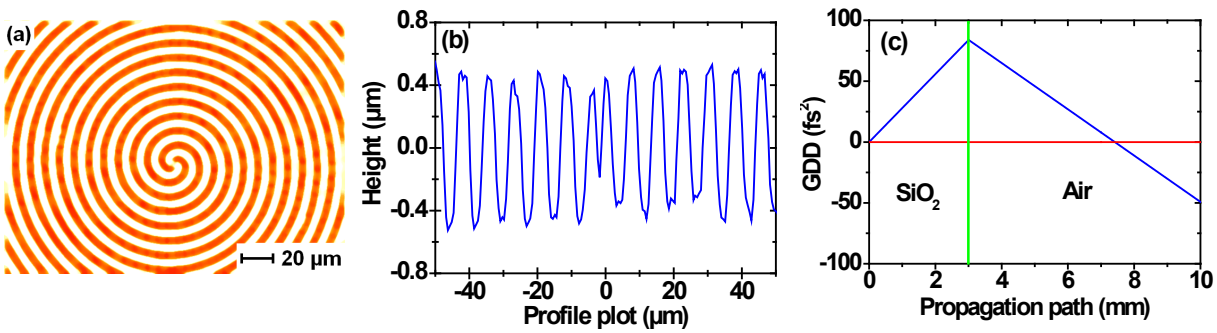

Fig. 4.7.1 White light interferometric measurements: **(a)** Profile map of a double spiral grating with a FOV of 220x140 µm^2, **(b)** the averaged (for different azimuthal angles) height profile of the diffractive axicon shows structure depth of around 800 nm which corresponds to a phase delay of 3π, **(c)** practically realized dispersion relations of a double spiraled grating.

For the SE1, an averaged profile height of 800 nm was measured. Because it is about a phase grating, the optical path and the resulting phase delay have to be considered. The phase delay is important with respect to the diffraction efficiency. A maximum efficiency is only obtained if the phase delay is exactly π, 3π, 5π, and so on. Since the refractive index of SiO_2 materials is about 1.5, the final optical path way is about 1200 nm (3π) as required. In the case of SE2, the beam path is more complicated because of the multi-step approach and the consequent prism effect (refractive beam deflection).

The dispersion curve for the SE1 element used for the autocorrelation experiments of the $\ell = 2$ vortex is plotted in *Fig. 4.7.1(c)*. The GRISM axicon was optimized to have a balanced dispersion at a distance of interest within the nondiffracting zone. A full compensation is theoretically achieved at a distance of $z = 7.5$ mm assuming a GDD at 800 nm for fused silica to be around 36.1 fs^2.

4.7.2 Temporal properties

The shortest available pulses of around 6.5 fs were used to test the compact, vortex-generating optical element. A measurement of the spatially integrated autocorrelation close to this value at $z = 8$ mm confirms that the pulse duration is as short as expected (see dispersion curve), around $\tau_p = 8.3$ fs ± 0.3 fs. Both traces for the initial Gaussian pulse and final vortex pulse are plotted In *Fig 4.7.2(a)*. A similar pulse duration is assumed for the $\ell = 1$ vortex.

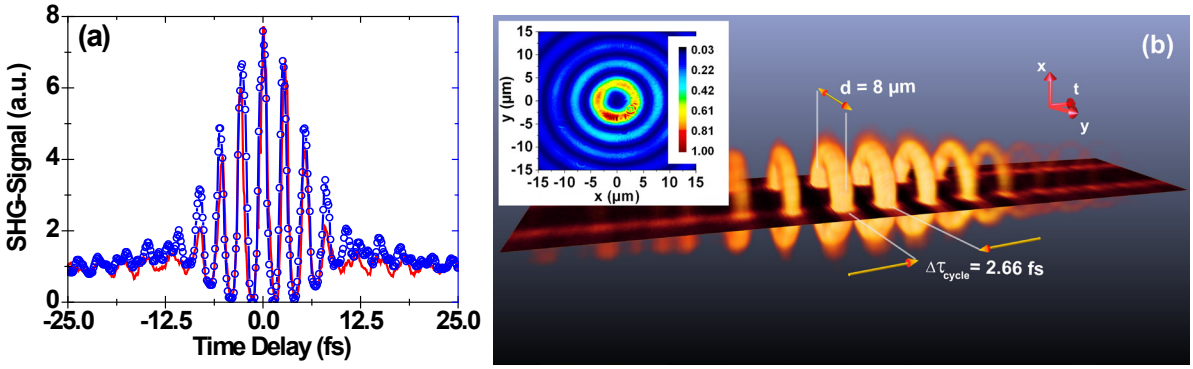

Fig. 4.7.2 Temporal behavior of a 8.3 fs vortex beam with a topological charge of $\ell = 2$ at a distance of $z = 8$ mm: **(a)** Autocorrelation traces of the non-twisted (red solid line) and twisted beam (blue open circles), **(b)** visualization of the spatially-resolved autocorrelation trace. The amplitudes of the autocorrelation trace in (b) are encoded in the brightness and the ring thickness of the ring pattern. The inset reflects the light distribution of the fundamental vortex pulse ($\lambda = 800$ nm) measured with a CCD camera.

A residual temporal chirp has broadened the pulse slightly (shorter pulses are possible by compensating the dispersion). Nevertheless, this represents one of the shortest optical vortices reported in the literature. The fully recorded spatially resolved autocorrelation trace is visualized in *Fig. 4.7.2(b)*, showing uniform pulse duration over the beam radius. Here, the

amplitudes of the trace were encoded in brightness and ring thickness. For example, the brightest and thickest ring corresponds to the maximum amplitude of the autocorrelation function at zero time delay. Note that the weak vortex rings were not resolved by the measuring setup. The ring structure is clearly visible in the inset of *Fig. 4.7.2(b)* measured at λ_0 = 800 nm with a time-integrating matrix detector. A very uniform spatial intensity distribution is achieved with such spiral gratings as discussed in the next section.

4.7.3 Nondiffracting propagation behavior

Because of the finite radius of the axicon, the nondiffracting zone is also of finite extension. The theoretical maximum nondiffracting distance was calculated to be in the range of 10 mm and 20 mm for SE1 and SE2, respectively. In the experiments, pulses of 12 fs as well as of 6.5 fs pass through the axicons. The intensity pattern was recorded with a CCD-camera at various distances. The nondiffracting behavior is obtained for all vortex beams independently on the topological charge or pulse duration as is immediately derived from the axial intensity cuts shown in *Fig. 4.7.3*.

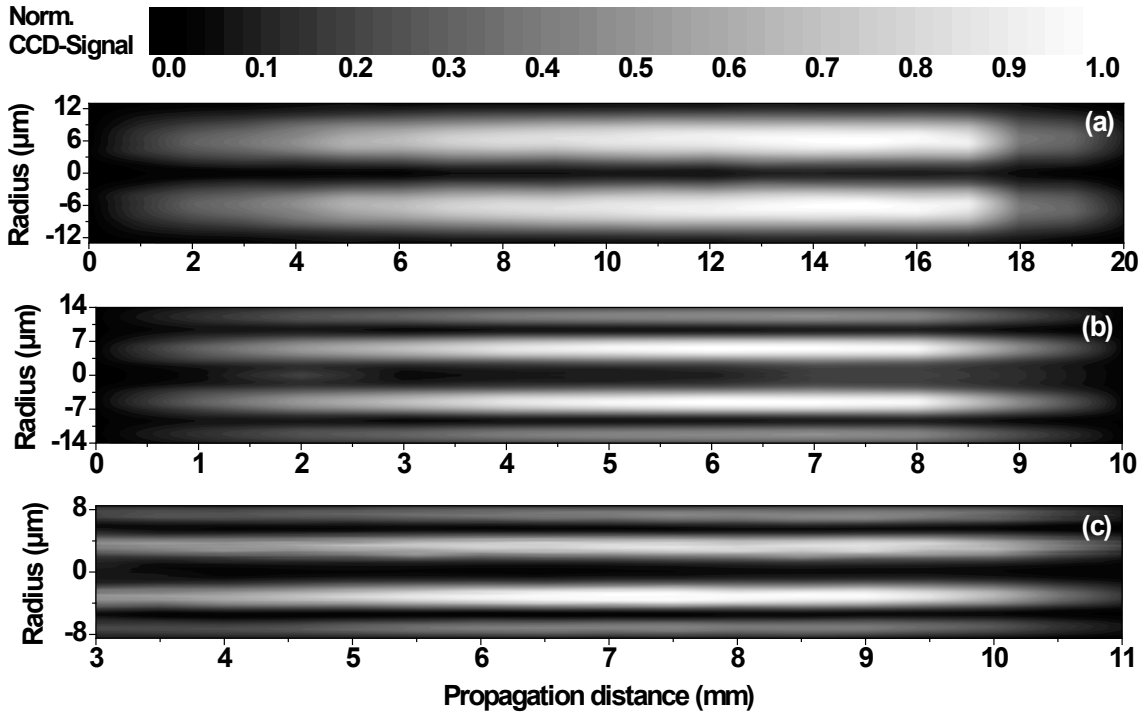

Fig. 4.7.3 Nondiffracting propagation behavior of pulsed optical vortices detected with a time-integrating CCD- and EMCCD camera at various distances: **(a)** Right-handed vortex with a topological charge ℓ = -1 for 12 fs input pulses, **(b)** right-handed vortex with a topological charge ℓ = -2 for 12 fs input pulses, **(c)** left-handed vortex with a topological charge ℓ = 2 for 6.5 fs input pulses.

A comparison of the axial intensity structures of $\ell = 1$ with those of $\ell = 2$ vortex beams reveals a similar propagation behavior. In all three cases, the ring of maximum intensity is surrounded by weaker concentric rings of lower intensity whereby the overall optical efficiency including the outer rings was about 20 %. The intensity increases slowly with the distance and decreases relatively fast at the end of the Bessel zone. The ring contrast over the entire depth is excellent and reaches even levels of > 90 %. For very short pulses, a theoretical conical angle of 6.7° was calculated by using the grating equation plus Snell's law of refraction for a beam at normal incidence on the optical element. The results agree very well with the experimental propagation conditions. Detailed information regarding the propagation behavior of cw and pulsed vortices can be extracted from reference [Ric09], where additional simulations with monochromatic light were also performed to confirm the measured data.

4.7.4 Measuring the orbital angular momentum

The wavefront rotation was measured via a SHS-sensor (array period $p = 300$ µm) at suitable distances from the programmed elements. Two types of SHS were used. The sensitivity of the commercial SHS was sufficient to resolve the vortex behavior of the main inner ring whereas in a modified version needle beams were used to increase the sensitivity. For that reason, the substrate with microlenses was replaced by the microaxicons programmed into an LCoS-SLM.

Measuring the wavefront with a matrix of microlenses or microaxicons does not need a reference wave. Therefore, a broadband beam splitter is not required. This is a huge advantage compared to the interference method. The plane of interest was expanded by a microscope objective to determine the OAM of such micrometer-sized vortices. A calibration of the magnification factor was performed by an optical element of a well-known periodical structure. Afterwards the spot position on the matrix detector were captured with and without the spiral grating. The resulting vector plot of the spatial elongations of the needle beams is shown in *Fig. 4.7.4(a)*. It should be noted that the vector field represents a direct measure of the phase gradient of the vortex beam. The sensitivity is sufficient to read out also information about the screw angle even in the higher order fringes. In *Fig. 4.7.4(b)*, the theoretical radial decay of screw angles (central wavelength of $\lambda_0 = 810$ nm) for a vortex beam of $\ell = 2$ is compared to experimental results from the two innermost rings. For this purpose, the screw angles were azimuthally averaged to reduce the measuring errors by filters or other disturbing optical elements. The error bar indicates the range of minimum and maximum value. It is found that the measured values are slightly higher in comparison to a pure $\ell = 2$ vortex. An

explanation is found in the illumination with a broadband spectrum and higher order vortex terms due to an imperfect spiral shape of the grating.

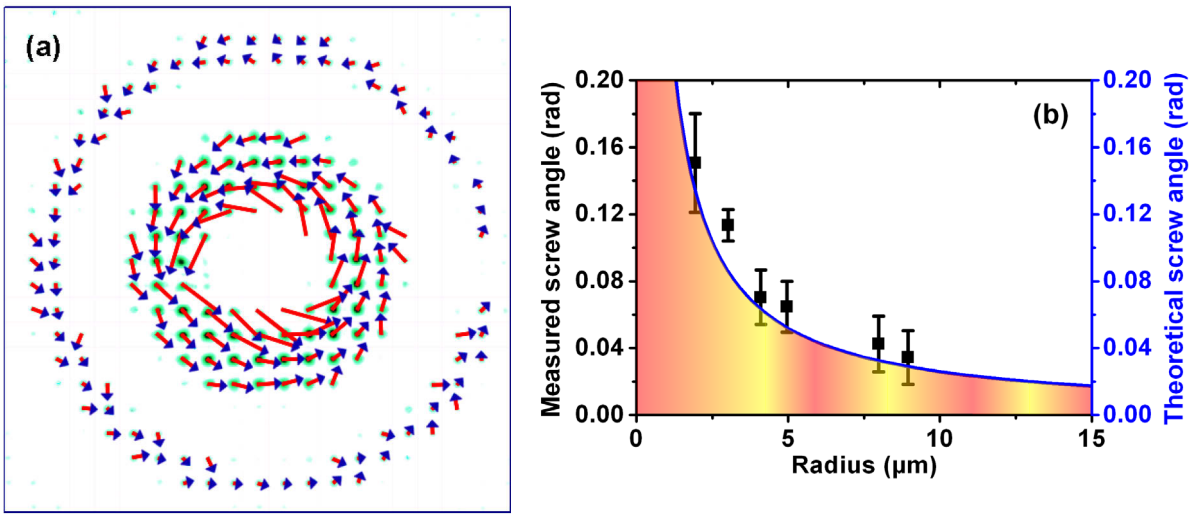

Fig. 4.7.4 Measured wavefront distortion of pulsed vortex Bessel beams with counterclockwise OAM of $\ell = 2$ at various distances: **(a)** Vector plot of the spatial elongations of the needle beams (the spatial dimensions are defined in *Fig. 4.7.3(c)*), **(b)** Screw angles as a function of the radius (blue solid line: theoretical curve).

A further advantage can be demonstrated by capturing the axial evolution of the spatial distribution of the phase gradient, which allows to measure and visualize the vortex decomposition.

In a second series of experiments, the commercial type of SHS and 'Laser A' was used to observe a rotation of the vector field and its decomposition with the distance. The vortex region was recorded with a sufficient accuracy (small statistical spread of the vector length and direction). Such a behavior can be found in *Fig. 4.7.5* where a $\ell = 2$ vortex decomposes into two orbital momentum beams of a topological charge $\ell = 1$. Then, the screw angle becomes a complex function of the radial and axial coordinates.

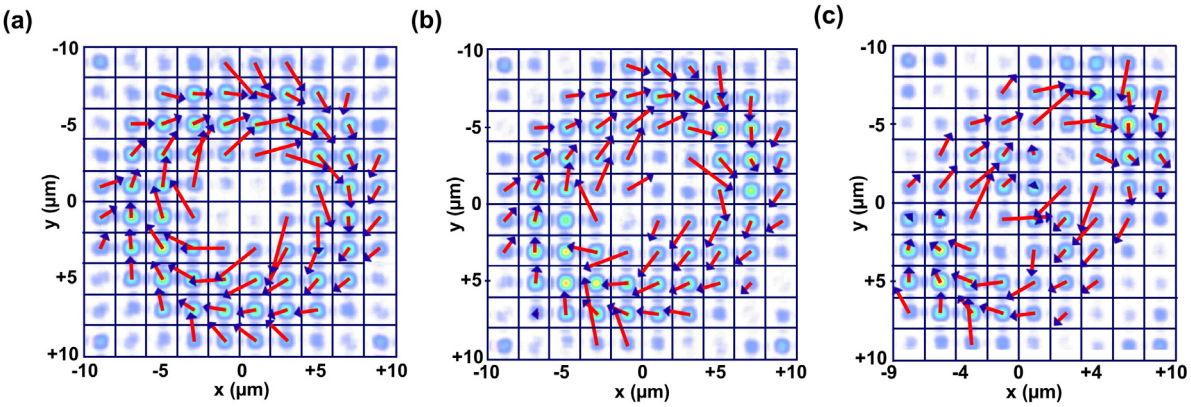

Fig. 4.7.5 Measured wavefront distortion of pulsed vortex Bessel beams with a clockwise OAM of $\ell = 2$ measured at various distances: **(a)** $z = 4$ mm **(b)** $z = 10$ mm **(c)** $z = 16$ mm The decomposition of the vortex is complete at a distance of about z = 13 mm.

Apart from different lasers used for the generation of $\ell = 2$ OAM beams the diffractive axicon has operated in two alignments. For the first configuration, the surface of the structured side pointed in the direction of the detector (see *Fig. 4.7.5*). In this case the rotational vortex circulates clockwise (right-handed). For the second alignment, the element was rotated by 180 degree (unstructured surface on the detector side). As expected, the sense of rotation appears to be reversed, which is evident from the vector field at an axial distance of z = 7 mm as shown in *Fig. 4.7.4(a)*.

Finally, a further clear fingerprint of the vortex properties was also found in two-dimensional spectral maps of the central region (4 µm x 4 µm). The spectral FWHM maps for $\ell = 2$ in *Fig. 4.7.6(a)* measured for the spiral axicon used in the experiments reported above and $\ell = 1$ as generated by a second reference axicon are shown in *Fig. 4.7.6(b)*. The different topological charges are clearly indicated by 4- and 2-fold leave-like patterns (blue: small bandwidth, red: large bandwidth).

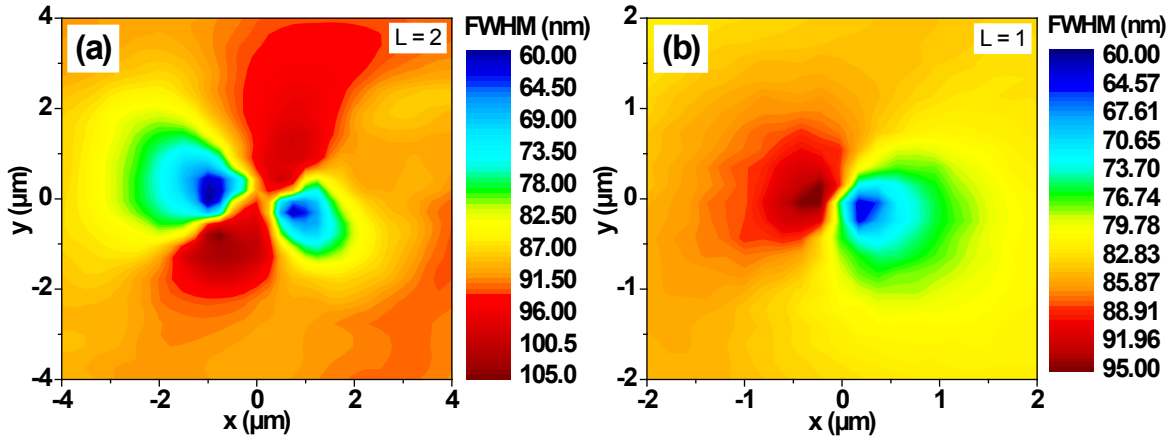

Fig. 4.7.6 Spectral maps for two few-cycle vortex beams with topological charges of (a) $\ell = 2$ (CGH as used for the time-wavefront experiments reported here) and (b) $\ell = 1$.

CHAPTER **5**

5 Summary and conclusions

5.1 Summary of the results

This thesis is focused on the generation and characterization of new types of nondiffracting wave phenomena, including pulsed needle beams (or needle pulses) and highly localized wave packets. Both theory and experiment are shown.
Adaptive shaping of such beams was realized by applying appropriate reflective types of spatial light modulators having excellent pulse transfer properties. Ultraflat discretized axicons with widely tunable parameters were programmed in transient phase maps with high structural flexibility. The shortest pulses formed in the experiments had input pulse durations of about 6.5 fs corresponding to 2.5 cycles of the electric field at a central wavelength of 800 nm. Spatiotemporal information of the shaped wave packets was extracted by linear as well as nonlinear measuring techniques incorporating highly sensitive matrix detectors. The results show the generation of ultrashort-pulsed linear light bullets and nondiffracting patterns with high spatial localization giving rise to a generalization beyond the approaches of nondiffracting beams known so far.

(1) Pulsed needle beams

Specific new modifications to nondiffracting Bessel beams having only one intensity maximum referred to as “needle beams” were studied. The generation of needle beams requires either spatially filtering out the Bessel fringes by self-apodized truncation

(with high losses) or to work with appropriately adapted boundary conditions, i.e., at ultrasmall conical angles (with minimum losses). A detail investigation of the propagation properties revealed that an unperturbed spatial and temporal characterization is only obtained within the central maximum at nearly equal pulse travel times of the interfering conical parts.

Such nondiffracting and nondispersing pulsed needle beams were generated from ultrashort laser pulses in the few cycle regime with diameters scalable between 1 mm down to 40 µm. Necessary beam corrections were implemented by adequately adapting the shape of the axicons. Externally induced aberrations, e.g. by large angles of incidence (up to 50°), were successfully compensated. Self-imaging properties of arrays of needle beams were analyzed on the basis of a diffraction-free coherent superposition (analogous to the Talbot effect). An extended depth of focus (almost doubled in comparison to a simple cone axicon) was observed by exploiting the advantages of Fresnel-zone-type axicons (programmable fraxicons).

(2) Pulsed hollow beams

In the next step, the specific advantages of needle beams (angular tolerance, aberration correction, etc.) were transferred to hollow beams. For this purpose, the combination of convex and concave axicons (W-shape) yields spatially non-oscillating ring-shaped needle beams. Here it was shown that arrays of optical nondiffracting bottle beams can be generated. For example, a nondiffracting zone with depth of focus of around 10 mm was achieved for hollow beams with a ring diameter of 200 µm. A fine tuning of the ring diameter and the intensity distribution by changing the base angle of the axicons was demonstrated.

(3) Generalization to highly localized wave packets

The approaches of needle and hollow beams were further generalized to the concept of highly localized beams and highly localized (ultrashort-pulsed) wave packets (HLWs) which can be understood as the result of simple geometrical transforms of needle beams. A certain class of well-adapted axicons with noncircular profiles was used to generate non-oscillating, nondiffracting wave packets of more complex structure (e.g. stadium-like distribution), while keeping their temporal characteristics undistorted as well and following an optimization principle with respect to the energy concentration (no parasitic fringes).

(4) Nondiffracting image patterns

Various HLWs were used as buildings blocks for more complex light distributions. The concept was demonstrated by converting a Gaussian spatial intensity distribution into particular image patterns. The required intensity modulation was achieved by a flexible arrangement of axicons corresponding to the target pattern and adapted to the input beam profile. Large cross-talk free propagation distances were obtained (e.g. 55 mm for needle beams with an axially averaged beam radius of 88 μm). The decomposition of an image shape into binary as well as complex HLWs was possessed (e.g. by propagating the few-cycle pulsed nondiffracting logo of the MBI).

(5) Axially dependent beam quality factor

For a suitable description of the degree of localization of needle beams and related types of highly localized waves, a new (modified) beam parameter product M_{NB}^2 for needle beams was defined. An axially dependent beam quality factor reveals the spatial localization of the wave packet at the corresponding axial positions. On the basis of M_{NB}^2 it becomes clear that needle beams generated from Gaussian beams partially conserve Gaussian propagation properties, manifesting in factors $M_{NB}^2 > 1$. The beam quality factor approximates to 1 for decreasing beam diameters.

(6) Extended Shack-Hartmann sensors

The measuring principle of the conventional Shack-Hartmann wavefront sensor (i.e. a combination of a wavefront division with a microlens array and an analysis of transversal spot elongations) was improved by using programmable axicons to realize a reconfigurable sensor with nondiffracting HLWs. This enables a measurement of the wavefront properties of ultrashort laser pulses with a high resolution and dynamics. In the given example, even a maximum radius of curvature of 10 m was resolved. A shape encoding technique was introduced to achieve an individualization of the spot shape for an improved wavefront detection. Moreover, wavefront curvatures of up to 33 m were measured with the method of temporal delay mapping.

(7) Spatially resolved autocorrelation

The temporal properties of extended, nondiffracting Shack-Hartmann architectures in combination with interferometers were further exploited to study spatially dependent pulse features which are not accessable with spatially integrating detection techniques. A modified 2^{nd} order autocorrelation setup was applied to perform accurate measurements of the spatially resolved pulse duration (2D spatial chirp) across a pulsed laser beam. A comparison between aberration-corrected and -uncorrected needle beams reveals significant differences in the width and shape of the autocorrelations traces. Moreover, the experiments indicated that the technique enables to determine the arrival times of spatially separated parts of the wave packets with sub-femtosecond resolution (temporal delay mapping).

(8) Ultrashort vortex pulses

The Shack-Hartmann sensor (SHS) with needle beams was applied to the detection of the orbital angular momentum of ultrashort-pulsed vortex beams generated with self-compensating diffractive optical elements. Pulsed vortices of 8.3 fs were generated from single and double spiral gratings. It was proved that such pulsed beams can be described by higher order Bessel beams. In these proof-of-principle experiments, the microscopic vortices (diameter about 7 μm) had a nondiffracting zone of few millimeters. In contrast to previous measurements of other groups, the high sensitivity of the improved SHS enabled to resolve the characteristic vector fields of parts of the beams with even higher order topological charges.

5.2 Conclusions

Highly localized wave packets (HLWs) are of fundamental interest in theoretical optics and promise many potential applications. Two of their particular properties are of high relevance in ultrashort-pulse laser physics: (i) spatial-temporal confinement of light in oscillation-free spatial distributions and (ii) the conservation of the temporal properties during the propagation.

The combination of micrometer dimensions and few-cycle pulses in a programmable setup (including an LCoS-SLM) was demonstrated for the first time and showed that both a high temporal and spatial localization is achieved simultaneously. The generation of HLWs represents the only known way to realize linear-optical, oscillation-free "light bullets" without unwanted dispersal of the energy in ring-shaped beam structures. In this context, an enhanced method to further manipulate the spatiotemporal structure by an overlaid diffraction grating is proposed.

The technique of "flying images" puts the concept of propagation-invariant beams beyond the reach of solitary pulsed needle beams and opens a field of new spurring applications like atom trapping and guiding, coherence tomography, nondiffracting laser resonators, and optical pumping of plasmas. In contrast to classical diffractive optics, the propagation of image features depends much less on their size. This compositional principle is complementary to the approach of nondiffracting image projection with axicons as introduced by McLeod [Mcl54]. However, algorithms have to be developed to find the optimal phase mask design for the particular application.

The extension of Shack-Hartmann sensors by programmable needle beams represents an important step towards well-defined properties of ultrashort pulses and can improve existing measuring techniques in microscopy and spectroscopy. Thanks to the usage of needle beams, it is now possible, to measure wavefront properties with a high sensitivity, for instance, very weak orbital angular momenta.

Furthermore, the use of arrays enable a highly accurate noncollinear, spatially resolved second order autocorrelations in combination with a simultaneous detection of the wavefront. An extension by a grating opens the possibility to retrieve also the spectral phase of a pulse at each spatial position. Simultaneously, the temporal delay mapping technique seems to be a promising application in pump-and-probe experiments where a comparison of temporal distorted and undistorted needle beams provides additional information about the process to be measured. However, the availability of carrier phase stabilized lasers is a basic

precondition to perform such experiments with high accuracy. The diffraction-free self-imaging effect may be used as an axial periodic optical lattice to trap particles in a manner that they are lined up in arrays of string of pearls.

Finally, the 8 fs optical vortex represents the shortest vortex pulse ever reported for a compact optical element and has applications in temporally resolved stimulated emission depletion (STED) fluorescence microscopy. It is expected that even shorter vortex pulses are accessible using the same design methodology.

Bibliography

[Abr72] M. Abramowitz, and I. A. Stegun, *Handbook of Mathematical Functions with Formulas, Graphs, and Mathematical Tables* (Dover Publications, 9th printing, New York, 1972), pp. 358-364.

[Ald02] J. Alda, Laser and Gaussian Beam Propagation and Transformation. In *Encyclopedia of Optical Engineering* (CRC Press, New York, 2002), pp. 999-1013.

[Akt03] S. Akturk, M. Kimmel, P. O'Shea, R. Trebino, "Measuring spatial chirp in ultrashort pulses using single-shot Frequency-Resolved Optical Gating," Opt. Express **11**, 69-78 (2003).

[Akt05] S. Akturk, X. Gu, P. Gabolde, and R. Trebino, "The general theory of first-order spatio-temporal distortions of Gaussian pulses and beams," Opt. Express **13**, 8642-8661 (2005).

[Ale12] P. Aleahmad, M.-A. Miri, M. S. Mills, I. Kaminer, M. Segev, and D. N. Christodoulides, "Fully vectorial accelerating diffraction-free Helmholtz beams," Phys. Rev. Lett. **109**, 203902 (2012).

[All92] L. Allen, M.W. Beijersbergen, R. J. C. Spreeuw, and J. P. Woerdman, "Orbital angular momentum of light and the transformation of Laguerre-Gaussian laser modes," Phys. Rev. A **45**, 8185-8189 (1992).

[All94] L. Allen, M. Babiker, and W. L. Power, "Azimuthal Doppler shift in light beams with orbital angular momentum," Opt. Commun. **112**, 141-144 (1994).

[All00] L. Allen and M. J. Padgett, “The Poynting vector in Laguerre-Gaussian beams and the interpretation of their angular momentum density,” Opt. Commun. **184**, 67-71 (2000).

[All03] L. Allen, S. M. Barnett, M. J. Padgett, *Optical Angular Momentum* (Taylor & Francis, Bristol: Institute of Physics, 2003).

[Alo10] B. Alonso, Í. J. Sola, Ó. Varela, J. Hernández-Toro, C. Méndez, J. San Román, A. Zaïr, and L. Roso, “Spatiotemporal amplitude-and-phase reconstruction by Fourier-transform of interference spectra of high-complex-beams,” JOSA B **27**, 933-940 (2010).

[And08] M. E. Anderson, A. Monmayrant, S.-P. Gorza, P. Wasylczyk, and I. A. Walmsley, “SPIDER: A decade of measuring ultrashort pulses,” Laser Phys. Lett. **5**, 259–266 (2008).

[Apt06] B. Apter, and U. Efron, “Combined Blazed Grating/Gires-Tournois Resonator for Liquid Crystal Beam Switching,” J. Lightwave Technol. **24**, 962-969 (2006).

[Ara11] L. E. E. de Araujo, and M. E. Anderson, “Measuring vortex charge with a triangular aperture,” Optics Letters **36**, 787-789 (2011).

[Arl00a] J. Arlt and M. J. Padgett, “Generation of a beam with a dark focus surrounded by regions of higher intensity: the optical bottle beam,” Opt. Lett. **25**, 191-193 (2000).

[Arl00b] J. Arlt, T. Hitomi, and K. Dholakia, “Atom guiding along Laguerre–Gaussian and Bessel light beams,” Appl. Phys. B **71**, 549–54 (2000).

[Arl01] J. Arlt, K. Dholakia, J. Soneson, and Ewan M. Wright, “Optical dipole traps and atomic waveguides based on Bessel light beams,” Phys. Rev. A **63**, 063602 (2001).

[Bar83] N. B. Baranova, A. V. Mamaev, N. F. Pilipetsky, V. V. Shkunov, and B. Ya. Zel’dovich, “Wave-front dislocations: topological limitations for adaptive systems with phase conjugation,” JOSA **73**, 525–528 (1983).

[Bar02] S. M. Barnett, “Optical angular-momentum flux,” J. Opt. B: Quantum Semiclass Opt. **4**, 7-16 (2002).

[Bat15] H. Bateman, Electrical and optical wave motion (Cambridge University Press, Cambridge, 1915).

[Baz90] V. Yu. Bazhenov, M. V. Vasnetsov, and M. S. Soskin, “Laser beams with screw dislocations in their wavefronts,” Pis’ma Zh. Eksp. Teor. Fiz. **52**, 1037 (1990) [JETP Lett. 52, 429 (1990)].

[Bei93] M. W. Beijersbergen, L. Allen, H. E. L. O. van der Veen, and J. P. Woerdman, "Astigmatic laser mode converters and transfer of orbital angular momentum," Opt. Commun. **96**, 123–132 (1993).

[Ben08] D. A. Bender, J. W. Nicholson, and M. Sheik-Bahae, "Ultrashort laser pulse characterization using modified spectrum auto-interferometric correlation (MOSAIC)," Opt. Express **16**, 11782-11794 (2008).

[Ber79] M. V. Berry and N. L. Balazs, "Nonspreading wave packets," Am. J. Phys. **47**, 264-267 (1979).

[Ber96] M.V. Berry and S. Klein, "Integer, fractional and fractal Talbot effects," J. Mod. Opt. **43**, 2139-2164 (1996).

[Ber04] M.V. Berry, "Optical vortices evolving from helicoidal integer and fractional phase steps," J. Opt. A: Pure Appl. Opt. **6**, 259–268 (2004).

[Ber10] G. C. G. Berkhout, M. P. J. Lavery, J. Courtial, M. W. Beijersbergen, and M. J. Padgett, "Efficient sorting of orbital angular momentum states of light," Phys. Rev. Lett. **105**, 153601 (2010).

[Bes89] I. M. Besieris, A. M. Shaarawi, and R. W. Ziolkowski, "A bi-directional traveling plane wave representation of exact solution of the scalar field equation," J. Math. Phys. **30**, 1254-1269 (1989).

[Bet36] R. A. Beth, "Mechanical Detection and Measurement of the Angular Momentum of Light," Phys. Rev. **50**, 115 (1936).

[Bez04] K. Bezuhanov, A. Dreischuh, G. G. Paulus, M. G. Schätzel, and H. Walther, "Vortices in femtosecond laser fields," Opt. Lett. **29**, 1942-1944 (2004).

[Boc05] M. Bock, "Räumlich-spektral aufgelöste Charakterisierung von ultrakurzen Laserimpulsen," Diploma thesis, University of Applied Science Wildau, Berlin (2005).

[Boc08a] M. Bock, "Spatio-spectral shaping of few-cycle laser pulses with liquid crystal displays," Master thesis, University of Applied Science Wildau, Berlin (2008).

[Boc08b] M. Bock , S. K. Das, R. Grunwald, S. Osten , P. Staudt and G. Stibenz, "Spectral and temporal response of liquid-crystal-on-silicon spatial light modulators," Appl. Phys. Lett. **92**, 151105 (2008).

[Boc09] M. Bock, S. K. Das, and R. Grunwald, "Programmable ultrashort-pulsed flying images," Opt. Express **17**, 7465-7478 (2009).

[Boc12a] M. Bock, S. K. Das, C. Fischer, M. Diehl, P. Börner, and R. Grunwald, "Reconfigurable wavefront sensor for ultrashort pulses," Opt. Lett. **37**, 1154-1156 (2012).

[Boc12b] M. Bock, S. K. Das, and R. Grunwald, "Ultrashort highly localized wavepackets," Opt. Express **20**, 12563-12578 (2012).

[Boc12c] M. Bock, J. Jahns, and R. Grunwald, "Few-cycle high-contrast vortex pulses," Opt. Lett. **37**, 3804-3806 (2012).

[Bor99] M. Born, and E. Wolf, Principles of Optics (Cambridge University Press, Cambridge, 1999).

[Bou02] Z. Bouchal, "Controlled spatial shaping of nondiffracting patterns and arrays," Opt. Lett. **27**, 1376-1378 (2002).

[Bow07] P. Bowlan, P. Gabolde, and R. Trebino, "Directly measuring the spatio-temporal electric field of focusing ultrashort pulses," Opt. Express **15**, 10219-10230 (2007).

[Bow09] P. Bowlan, H. Valtna-Lukner, M. Lõhmus, P. Piksarv, P. Saari, and R. Trebino, "Measuring the spatiotemporal field of ultrashort Bessel-X pulses," Opt. Lett. **34**, 2276-2278 (2009).

[Bow10] R. W. Bowman, A. J. Wright, and M. J. Padgett, "An SLM- based Shack-Hartmann wavefront sensor for aberration correction in optical tweezers," J. Opt. **12**, 124004 (2010).

[Car99] C. F. R. Caron, and R. M. Potvliege, "Free-space propagation of ultrashort pulses: spacetime couplings in Gaussian pulse beams," Journal of Modern Optics **46**, 1881-1891 (1999).

[Chr96] J. Christou, V. Tikhonenko, Y. S. Kivshar, and B. Luther-Davies, "Vortex soliton motion and steering," Opt. Lett. **21**, 1649–1651 (1996).

[Che08] M. Chen, F. S. Roux, and J. C. Olivier, "Detection of phase singularities with a Shack-Hartmann wavefront sensor," JOSA A **24**, 1994-2002 (2007).

[Che12] Z. Chen, L. Hua, and J. Pu, "Tight Focusing of Light Beams: Effect of Polarization, Phase and Coherence" in Progress in Optics **57** (2012).

[Cho10] A. Chong, W. H. Renninger, D. N. Christodoulides, and F. W. Wise, "Airy–Bessel wave packets as versatile linear light bullets," Nature Photonics **4**, 103-106 (2010).

[Con04] C. Conti, "Generation and nonlinear dynamics of X waves of the Schrödinger equation," Phys. Rev E **70**, 046613 (2004).

[Cot07] D. M. Cottrell, J. M. Craven, and J. A. Davis, "Nondiffracting random intensity patterns," Opt. Lett **32**, 298-300 (2007).

[Cou97] J. Courtial, K. Dholakia, L. Allen, and M. J. Padgett, "Second-harmonic generation and the conservation of orbital angular momentum with high-order Laguerre-Gaussian modes," Phys. Rev. A **56**, 4193 4106 (1997).

[Cou98] J. Courtial, K. Dholakia, D. A. Robertson, L. Allen, and M. J. Padgett, "Rotational Frequency Shift of a Light Beam," Phys. Rev. Lett. **80**, 3217 (1998).

[Cow57] J. M. Cowley and A.F. Moodie, "Fourier Images: I — The point source," Proc. Phys. Soc. **70**, 486-496 (1957).

[Dav96] Jeffrey A. Davis, E. Carcole, and Don M. Cottrell, "Nondiffracting interference patterns generated with programmable spatial light modulators," Appl. Opt. **35**, 599-602 (1996).

[Del94] K. W. DeLong, Rick Trebino, and Daniel J. Kane, "Comparison of ultrashort-pulse frequency-resolved-optical-gating traces for three common beam geometries," JOSA B **11**, 1595-1608 (1994).

[Dho96] K. Dholakia, N. B. Simpson, M. J. Padgett, and L. Allen, "Second-harmonic generation and the orbital angular momentum of light," Phys. Rev. A **54**, R3742 (1996).

[Dur87] J. Durnin, J. J. Miceli, Jr., and J. H. Eberly, "Diffraction-free beams," Phys. Rev. Lett. **58**, 1499-1501 (1987).

[Dys58] J. Dyson, "Circular and spiral diffraction gratings," Proc. R. Soc. Lond. A **248**, 93–106 (1958).

[Enk94] S. J. van Enk, and G Nienhuis, "Commutation rules and eigenvalues of spin and orbital angular momentum of radiation fields," J. Mod. Opt. **41**, 963-977 (1994).

[Fen98] S. Feng, H. G. Winful, and R. W. Hellwarth, "Gouy shift and temporal reshaping of focused single-cycle electromagnetic pulses," Opt. Lett. **23**, 385-387 (1998).

[Fen00] S. M. Feng and H. G. Winful, "Spatiotemporal structure of isodiffracting ultrashort electromagnetic pulses," Phys. Rev. E. **61**, 862-873 (2000).

[Fen01] S. M. Feng, and H. G. Winful, "Physical origin of the Gouy phase shift," Opt. Lett. **26**, 485-487 (2001).

[Gal01] L. Gallmann, G. Steinmeyer, D. H. Sutter, T. Rupp, C. Iaconis, I. A. Walmsley, and U. Keller, "Spatially resolved amplitude and phase characterization of femtosecond optical pulses," Opt. Lett. **26**, 96-98 (2001).

[Gar97] B. A. Garetz and S. Arnold, "Variable frequency shifting of circularly polarized laser radiation via a rotating half-wave retardation plate," Opt. Commun. **31**, 1 (1997).

[Gib04] G. Gibson, J. Courtial, M. Padgett, M. Vasnetsov, V. Pas'ko, S. Barnett, and S. Franke-Arnold, "Free-space information transfer using light beams carrying orbital angular momentum," Opt. Express **12**, 5448-5456 (2004).

[Gir64] F. Gires, and P. Tournois, "Interféromètre utilisable pour la compression d'impulsions lumineuses modulées en fréquence," C. R. Acad. Sc. Paris **258**, 6112-6115 (1964).

[Gol90] I. Golub and R. Tremblay, "Light focusing and guiding by an axicon-pair-generated tubular light beam," JOSA B **7**, 1264-1267 (1990).

[Gol06] I. Golub, "Fresnel axicon," Opt. Lett. **31**, 1890-1892 (2006).

[Gor87] F. Gori, G. Guattari, C. Padovani, "Bessel-Gauss beams", Opt. Commun. **64**, 491-495 (1987).

[Gou90] L. G. Gouy, "Sur une propriete nouvelle des ondes lumineuses", C. R. Acad. Sci. Paris **110**, 1251-1253 (1890).

[Gri03] D. G. Grier, "A revolution in optical manipulation," Nature **424**, 810-816 (2003).

[Gru03] R. Grunwald, U. Neumann, U. Griebner, K. Reimann, G. Steinmeyer, and V. Kebbel, "Ultrashort-pulse wavefront autocorrelation," Opt. Lett. **28**, 2399-2401 (2003).

[Gru07] R. Grunwald, S. Huferath, M. Bock, U. Neumann, and S. Langer, "Angular tolerance of Shack-Hartmann wavefront sensors with microaxicons," Opt. Letters **32**, 1533-1535 (2007).

[Gru08] R. Grunwald, M. Bock, V. Kebbel, S. Huferath, U. Neumann, G. Steinmeyer, G. Stibenz, J.-L. Néron, and M. Piché, "Ultrashort-pulsed truncated polychromatic Bessel-Gauss beams," Opt. Express **16**, 1077-1089 (2008).

[Gue90] R. Guenther, Diffraction and Gaussian Beams, In *Modern Optic* (John Wiley and Sons, New York, 1990), pp. 323–360.

[Gut00] J. C. Gutiérrez-Vega, M. D. Iturbe-Castillo, and S. Chávez-Cerda, "Alternative formulation for invariant optical fields: Mathieu beams," Opt. Lett. **25**, 1493-1495 (2000).

[Gut08] J. C. Gutiérrez-Vega, and C. López-Mariscal, "Nondiffracting vortex beams with continuous orbital angular momentum order dependence," J. Opt. A: Pure Appl. Opt. **10**, 015009 (2008).

[Har00] J. Hartmann, „Bemerkungen über den Bau und die Justierung von Spektrographen." Z. Instrumentenk. **20**, 47-58 (1900).

[Har08] H. Harnandez-Figueroa, M. Zamboni-Rached, and E. Recami (Eds.), *Localized Waves - Theory and experiments* (Wiley & Sons, New Jersey, 2008).

[Hec92] N. R. Heckenberg, R. McDuff, C. P. Smith, and A. G. White, "Generation of optical phase singularities by computer-generated holograms," Opt. Lett. **17**, 221-223 (1992).

[Hel94] S. W. Hell and J. Wichmann, "Breaking the diffraction resolution limit by stimulated emission: stimulated-emission-depletion fluorescence microscopy," Opt. Lett. **19**, 780-782 (1994).

[Her91] M. R. Herman, T. A. Wiggins, "Production and uses of diffractionless beams," J. Opt. Soc. Am. A **8**, 932-942 (1991).

[Her00] R. M. Herman and T. A. Wiggins, "Bessel-like beams modulated by arbitrary radial functions," J. Opt. Soc. Am. A **17**, 1021-1032 (2000).

[Her08] H. E. Hernández-Figueroa, M Zamboni-Rached, and E. Recami, Localized waves, Theory and experiments (Johny Wiley and Sons, New York, 2008), pp. 7-15.

[Hod92] N. Hodgson, H. Weber, *Optische Resonatoren - Grundlagen, Eigenschaften, Optimierung* (Springer-Verlag, Heidelberg, 1992).

[Hu06] M.-L. Hu, C.-Y. Wang, Y.-J. Song, Y.-F. Li, and L. Chai, "A hollow beam from a holey fiber," Opt. Express **14**, 4128-4134 (2006).

[Huf08] S. Huferath-von Luepke, V. Kebbel, M. Bock, and R. Grunwald, Noncollinear autocorrelation with radially symmetric nondiffracting beams, SPIE Optics+Photonics / Optical Engineering + Applications / Advanced Metrology Conference, San Diego, USA, 2008, in: Proc. SPIE 7063, 706311-706311-12 (2008).

[Iac98] C. Iaconis, I. A. Walmsley, "Spectral Phase Interferometry for Direct Electric-Field Reconstruction of Ultrashort Optical Pulses," Opt. Lett. **23**, 792–794 (1998).

[Kär04] F. X. Kärtner, *Few-cycle laser pulse generation and its applications* (Springer, New York, 2004).

[Ket98] V. Kettunen, and J. Turunen, "Propagation-invariant spot arrays," Opt. Letters **23**, 1247-1249 (1998).

[Kho92] S.N. Khoninaa, V.V. Kotlyara, M.V. Shinkaryeva, V.A. Soifera, and G.V. Usplenieva, "The Phase Rotor Filter," J. of Mod. Opt. **39**, 1147-1154 (1992).

[Kim97] G. Kim, J. Jeon, K. Ko, H. Moon, J. Lee, and J. Chang, "Optical vortices produced with a nonspiral phase plate," Appl. Opt. **36**, 8614-8621 (1997).

[Kiv98] Y. S. Kivshar, J. Christou, V. Tikhonenko, B. Luther-Davies, and L. M. Pismen, "Dynamics of optical vortex solitons," Opt. Comm. **152**, 198–206 (1998).

[Kiv03] Y. Kivshar and G. Agrawal, *Optical Solitons: From Fibers to Photonic Crystals*, Academic Press, San Diego, Calif. (2003).

[Kor95] V. P. Koronkevich, I. A. Mikhaltsova, E. G. Churin, and Yu. I. Yurlov, "Lensacon," Appl. Opt. **34**, 5761 (1995).

[Lav12] M. P. J. Lavery, D. J. Robertson, G. C. G. Berkhout, G. D. Love, M. J. Padgett, and J. Courtial, "Refractive elements for the measurement of the orbital angular momentum of a single photon," Opt. Express **20**, 2110-2115 (2012).

[Lea04] J. Leach, E. Yao, and M. J. Padgett, "Observation of the vortex structure of a non-integer vortex beam," New J. Phys. **6**, 71 (2004).

[Lee04] W.M. Lee, X.-C. Yuan, K. Dholakia, "Experimental observation of optical vortex evolution in a Gaussian beam with an embedded fractional phase step," Opt. Comm. **239**, 129-135 (2004).

[Len11] F. Lenzini, S. Residori, F. T. Arecchi, and U. Bortolozzo, "Optical vortex interaction and generation via nonlinear wave mixing," Phys. Rev. A **84**, 061801 (2011).

[Lin02] N. Lindlein and J. Pfund, "Experimental results for expanding the dynamic range of a Shack-Hartmann sensor using astigmatic microlenses," Opt. Eng. **41**, 529-533 (2002).

[Lin04] F. Lindner, G. G. Paulus, H. Walther, A. Baltuška, E. Goulielmakis, M. Lezius, and F. Krausz, "Gouy Phase Shift for Few-Cycle Laser Pulses," Phys. Rev. Lett. **92**, 113001 (2004).

[Loh88] A.W. Lohmann, "An array illuminator based on the Talbot-effect," Optik **79**, 41-45 (1988).

[Lõh12] M. Lõhmus, P. Bowlan, P. Piksarv, H. Valtna-Lukner, R. Trebino, and P. Saari, "Diffraction of ultrashort optical pulses from circularly symmetric binary phase gratings," Opt. Lett. **37**, 1238-1240 (2012).

[Lon04] S. Longhi, "Localized subluminal envelope pulses in dispersive media," Opt. Lett. **29**, 147–149 (2004).

[Lu92] J.-y. Lu, and J. F. Greenleaf, "Nondiffracting X-waves: exact solutions to free-space scalar wave equation and their finite aperture realization," IEEE Trans. Ultrason. Ferroelectr. Freq. Control **39**, 19-31 (1992).

[Mac93] R. P. MacDonald, J. Chrostowski, S. A. Boothroyd, and B. A. Syrett, "Holographic formation of a diode laser nondiffracting beam," Appl. Opt. **32**, 6470 (1993).

[Man98] I. Manek, Yu. B. Ovchinnikov, R. Grimm, "Generation of a hollow laser beam for atom trapping using an axicon," Opt. Commun. **147**, 67-70 (1998).

[Mar84] O. E. Martinez, J. P. Gordon, and R. L. Fork, "Negative group-velocity dispersion using refraction," J. Opt. Soc. Am. A **1**, 1003-1006 (1984).

[Mar05] I. G. Mariyenko, J. Strohaber, and C. J. G. Uiterwaal, "Creation of optical vortices in femtosecond pulses," Opt. Express **13**, 7599-7608 (2005).

[Mar10] R. Martínez-Cuenca, V. Durán, V. Climent, E. Tajahuerce, S. Bará, J. Ares, J. Arines, M. Martínez-Corral, and Jesús Lancis, "Reconfigurable Shack–Hartmann sensor without moving elements," Opt. Letters **35**, 1338-1340 (2010).

[Mcl54] J. H. McLeod, "The Axicon: A New Type of Optical Element," JOSA **44**, 592-592 (1954).

[Min08] G. Minguez-Vega, O. Mendoza-Yero, J. Lancis,1 R. Gisbert, and P. Andrés, "Diffractive optics for quasi-direct space-to-time pulse shaping," Opt. Express **16**, 16993-16998 (2008).

[Mol07] G. Molina-Terriza, J. P. Torres, and L. Torner, "Twisted photons," Nature Physics **3**, 305-310 (2007).

[Nei02] A.T. O'Neil, I. MacVicar, L. Allen, and M. J.Padgett, "Intrinsic and extrinsic nature of the orbital angular momentum of a light beam," Phys Rev Lett. **88**, 053601 (2002).

[Nie96] G. Nienhuis, "Doppler effect induced by rotating lenses," Opt. Commun. **132**, 8 (1996).

[Nye74] J. F. Nye, and M.V. Berry, "Dislocations in Wave Trains," Proc. R. Soc. A **336**, 165 (1974).

[Oli00] S. Olivier, V. Laude, and J.-P. Huignard, "Liquid-Crystal Hartmann Wave-Front Scanner," Appl. Opt. **39**, 3838-3846 (2000).

[Pad00a] M. J. Padgett and L. Allen, "The Poynting vector in Laguerre-Gaussian laser modes," Opt. Commun. **121**, 36-40 (1995).

[Pad00b] M. Padgett, and L. Allen, "Light with a twist in its tail," Contemporary Physics **41**, 275-285 (2000).

[Ped93] Pedrotti, F.L.; Pedrotti, L.S. Characterization of Laser Beams, In *Introduction to Optics* (Prentice-Hall: Englewood Cliffs, NJ, 1993), pp. 456–483.

[Pig11] B. Piglosiewicz, D. Sadiq, M. Mascheck, S. Schmidt, M. Silies, P. Vasa, and C. Lienau, "Ultrasmall bullets of light - focusing few-cycle light pulses to the diffraction limit," Optics Express **19**, 14451-14463 (2011).

[Pik12] P. Piksarv, H. Valtna-Lukner, A. Valdmann, M. Lõhmus, R. Matt, and P. Saari, "Temporal focusing of ultrashort pulsed Bessel beams into Airy–Bessel light bullets," Opt. Express **20**, 17220-17229 (2012).

[Pla01] B. C. Platt and R. Shack, "History and principles of Shack– Hartmann wavefront sensing," J. Refract. Surg. **17**, 573–577 (2001).

[Por98] M. A. Porras, "Ultrashort pulsed Gaussian light beams." Phys. Rev. E **58**, 1086–1093 (1998).

[Por04] M. A. Porras, and P. Di Trapani, "Localized and stationary light wave modes in dispersive media," Phys. Rev. E **69**, 066606 (2004).

[Poy09] J. H. Poynting," The Wave Motion of a Revolving Shaft, and a Suggestion as to the Angular Momentum in a Beam of Circularly Polarised Light," Proc. R. Soc. Lond. A **82**, 560 (1909).

[Ray81] L. Rayleigh, "On Copying Diffraction–Gratings, and some Phenomena Connected Therewith," Philos. Mag. **11**, 196-205 (1881).

[Rei02] K. Reivelt and P. Saari, "Experimental demonstration of realizability of optical focus wave modes," Phys. Rev. E **66**, 056611 (2002).

[Rei04] K. Reivelt and P. Saari, "Bessel-Gauss pulse as an appropriate mathematical model for optically realizable localized waves," Opt. Lett. **29**, 1176-1178 (2004).

[Rha04] J. Rha, D. G. Voelz, and M. K. Giles, "Reconfigurable Shack-Hartmann wavefront sensor," Opt. Eng. **43**, 251-256 (2004).

[Ric09] A. Richter, "Generation of orbital angular momentum in femtosecond laser pulses by means of spiral phase elements," Master Thesis, FernUni in Hagen (2009).

[Rin12] J. D. Ring, J. Lindberg, A. Mourka, M. Mazilu, K. Dholakia, and M.R. Dennis, "Auto-focusing and self-healing of Pearcey beams," Opt. Express **17**, 18855-18966 (2012).

[Rou02] G. Rousseau, N. McCarthy, and M. Piché, "Description of pulse propagation in a dispersive medium by use of a pulse quality factor," Opt. Lett. **18**, 1649-1651 (2002).

[Saa96] P. Saari, Spatially and temporally nondiffracting ultrashort pulses, In *O. Svelto, S. De Silvestri, and G. Denardo (Eds.): Ultrafast Processes in Spectroscopy*, (Plenum Press, New York, 1996), pp. 151-156.

[Saa97a] P. Saari, and H. Sonajalg, “Pulsed Bessel beams,” Laser Physics **7**, 32-39 (1997).

[Saa97b] P. Saari, and K. Reivelt, „Evidence of X-shaped propagation-invariant localized light waves,“ Phys. Rev. Lett. **24**, 4135-4138 (1997).

[Saa05] P. Saari, M. Menert, and H. Valtna, “Photon localization barrier can be overcome,” Opt. Commun. **246**, 445-450 (2005).

[Saa04] P. Saari, and K. Reivelt, “Generation and classification of localized waves by Lorentz transformations in Fourier space,” Phys Rev E Stat Nonlin Soft Matter Phys 69, 036612 (2004).

[Saa06] P. Saari, “How small a packet of photons can be made?,” Laser Physics **16**, 556-561 (2006).

[Saa12] P. Saari, Photon Localization Revisited, In *Sergiy Lyagushin (Ed.): Quantum Optics and Laser Experiments* (InTech - Open Access Publisher, Croatia, 2012), 49-66.

[Sal91] Saleh, B.E.A.; Teich, M.C. Beam Optics, In *Fundamentals of Photonics* (John Wiley and Sons, New York, 1991), pp. 80–107.

[Sch08] A. Schwarz and W. Rudolph, “Dispersion-compensating beam shaper for femtosecond optical vortex beams,” Opt. Lett. **33**, 2970-2972 (2008).

[Sei03] L. Seifert, J. Liesener, and H. J. Tiziani, “The adaptive Shack-Hartmann sensor,” Opt. Commun. **216**, 313-319 (2003).

[Sez85] A. Sezginer, “A general formulation of focused wave modes,” J. Appl. Phys. **57**, 678-683 (1985).

[Sha71] R. V. Shack and B. C. Platt, “Production and Use of a Lenticular Hartmann Screen.” JOSA **61**, 656-660 (1971).

[She89] D.C. O’Shea, Gaussian Beams, in: *Elements of Modern Optical Design* (John Wiley & Sons, New York, 1985), pp. 230–269.

[Shv10] V. G. Shvedov, C. Hnatovsky, W. Krolikowski, and A. V. Rode, "Efficient beam converter for the generation of high-power femtosecond vortices," Opt. Lett. **35**, 2660-2662 (2010).

[Sie96] A.E. Siegman, *Lasers* (Oxford University Press, Mill Valley CA, 1986).

[Sil90] Y. Silberberg, “Collapse of optical pulses,” Optics Letters **15**, 1282-1284 (1990).

[Sim97] N. B. Simpson, K. Dholakia, L. Allen, and M. J. Padgett, “Mechanical equivalence of spin and orbital angular momentum of light: an optical spanner,” Opt. Lett. **22**, 52-54 (1997).

[Siv07] G. A. Siviloglou, J. Broky, A. Dogariu, and D. N. Christodoulides, “Observation of Accelerating Airy Beams,” Phys. Rev. Lett. **99**, 213901 (2007).

[Son97] H. Sõnajalg, M. Rätsep, and P. Saari, “Demonstration of the Bessel-X pulse propagating with strong lateral and longitudinal localization in a dispersive medium,” Opt. Lett. **22**, 310–312 (1997).

[Sor00] E. Sorokin, G. Tempea, and T. Brabec, “Measurement of the root-mean-square width and the root-mean-square chirp in ultrafast optics,” JOSA B **17**, 146-150 (2000).

[Str41] J. A. Stratton, *Electromagnetic theory* (McGraw Hill, New York, 1941), 356.

[Sve89] O. Svelto, *Principles of Lasers*, 3rd Ed. (Plenum Press, New York, 1989).

[Tac10] P. Martelli, M. Tacca, A. Gatto, G. Moneta, and M. Martinelli, “Gouy phase shift in nondiffracting Bessel beams,” Opt. Express **18**, 7108-7120 (2010).

[Tal36] H.F. Talbot, “Facts relating to optical science. No. IV,” Phil. Mag. **9**, 401-407 (1836).

[Tra03] P. Di Trapani, G. Valiulis, A. Piskarskas, O. Jedrkiewicz, J. Trull, C. Conti, and S. Trillo, “Spontaneously generated X-shaped light bullets,” Phys. Rev. Lett. **91**, 093904 (2003).

[Tre02] R. Trebino, *Frequency-Resolved Optical Gating: The Measurement of Ultrashort Laser Pulses* (Springer, 2002).

[Uri10] N. Uribe-Patarroyo, A. Alvarez-Herrero, and T. Belenguer, “A comprehensive approach to deal with instrumental optical aberrations effects in high-accuracy photon’s orbital angular momentum spectrum measurements,” Opt. Express **18**, 21111-21120 (2010).

[Val09] H. Valtna-Lukner, P. Bowlan, M. Lõhmus, P. Piksarv, R. Trebino, and P. Saari, “Direct spatiotemporal measurements of accelerating ultrashort Bessel-type light bullets,” Opt. Express **17**, 14948-14955 (2009).

[Wya92] J.C. Wyant and Katherine Creath, Basic Wavefront Aberration Theory for Optical Metrology, In *Applied Optics and Optical Engineering* Vol. XI, Chapter 1, (Academic Press, Arizona, 1992), chapter 1.

[Yam04] K. Yamane, T. Kito, R. Morita, and M. Yamashita, “Experimental and theoretical demonstration of validity and limitations in fringe-resolved autocorrelation measurements for pulses of few optical cycles,” Opt. Express **12**, 2762-2773 (2004).

[Yam12] K. Yamane, Y. Toda, and R. Morita, "Ultrashort optical-vortex pulse generation in few-cycle regime," Opt. Express **20**, 18986-18993 (2012).

[Zam02] M. Zamboni-Rached, E. Recami, and H. E. Hernández-Figueroa, "New localized Superluminal solutions to the wave equations with finite total energies and arbitrary frequencies," Eur. Phys. J. D **21**, 217-228 (2002).

[Zam06] R. Zambrini and S. M. Barnett, "Quasi-intrinsic angular momentum and the measurement of its spectrum," Phys. Rev. Lett. **96**, 113901(2006).

[Zam08] M. Z. Rached and E. Recami, "Subluminal wave bullets: Exact localized subluminal solutions to the wave equations," Phys. Rev. A **77**, 033824 (2008).

[Zey07] I. Zeylikovich, H. I. Sztul, V. Kartazaev, T. Le, and R. R. Alfano, "Ultrashort Laguerre-Gaussian pulses with angular and group velocity dispersion compensation," Opt. Lett. **32**, 2015-2027 (2007).

[Zha06] L. Zhao, N. Bai, X. Li, L. S. Ong, Z. P. Fang, and A. K. Asundi, "Efficient implementation of a spatial light modulator as a diffractive optical microlens array in a digital Shack–Hartmann wavefront sensor," Appl. Optics **45**, 90-94 (2006).

[Zha12] P. Zhang, Y. Hu, T. Li, D. Cannan, X. Yin, R. Morandotti, Z. Chen, and X. Zhang, "Nonparaxial Mathieu and Weber Accelerating beams," Phys. Rev. Lett. **109**, 193901 (2012).

[Zho10] P. Zhou, X. Wang, Y. Ma, H. Ma, X, Xu, and Z. Liu, "Generation of a hollow beam by active phasing of a laser array using a stochastic parallel gradient descent algorithm", J. Opt. **12**, 015401 (2010).

Acknowledgements

The author of this thesis gratefully acknowledges support and valuable discussions with Prof. T. Elsaesser (MBI Berlin), Dr. Grunwald, Dr. P. Bowlan, PD Dr. G. Steinmeyer, Dr. Griebner, PD Dr. J. Jahns (FernUniversiät in Hagen), Dr. S. K. Das, A. Schmidt, B. Borchers, S. Birkholz, M. Tischer, M. Friedrich, S. Schwanke. I also thanks PD Dr. M. Wörner, Dr. J.-W. Tomm, Dr. T. Hansel, C. Reschke, S. König, A. Treffer, J. Brunne (imtek, Universität Freiburg), C. Fischer, M. Diehl, P. Börner (metrolux optische Messtechnik GmbH), Dr. C. Ropers, S. Huferath (BIAS Bremen), V. Kebbel (bwm Bremen), Dr. M. Becker (Becker & Hickl GmbH, Berlin). For a close and fruitful collaboration and essential technical support, I like to thank especially Dr. S. Osten, S. Krüger from HoloEye Photonics AG and Dr. G. Stibenz and P. Staudt from APE GmbH. I would also like to thank my entire family for their support throughout the years. The thesis was supported in parts by the DFG-project GR1782/13-1.

APPENDIX **A**

Describing diffractive axicon

A diffractive axicon is completely described by its j-th radius r_j and j-th period p_j. In the 2-dimensional cylindrical parameter space the resulting vector $b(r,\eta)$ can be expressed by a radial and an azimuthal component, however, for concentric diffractive axicons $b(r,\eta)$ exhibits only a radial part:

$$r_j = jr \tag{66}$$

$$p_j = r_{j+1} - r_j = (j+1)r - jr = r \tag{67}$$

$$\vec{b}(r,\mu) = \frac{2\pi}{p_j}\vec{e}_r = \frac{2\pi}{r}\begin{pmatrix}\cos(\eta)\\ \sin(\eta)\end{pmatrix} \tag{68}$$

Here, η is the azimuthal angle. In single spiral case the radius becomes a linear function of the azimuthal angle multiplied by a constant integer variable a. The constant a determines the number of turns per unit length.

$$r_j = \pm a\left(j\eta + \eta_0\right) \tag{69}$$

As a direct consequence of this definition, the period $p_j(r, \eta)$ as well as the in-plane vector $b(r,\eta)$ can be regarded to be a composition of an azimuthal and radial contribution.

$$p_j(\eta) = \pm 2\pi r_j \tag{70}$$

$$p_j(r) = r_{j+1} - r_j = a\left[(j+1)2\pi + \eta_0 - j2\pi - \eta_0\right] = a2\pi \tag{71}$$

$$\vec{b}(r,\eta) = \frac{2\pi}{p_j(r,\eta)}\left(\vec{e}_r + \vec{e}_\varphi\right) = \frac{1}{a}\begin{pmatrix}\cos(\eta)\\ \sin(\eta)\end{pmatrix} + \frac{1}{r_j}\begin{pmatrix}-\sin(\eta)\\ \cos(\eta)\end{pmatrix} \tag{72}$$

For higher spiralities the origin of each individual spiral part is shifted by a fixed amount which is considered by the constant angle η_0. Those structures can be implemented in glass substrates by etching processes or programmed into a spatial light modulator which ensures a higher flexibility in generating arbitrary and reconfigurable patterns, however, restricted by the spatial resolution (pixel size).

APPENDIX **B**

Orbital angular momentum in atom physics

Further properties of the optical angular momentum can be found in atom physics where it plays a remarkable role in light-matter interaction like for cooling or trapping of atoms. It was figured out that in the nonrelativistic case both spin and orbital angular momentum can cause a rotationally induced frequency shift and can be seen as the analogue phenomenon to the translational Doppler shift. In first experiments it was shown that by a rotating halfwave plate the optical frequency of circularly polarized light can be shifted by a value of twice the rotational frequency [Gar97]. A similar effect was also predicted for rotating lenses [Nie96]. According to absorbing atoms it was furthermore shown that the resonance frequency shifts by a certain amount proportional to ℓ. It is well-known that the resonance frequency of an atom is shifted if the atom travels with a certain velocity along the beam path. The maximum shift is reached for parallel propagation whereas it is zero for a transverse direction. Corresponding to an existing orbital angular momentum (spin angular momentum was set to be zero) a more detailed analysis of the azimuthal dependence was performed in the quantum mechanical approach for Laguerre-Gaussian beams [All94]. Finally, it was found that the atomic velocity vector can be split into an axial, radial and azimuthal component whereby a significant contribution to the total shift is delivered by the azimuthal Doppler shift:

$$\delta_{\Phi} = \frac{-v_{\Phi} \cdot \ell}{r} = -\Omega_a \ell \tag{73}$$

Here, the shift is directly proportional to topological charge ℓ and inversely proportional to the position r of the atom. To conclude, an orbital angular momentum results in a shift of the frequency like circularly polarized light rotating (observer view) with an angular velocity of Ω_a which induces a frequency shift of $\Omega_a\sigma$. Because spin and orbital angular moment behave additively [Cou98], the rotational frequency shift is then defined as follows:

$$\delta = \Omega_a J \tag{74}$$

$$J = (\ell + \sigma) \quad \text{where } \sigma = 0, \pm 1 \text{ and } \ell = 0,1,2,3\ldots \tag{75}$$

Note that unlike the translational Doppler shift the rotational shift is independent on the unshifted frequency. Its amount does not change. It depends only on the angular velocity.

I

List of publications and conference contributions

Peer reviewed papers

[1] M. Bock, J. Jahns, and R. Grunwald, "Few-cycle high-contrast vortex pulses," Opt. Lett. **37**, 3804-3806 (2012).

[2] M. Bock, S. K. Das, and R. Grunwald, "Ultrashort highly localized wavepackets," Opt. Express **20**, 12563-12578 (2012).

[3] R. Grunwald and M. Bock, "Spatially encoded localized wavepackets for ultrafast optical data transfer," J. Europ. Opt. Soc. Rap. Public. **7**, 12009 (2012).

[4] R. Grunwald, M. Bock, and J. Jahns, "Temporal multiplexing and shaping of few-cycle pulses with microoptical retroreflector arrays," Adv. Opt. Techn. **1**, 97-99 (2012).

[5] M. Bock, S. K. Das, C. Fischer, M. Diehl, P. Börner, and R. Grunwald, "Reconfigurable wavefront sensor for ultrashort pulses," Opt. Lett. **37**, 1154-1156 (2012).

[6] S. K. Das, C. Schwanke, A. Pfuch, W. Seeber, M. Bock, G. Steinmeyer, T. Elsaesser, and R. Grunwald, "Highly efficient THG in TiO_2 nanolayers for third-order pulse characterization," Opt. Express **19**, 16985-16995 (2011).

[7] S. K. Das, M. Biswas, D. Byrne, M. Bock, E. McGlynn, M. Breusing, and R. Grunwald, "Multiphoton-absorption induced UV luminescence of ZnO nanorods irradiated by low-energy fs-pulses," J. Appl. Phys. **108**, 043107 (2010).

[8] M. Bock, S. K. Das, and R. Grunwald, "Programmable ultrashort-pulsed flying

images," Opt. Express 17, 7465-7478 (2009).

[9] S. K. Das, D. Dufft, A. Rosenfeld, J. Bonse, M. Bock, and R. Grunwald, "Femtosecond-laser-induced high spatial frequency quasi-periodic nanostructures on TiO_2 surfaces," J. Appl. Phys. **105**, 084912 (2009).

[10] J. S. Skibina, R. Iliew, J. Bethge, M. Bock, D. Fischer, V. I. Beloglasov, R. Wedell, and G. Steinmeyer, "A chirped photonic-crystal fibre," Nature Photonics **2**, 679 - 683 (2008).

[12] S. K. Das, M. Bock, C. O'Neill, R. Grunwald, K. M. Lee, H. W. Lee, S. Lee, and F. Rotermund, "Efficient second harmonic generation in ZnO nanorod arrays with broadband ultrashort pulses," Appl. Phys. Lett. **93**, 181112 (2008).

[13] M. Bock , S. K. Das, R. Grunwald, S. Osten, P. Staudt, and G. Stibenz, "Spectral and temporal response of liquid-crystal-on-silicon spatial light modulators," Appl. Phys. Lett. **92**, 151105 (2008).

[14] R. Grunwald, M. Bock, V. Kebbel, S. Huferath, U. Neumann, G. Steinmeyer, G. Stibenz, J.-L. Néron, and M. Piché, "Ultrashort-pulsed truncated polychromatic Bessel-Gauss beams," Opt. Expr. **16**, 1077-1089 (2008).

[15] R. Grunwald, S. Huferath, M. Bock, U. Neumann, and S. Langer, "Angular tolerance of Shack-Hartmann wavefront sensors with microaxicons," Opt. Lett. **32**, 1533-1535 (2007).

Books and brochures

[1] M. Bock and R. Grunwald, Spatio-temporal localization of ultrashort-pulsed Bessel beams at extremely low light level, In: H. E. Hernandez-Figueroa, M. Zamboni-Rached, E. Recami (eds.) *Nondiffracting Waves*, (J. Wiley, Berlin, 2013), in press.

[2] M. Bock, S. K. Das, C. Fischer, M. Diehl, P. Börner, and and R. Grunwald, Adaptive shaping of nondiffracting wavepackets for applications in ultrashort pulse diagnostics, in: Non-diffracting waves, In: H. E. Hernandez-Figueroa, M. Zamboni-Rached, E. Recami (eds.) *Nondiffracting Waves*, (J. Wiley, Berlin, 2013), in press.

[3] M. Bock, S. K. Das, R. Grunwald, S. Osten, P. Staudt, and G. Stibenz, "Ultrashort-Pulse Transfer Functions of Spatial Light Modulators, Brochure Optische Technologien," The Congress Laser Optics Berlin 2008, Chapter 4.3, pp. 54-55 (BMBF, Berlin 2009).

[4] J. Jahns, R. Grunwald, M. Bock, “Optical tapped delay filter as beam splitter for fs-pulses,” Jahresbericht FernUniversität Hagen, Optische Nachrichtentechnik, 2007, p. 58.

[5] R. Grunwald, U. Neumann, U. Griebner, G. Steinmeyer, G. Stibenz, M. Bock, V. Kebbel, Self-reconstruction of pulsed optical X-waves, in: M. Zamboni-Rached, E. Recami, H. E. Hernández-Figueroa (Eds.), *Localized Waves, Theory and experiments*, Wiley & Sons, New York, 2008. 299-313, Chapter 11.

Popular scientific journals

[1] R. Grunwald and M. Bock, “Programmable micro-optics for ultrashort pulses,” SPIE Newsroom (2010),

[2] R. Grunwald, M. Bock, “Beamer für ultrakurze Laserpulse,” Kurzmitteilung, Laser Magazin No. 2/2008, pp. 17-18, April 2008.

[3] M. Bock, “Spatio-spectral diagnostics of ultrashort laser pulses by means of statistical moments,” Photonik International, 2-5 (2007).

Invited conference talks / proceedings

[1] S. K. Das, M. Bock, R. Grunwald, B. Borchers, G. Steinmeyer, D. Ristau, T. Vockerodt, and U. Morgner, “First Experimental Evidence for a Non-instantaneous Lifetime of Nonlinear Optical Chi(3) Effects,” Lasers, Sources and Related Photonic Devices, 29 January - 3 February 2012, Rancho Bernardo Inn, San Diego, California, USA.

[2] M. Bock, S. K. Das, and R. Grunwald, “Adaptive shaping of complex pulsed nondiffracting light fields,” SPIE Photonics West, San Francisco, USA, Jan. 22-Jan. 27 (2011), accepted, Proc. SPIE 7950, 795009 (2011).

[3] R. Grunwald, M. Bock, and S. K. Das, “Light bullets, light rings and flying images: adaptive spatial modulation of ultrashort laser pulses, National Laser Symposium (NLS-19), Raja Ramanna Centre for Advanced Technology,” Indore, India, Dec. 1-4 (2010); in: KIRAN, A Bulletin of the Indian Laser Association, Vol. 21, no. 3, 21-23 (Dec. 2010).

[4] R. Grunwald, M. Bock, “Programmable microoptics for ultrashort pulses,” SPIE Photonics Europe, Brussels, April 12-16 (2010); Proc. SPIE 7716, 77160P (2010).

[5] R. Grunwald and M. Bock, “Spatial control and diagnostics of femtosecond pulses with programmable microoptics,” SPIE Photonics West, January 23-28, San Francisco 2010; Proc. SPIE 7579, 75790T (2010).

[6] R. Grunwald and M. Bock, “Adaptive phase encoding and diagnostics of ultrashort pulses with liquid crystal displays,” CLEO Pacific Rim, Shanghai, China, 2009.

[7] J. Jahns, H. Knuppertz, R. Grunwald, and M. Bock, “Microoptical processing and shaping of ultrashort pulses,” International Conference on Transparent Optical Networks (ICTON) 2008, June 22-26, Athens, Greece.

[8] R. Grunwald, M. Bock, S. Huferath-von Luepke, S. K. Das, S. Osten, P. Staudt, and G. Stibenz, “Programmable ultrashort-pulse localized waves,” PIERS Progress in Electromagnetics Research Symposium, Cambridge, USA, July 2-6, 2008, Workshop on Localized Waves, Proceedings on CD-ROM.

[9] R. Grunwald, M. Bock, S. Huferath-von Luepke, “Smart spatio-temporal beam shaping with thin-film microoptics,” SPIE Optics+Photonics Symposium, Laser Beam Shaping IX Conference, San Diego, USA, 2008, (Keynote Lecture); in: Proc. SPIE Vol. 7062, 706202 (2008).

[10] R. Grunwald and M. Bock, “Nondiffracting single photons and quantum interference experiments,” SIAM Conference on Nonlinear Waves and Coherent Structures, July 21-24, 2008, Universitá di Roma ‘La Sapienza’, Minisymp: Localized waves and related phenomena ", Session MS25, Abstracts p. 72.

[11] S. Huferath, R. Grunwald, M. Bock, “Axicon-based Shack-Hartmann sensors for extreme parameters,” Young Scientists International Workshop, in Frame of the Workshop Applied Photonics, Laser Laboratorium Goettingen, April 26, 2007.

[12] R. Grunwald, M. Bock, and G. Wernicke, “Nondiffracting ultrafast images generated with SLM and microaxicon arrays,” 1st Int. Summer School Adaptive Optics and Microoptics, Berlin 2006 (CD-ROM).

[13] R. Grunwald, M. Bock, U. Neumann, G. Stibenz, G. Steinmeyer, “Fringe-free nondiffracting beams for advanced laser diagnostics and processing,” CLEO/QELS 2006, Long Beach, May 21-26, 2006, Technical Digest CD-ROM, paper CMX1.

Conference talks / proceedings

[1] A. Treffer, S. K. Das, M. Bock, J. Brunne, U. Wallrabe, and R. Grunwald, "MEMS axicons for nondiffracting line shaping of ultrashort pulses," Photonics West, San Francisco, USA, February 2-7 (2013), accepted.

[2] S. König, M. Bock, S. K. Das, A. Treffer, and R. Grunwald, "Temporal self-reconstruction of few-cycle nondiffracting wavepackets," Photonics West, San Francisco, USA, February 2-7 (2013), accepted.

[3] J. Brunne, M. Wapler, U. Wallrabe, A. Treffer, M. Bock, R. Grunwald, "Adaptive Fresnel mirror for ultrashort-pulse laser beam shaping," Int. Symposium on Optomechatronic Technologies 2012 (ISOT 2012), Oct. 29-31, 2012, Paris, France.

[4] S. K. Das, A. Rosenfeld, H. Messaoudi, M. Bock, M. Tischer, and R. Grunwald, "Quantitative estimation of intensity dependent wavelength periods of laser-induced ripples," 13th International Symposium on Laser Precision Microfabrication LPM 2012, Washington, USA, June 12-15 (2012).

[5] M. Bock, J. Jahns, and R. Grunwald, "8-fs high contrast vortex pulses," CLEO/QELS, May 6-11 (2012) San Jose, CA, USA (**Post Deadline Paper** CTh5C.5).

[6] M. Bock, S. K. Das, and R. Grunwald, "Few-cycle highly localized wavepackets on demand with superior temporal transfer," CLEO/QELS, May 6-11 (2012) San Jose, CA, USA (paper QM4E.2).

[7] M. Bock, J. Skibina, D. Fischer, R. Grunwald, S. Burger, V. Beloglazov, and G. Steinmeyer, "10-fs pulse delivery through a fiber," CLEO/QELS, May 6-11 (2012) San Jose, CA, USA (paper CTh3G.3).

[8] M. Bock, P. Börner, M. Diehl, C. Fischer, S. K. Das, and R. Grunwald, "Adaptive characterization of few-cycle wavepackets with high-pulse-fidelity time-wavefront sensors," CLEO/QELS, May 6-11 (2012) San Jose, CA, USA (paper CTh1N.2).

[9] S. K. Das, M. Bock, R. Grunwald, B. Borchers, J. Hytti, G. Steinmeyyer, D. Ristau, T. Vockerodt, and U. Morgner, "Non-instantaneity of $\chi^{(3)}$ nonlinear optical effects," CLEO/QELS, May 6-11 (2012) San Jose, CA, USA (paper CM1J.4).

[10] A. Treffer, J. Brunne, S. K. Das, M. Bock, H. Messaoudi, U. Wallrabe, and R. Grunwald, "Characterization of fast-switching low-dispersion MEMS-based micro-axicons for applications in ultrashort-pulse nanostructuring," Deutsche Physikalische Gesellschaft, Frühjahrstagung Sektion AMOP, Stuttgart, Germany, March 12-16, 2012.

[11] S. K. Das, F. Guell, H. Messaoudi, M. Bock, and R. Grunwald, “Evidence for non-mass-transfer mechanism in fs-laser formation of sub-200 nm structures on sapphire,” CLEO/QELS, May 6-11 (2012) San Jose, CA, USA (paper CM4K.4).

[12] S. K. Das, R. Grunwald, A. Rosenfeld, M. Bock, and G. Steinmeyer, “Nanostructured material for photonic applications,” Int. Conf. on Theoretical and Appl. Phys. (ICTAP), 1-2 Dec., 2011, IIT Kharagpur, India.

[13] R. Grunwald and M. Bock, “Ultrafast transfer of spatially encoded data with programmable arrays of highly localized wavepackets,” 1st EOS Topical Meeting on Micro- and Nano-Optoelectronic Systems, December 7-9, 2011, Bremen.

[14] J. Brunne, U. Wallrabe, A. Treffer, M. Bock, and R. Grunwald, “Fast optical line shaper for ultrashort-pulse laser nanomachining,” 2011 International Conference on Optical MEMS & Nanophotonics (OMN2011), August 8-11, 2011, Istanbul, Turkey, Conference Digest p. 5-6.

[15] M. Bock and R. Grunwald, “Ultrashort-pulsed, ultra-broadband nondiffracting tubular beam generated with a phase only spatial light modulator,” DPG Spring Meeting, Hannover, Germany, March 2010, session Q 34.3, paper F 342.

[16] S. K. Das, M. Bock, A. Rosenfeld, and R. Grunwald, “Laser-induced periodic nanostructures on ZnO surfaces with a patterned beam in water environment,” CLEO/QELS 2010, paper CMR3.

[17] S. Huferath-von Luepke, V. Kebbel, M. Bock, and R. Grunwald, “Simulation of pulsed Bessel-like beams,” Laser Optics Berlin, 2010.

[18] M. Bock, S. K. Das, A. Richter, J. T. Preusse, and R. Grunwald, “Programmable supercollimated ultrashort pulses,” Laser Optics Berlin, 2010.

[19] A. Richter, M. Bock, J. Jahns, and R. Grunwald, “Orbital angular momentum experiments with broadband few cycle pulses,” SPIE Photonics West, January 23-28, San Francisco 2010, Proc. SPIE 7613, 761308 (2010).

[20] M. Bock, S. K. Das, R. Grunwald, “Spatio-spectral encoding of nondiffracting ultrashort pulses,” Workshop Optics in Computing (Optik in der Rechentechnik, ORT), collocated to ECOC (European Conference on Optical Communication), Sept. 24, 2009, Vienna, Austria.

[21] S. Huferath-von Luepke, M. Bock, and R. Grunwald, “Adaptive Bessel-autocorrelation of ultrashort pulses with phase-only spatial light modulators,” SPIE Europe - Optical Metrology, June 14-18, Munich 2009.

[22] S. K. Das, M. Bock, E. McGlynn, M. Biswas, and R. Grunwald, "Strong multiphoton-absorption-induced UV luminescence from ZnO nanorod arrays grown by vapour-liquid-solid mechanism," CLEO Europe - EQEC, Munich 2009.

[23] J. Jahns, H. Knuppertz, R. Grunwald, M. Bock, "Microoptical CDM-technique for satellite communications," Joint Meeting of DGAO-SIOF, June 2-5, 2009, Brescia, Italy.

[24] M. Bock, S. K. Das, and R. Grunwald, "Ultrashort-pulsed nondiffracting images," CLEO/IQEC 2009, Baltimore, May 31 – June 5, 2009, paper CME4

[25] S. K. Das, D. Dufft, M. Bock, A. Rosenfeld, J. Bonse, and R. Grunwald, "Femtosecond-laser induced sub-200 nm strcutures in TiO2," CLEO/IQEC 2009, Baltimore, May 31 – June 5, 2009, paper JWA1

[26] S. K. Das, M. Bock, C. O'Neill, R. Grunwald, K. M. Lee, H. W. Lee, S. Lee, and F. Rotermund, "Highly-efficient second harmonic generation in ZnO nanorods with ultrashort pulses," CLEO/IQEC 2009, Baltimore, May 31 – June 5, 2009, paper IML6

[27] M. Bock and R. Grunwald, "Spatial light modulation and projection of few-femtosecond laser pulses with liquid-crystal-on-silicon microdisplays," Summer School, International Photonics Cluster, Berlin 2008.

[28] S. Huferath-von Luepke, V. Kebbel, M. Bock, and R. Grunwald, "Noncollinear autocorrelation with radially symmetric nondiffracting beams," SPIE Optics+Photonics Symposium, Advanced Metrology Conference, San Diego, USA, in: Proc. SPIE Vol. 7063, 706311-1-12 (2008).

[29] M. Bock, S. K. Das, R. Grunwald, S. Osten, P. Staudt, G. Stibenz, "High fidelity ultrashort-pulse transfer with spatial light modulators," LOB Berlin 2008.

[30] R. Grunwald, M. Bock, and J. Jahns, "Femtosecond laser pulse shaping with microoptical retroreflector arrays," CLEO 2008, San José, CA; Technical Digest CD-ROM, paper Technical Digest CD-ROM, paper CTuU3.

[31] R. Grunwald, S. Huferath, M. Bock, "Robust Shack-Hartmann wavefront sensing with ultraflat microaxicons," SPIE Europe Optical Metrology, Munich, June 18-21, 2007, Proc. SPIE 6617-13 (2007).

[32] R. Grunwald, U. Neumann, M. Bock, and G. Steinmeyer, "Young's interference experiment with ultrashort-pulsed Bessel beams," CLEO/QELS 2007, Baltimore, May 6-11, 2007, Technical Digest CD-ROM, paper CThM7.

[33] R. Grunwald and M. Bock, “Spatio-Spectral Analysis and Encoding of Ultrashort Pulses with Higher-Order Statistical Moments,” CLEO/QELS 2007, Baltimore, May 6-11, 2007, Technical Digest CD-ROM, paper CWJ2.

[34] R. Grunwald, M. Bock, G. Steinmeyer, G. Stibenz, “Graxicons for hyperspectral diagnostics of few-cycle laser pulses,” CLEO/QELS 2006, Long Beach, May 21-26, 2006, Technical Digest CD-ROM, paper CWJ2.

[35] R. Grunwald, U. Neumann, M. Bock, K. Mann, B. Schäfer, V. Kebbel, “Wavefront sensing at extreme parameters, Laser Optik Berlin (LOB),” In: Optical Technologies in Germany 2006, Technical Digest, 62-63.

Conference posters / proceedings

[1] H. Messaoudi, S. K. Das, M. Bock, E. McGlynn, D. Byrne, F. Güell, and R. Grunwald, “Ultrashort pulse characterization utilizing highly nonlinear ZnO nanostructures,” 5th Szeged International Workshop on Advances in Nanoscience 2012 (SIWAN5), Szeged, Hungary, 24-27 October, 2012, accepted.

[2] S. K. Das, C. Schwanke, M. Bock, A. Pfuch, W. Seeber, and R. Grunwald, “Enhanced third order nonlinearity in nanocrystalline TiO2 thin films,” 2nd Int. Workshop Nonlinear Nanostructures for Ultrafast Laser Application, 2011, May 19-20, Berlin, Germany, Technical Digest, Poster 3.

[3] S. K. Das, C. Schwanke, A. Pfuch, W. Seeber, M. Bock, and R. Grunwald, “Enhanced surface third harmonic generation in TiO2 nanolayers,” CLEO:2011, Baltimore, USA, PosterK-JThB52.

[4] M. Bock, C. Schwanke, S. K. Das, R. Beuthner, M. Diehl, C. Fischer, and R. Grunwald, “Adaptive wavefront diagnostics of ultrashort pulses with programmable microaxicons,” CLEO Europe - EQEC, Munich 2011, Poster CF.P.13.

[5] J. Brunne, M. Bock, A. Treffer, U. Wallrabe, and R. Grunwald, “Adaptive generation of Bessel-like beams by reflective multi-electrode piezo-axicons,” CLEO Europe - EQEC, Munich 2011, Poster CF.P.14.

[6] S. K. Das, A. Rosenfeld, M. Bock, A. Pfuch, W. Seeber, and R. Grunwald, “Scattering-controlled femtosecond-laser induced nanostructuring of TiO2 thin films,” SPIE Photonics West, San Francisco, USA, Jan. 22-27 (2011), Proc. SPIE 7925, 79251B (2011).

[7] M. Bock, J. T. Preusse, and R. Grunwald, “Spatio-temporal analysis of ultrashort pulses by statistical signatures of frequency converted needle beams,” CLEO/QELS 2010, poster JThE93.

[8] S. K. Das, D. Byrne, E. McGlynn, M. Bock, and R. Grunwald, “Multi-photon excited UV luminescence of ZnO nanorods after irradiation with few-nJ femtosecond laser pulses,” CLEO/QELS 2010, poster JThE16.

[9] S. K. Das, M. Bock, E. McGlynn, M. Biswas, and R. Grunwald, “Strong multiphoton-absorption-induced UV luminescence from ZnO nanorod arrays grown by vapour-liquid-solid mechanism,” CLEO Europe - EQEC, Munich 2009, poster CF.P2.

[10] M. Bock and R. Grunwald, “Flexible spatial-domain beam shaping of few-cycle pulses with reflective phase-only liquid crystal displays,” CLEO Europe - EQEC, Munich, 14-19 June, 2009, presentation number CF.P.2

[11] S. Huferath-von-Luepke, M. Bock, R. Grunwald, and V. Kebbel, “Comparison of autocorrelator, Bessel autocorrelator and modified Bessel autocorrelator for ultra-short pulse diagnostics,” Fringe '09 - 6th Int. Workshop on Advanced Optical Metrology, Sept. 14-16, 2009, Stuttgart.

[12] H. Knuppertz, M. Bohling, J. Jahns, M. Bock, and R. Grunwald, “Ultraprecisely machined microoptics for fs-pulse shaping and replication,” Ultrafast Phenomena 2008, June 9-13, Stresa (Lago Maggiore), Italy, THUIIIa.4.

[13] R. Grunwald and M. Bock, “Bessel-type interference patterns detected in single photon regime,” CLEO Europe IQEC, Munich, June 17-22, 2007, Technical Digest CD-ROM, paper IF-13-TUE.

[14] M. Ferstl, G. Devendra, R. Grunwald, M. Bock, “Lithographically fabricated micro-optical array beam shapers for ultra-short pulse lasers,” CLEO/QELS 2006, Long Beach, May 21-26, 2006, Technical Digest CD-ROM, paper JThC98.

Patents

[1] R. Grunwald and M. Bock, „Verfahren und Vorrichtung zur räumlich-zeitlichen Pulsanalyse mittels statistischer Parameter“ (filed July 7, 2010, DE 10 2010 026 701.5 patented October 20, 2011).

[2] R. Grunwald and M. Bock, „Verfahren und Anordnung zur spektralaufgelösten Charakterisierung einer Wellenfront ultrakurzer Laserimpulse“ (filed December 12, 2005, DE 102005059755B3 patented June 14, 2007).

Selbständigkeitserklärung

hiermit erkläre ich, dass ich die von mir eingereichte Arbeit selbstständig und unter Benutzung der von mir angegebenen Literatur sowie der Hinweise meiner Betreuer Herrn Prof. Dr. T. Elsässer und Dr. R. Grunwald vom Max-Born-Institut für Nichtlineare Optik angefertigt habe.

Berlin, 10. September 2013 _____

Deklaration

Hiermit bestätigte ich, dass der Inhalt dieser Arbeit im Ganzen oder Teile davon nicht bei anderen Instituten oder Universitäten für den Verleih eines Abschlusses eingereicht wurde, und dass vorher noch kein entsprechender Doktorgrad erworben wurde.
Weiterhin nehme ich die dem angestrebten Verfahren zugrunde liegenden Promotionsordnung zur Kenntnis.

Berlin, 10. September 2013 _____